SEMI-ANNUAL PROGRESS REPORT *

JUNE-NOVEMBER, 1974

NASA GRANT NGR-15-005-147 "GAS FILM COOLING OF TURBINE VANES"

Submitted by

Gary J. Hanus

Purdue University

West Lafayette, Indiana 47906

Principal Investigator:

Mel R. L'Ecuyer

* The NASA Technical Officer for this grant is
David Poferl
NASA Lewis Research Center
21000 Brookpark Road
Cleveland, Ohio 44135

NOV 1974
RECEIVED
NASA STI FACILITY
INPUT BRANCH

SUMMARY

Heat transfer measurements were made on the suction and pressure surfaces of a turbine vane representative of an advanced, high-temperature, high-pressure turbine. Due to facility constraints on available gas temperature, pressure, and flow rates and to instrumentation considerations the testing was performed at reduced gas conditions. By proper matching of the significant similarity parameters, the heat transfer measured on the 3x size vane was representative of that experienced in the more severe environment of actual engine conditions. The objectives of this series of tests were to evaluate the performance of the measuring techniques and to compare the results with exisitng boundary layer predictions. These initial measurements were a preliminary step in conducting a film cooling study of injection from a row of radially angled holes in the leading edge region of a turbine vane. The dry wall (non film-cooled) data for the vane surfaces showed the actual heat transfer to be lower than predicted. On the suction surface, the Stanton number distribution was approximately 25% lower than predicted. The pressure surface showed a distinct region just prior to the fully developed turbulent region in which the Stanton number was 50% lower than predicted, but then returned to within $\pm$ 10% of the predicted value.

INTRODUCTION

The basic objective of this testing program was to provide realistic heat transfer data under film cooling conditions for a simulated 3x size turbine vane operating at reduced flow conditions. In addition to recording heat flux levels at design and off-design conditions, the following secondary items were investigated to insure the reliability and quality of the testing methods and results:

1. Influence of vertical and horizontal pitot-static, total temperature probes on the average heat flux measurements taken while the probes were cycled upstream of the test surfaces.

2. Comparison of sampled heat flux output (digitally) by 360 computer with visual display of analog output on oscillograph (comparison of mean heat flux levels).

3. Determination of ability to reproduce flow conditions and heat flux levels from run to run.

ANALYSIS

In order to conduct a meaningful investigation of heat transfer phenomena occuring in high temperature turbine environments, it is necessary to consider matching as many similarity variables characteristic of the dimensionless conservation equations as possible. It follows from nondimensionalizing such governing equations that the heat transfer to a surface in the form of the Stanton number can be expressed as:

$$St_x = St_x\ (x/L,\ Re_x,\ Pr,\ Gr_x,\ E)$$

Analyzing the particular problem of simulaing a turbine vane allows one of these parameters to drop out, namely the Grash of No. By proper geometric modeling and flow manipulation, it is possible to maintain similarity between the hydrodynamic and thermal boundary layers of a scaled-up model under reduced flow conditions and the actual turbine vane under engine operation. Appendix A provides a detailed outline of the considerations necessary to accurately model high-temperature, high-pressure heat transfer.

TEST FACILITY

Figures 1 and 2 show the details of the main flow channel used in this investigation. Supply air is split into two legs: a by-pass channel and a combustor air channel. These two legs feed a 10" OD pipe with mixed heated air. The main hot gas supply flows first through a turbulence production region consisting of interchangeable ducts and wire mesh screens. Proper selection and placement of the screens can achieve from 6% to 11% freestream turbulence intensity just prior to the main test section. The entrance to the test section is 9.6" x 4.5" and divided into three legs at the exit with flow areas in the proportions of 2:1:1. The largest leg supplies the air for the main flow channel which is bordered by the suction and pressure surface walls of two 3x size advanced concept, core-engine vane contours. The remaining two legs provide bleed capability for establishing the desired Mach number distribution over the vane surfaces.

The turbine vane surfaces are constructed of contoured stainless steel inner bodies over which are attached 0.0625" OFHC copper skins. As shown in Figures 3 and 4, the vanes are water cooled across the span at various locations along the vane surfaces. The coolant channels are 0.0625" deep and 0.5" wide and carry from one to two gal/min. each. The coolant channels can be individually throttled to provide the maximum range possible of heat removal along the vane contours. Such a capability will insure maintenance of a nearly uniform wall-temperature boundary condition.

INSTRUMENTATION

Both the suction and pressure surfaces of the test vane are instrumented with copper-constantan thermocouples, static wall pressure taps and thin foil heat flux transducers. The thermocouples and pressure taps are all located in the support lands separating the water coolant channels as shown in Figures 3 and 4. The heat flux transducers are threaded into copper plugs fixed at various locations along the surface. Generally, they are placed fully within a coolant channel to provide as good a heat sink as possible for the heat flux gages. Due to the important part played by the heat flux transducers, a separate section will be devoted to its characteristics, operation, calibration, and limitations.

Each copper-constantan thermocouple was made by heli-arcing the copper and constantan within a stainless steel sheath 0.030" to 0.050" in diameter. The static wall taps were 0.020" ID copper tubes brazed flush to the surface and joined beneath with 0.040" OD stainless tubing. Both wall pressure taps and thermocouples were oven brazed to the test surfaces at 1500° - 1600° F. Table 1 identifies each item of instrumentation and its corresponding location with reference to the stagnation line of the vane.

HEAT FLUX TRANSDUCERS

The basic principal behind the Gardon or thin foil heat flux gage is illustrated in figure 5. A thin circular constantan foil is fused around the circumference of one end of a tube-like, copper heat sink. Thus, a continuous thermocouple junction is formed along the outer edge of the foil. On the underside of the foil, a fine copper wire is joined at the center, forming a second copper-constantan junction. All the incident heat flux travels radially along the foil (due to the dead space behind the thin foil) and establishes a parabolic temperature profile which has a ΔT from center to edge that is dependent on the magnitude of the incident heat flux.

Accounting for the physical properties variations of the constantan foil AND THE CHANGE IN JUNCTION EMF READ BETWEEN THE TWO FOIL contacts, the differential emf read between the two foil ~~contacts~~ JUNCTIONS becomes linearly dependent upon the magnitude of the incoming heat flux.

The particular design of the thin foil gage used in this study can be characterized as miniature. In order to avoid test surface irregularities with gage installation and at the same time approach point source measurements it was necessary to have a sensor of small diameter compared to the characteristic dimensions of the test surface. In addition, the small nature of the gage dictates small Δemf, insuring that the ΔT from center to edge of foil is not too great. This is an important consideration since large step inputs in the temperature boundary condition can induce boundary layer instability at the time when such disturbances cannot be tolerated (i.e., laminar boundary layer development).

Figure 6 is a detailed drawing of the heat flux sensors and the installation technique used in this program. The basic sensor device, as shown in Figure 5, is pressed into a 0.145" threaded (5-40 UNC) OFHC copper plug. The sensor area itself is 0.020" in diameter and 0.005" thick. A 0.002" diameter copper wire is laser-welded to the center of the sensing foil from beneath. This wire, together with a 0.005" diameter copper ground wire (attached to heat sink) are both coated with 0.002" of teflon, fully shielded, and brought out the bottom of the threaded plug. The heat flux gage is then threaded into the OFHC copper plug mounted within the test surface wall. The threaded portion of the gage is long enough to provide 10-11 threads of contact with the water-cooled plug.

Miniature gages have the advantages mentioned previously but also have the disadvantage of small output voltages. With a maximum ΔT between the center and edge of the sensing foil of $5^{o}F$, the maximum output level is only in the microvolt range. Therefore, each heat flux transducer has associated with it an individually matched operational amplifier with a gain near 1000, thus converting the raw transducer microvolt signal to a more convenient millivolt level. With the amplifiers, the gages are calibrated with a sensitivity of 10 mv/Btu-ft^2-sec. Due to the microvolt level of the raw output, all solder connections were made with low noise cadmium-tin solder to eliminate any additional emf sources between the sensors and the amplifiers. Since the amplifiers' output varies 3 millivolts/$10^{o}F$ change in ambient temperature, (a zero shift and not a calibration change) all amplifiers and associated electrical

connections were thermally isolated from ambient conditions using a sealed, styrofoam enclosure. Figure 7 shows the heat flux signal processing procedure.

Calibration of the sensors followed the technique depicted in Figure 8. Each sensor to be calibrated was mounted on the center axis at the entrance of one of two, back-to-back (symmetrical) black-body cavities. The black body was a graphite assembly tapered to acheive uniform inside wall temperatures with resistance heating. The heat flux source-temperature was monitored on the opposite side of the apparatus in a similar black body cavity using an optical pyrometer. The length to diameter ratio of the cavity was large enough, coupled with the high emissivity of the walls, to simulate extremely well an emissivity of unity near where the sensor was placed. A view factor between the black body opening and the sensor surface can be easily calculated and, knowing the radiative properties of the coated sensor, an accurate calibration can be made.

The sensor's operation is based on a few assumptions that must be recognized. In order for the calibration to be valid, the sensor body temperature must be greater than 50°F and less than 450°F. Outside this range, the change in emf of the thermocouple junctions is not compensated for by the physical property changes of the foil to produce the typical linear calibration curve. Secondly, the gages must operate in a field of heat flux uniform over an area that is much greater than the sensor area. Neither of these restrictions posed any difficulty in conducting this study. Each sensor is accurate to within ± 3% of full scale.

Repeatability is within ½%, with any greater amount attributed to inaccuracies of reproducing flow conditions. The response time for a typical sensor is 2.4 milliseconds.

RESULTS

As listed in Table 2, twenty-two flow conditions were used in the heat transfer study. The underlined reading numbers designate the reduced flow conditions necessary for simulation of a high-pressure, high-temperature turbine vane. Although the total pressure used was 16% higher than that representative of engine conditions, the Stanton number for such a change will differ only by about 3% assuming the heat transfer coefficient varies as the pressure to the 0.8 power and that the Mach number distribution remains unchanged. Therefore, the dimensionless heat transfer results can be regarded as accurate simulations of real engine conditions.

In recording the heat flux data two different methods were employed: (1) data was sampled 16 times per data point corresponding to the number of positions reached by each of two pitot-static probes in mapping out flow profiles in a plane upstream of the test surfaces, and (2) analog data of the heat flux was displayed on a high response oscillograph recorder. The question arose as to the accuracy of an averaged output based on 16 sample points of a signal with a peak-to-peak noise level as much as 8% of the mean signal level. Figures 9-12 show a comparison of the mean heat flux level based on an average of 16 readings digitally sampled by an IBM 360 system and the mean level as recorded by drawing a mean value line through the analog oscillographic output. The majority of the data points show excellent agreement between the two methods. A few are within a $\pm$ 10% band. The ability

to accurately determine a true mean from the analog output depends on the following: (1) resolution, (2) accuracy of zero setting, (3) calibration curve and (4) the ability to determine just where to place the mean value in view of the noise band. It was decided that since the above four considerations can lead to errors of the order of 10%, the computer sampled-and-averaged data would be the simpler and more accurate method. The computer sampling method does not have the problems of resolution and zero settings.

Figures 9-12 also show another important item. The open symbols represent averaged data based on the computer sampling the heat flux while the pitot-static probes were within the flow stream. The corresponding analog output is without the presence of the probes. In general, the leading and trailing edge regions of the pressure surface were shown to be sensitive to the presence of the probes, especially the vertical probe. The closed symbols represent averaged heat fluxes with all probes retracted from the flow channel. This narrowed the band of difference between the two averaging methods. From this information the following procedure was adopted for recording a data point:

1. Output would be recorded and processed (averaged) digitally by the computer with an analog back-up system in parallel.

2. A data point of 16 samples corresponding to 16 positions of the pitot-static probes would determine all flow parameter values such as local velocity distribution, wall temperature, weight flow, inlet temperature, and velocity profiles. . . heat flux output for this would be ignored.

3. An additional data point of 16 samples would be taken with probes fully retracted under exactly the same conditions as (2) of which the recorded heat flux data would be the primary information.

Of all the test points taken, the majority were set as closely to the simulated design operating conditions as possible. Only those points are analyzed in detail within this section of the report. Over a period of three weeks during testing, the design flow conditions was ~~attempted to be~~ reproduced five times corresponding to reading numbers 69, 79, 85, 87, and 93.

Figures 13-17 show a comparison between the predicted design Mach number distribution over the vane and the measured values. Agreement is well within 10% of design except for a region on the pressure surface experiencing an unfavorable pressure gradient. Here the deviation is about 20%. Figures 18-27 are the corresponding velocity distributions for the design conditions.

Figures 28-32 display the heat transfer coefficient distribution along the suction surface as compared to the predicted values using the same measured velocity distribution, total pressure, and total temperature. Figure 33 shows all five readings with the mean values plotted along with an indication of the flow condition reproducibility. Based on the mean values, the heat transfer coefficient is $\pm 20\%$ of the predicted values. The largest variation in reproducibility was in the region near transition. This is reasonable due to the sensitivity of this region to minute variations in external flow conditions.

The pressure surface heat transfer ocefficient distribution as seen in Figures 34-38 exhibits the same sensitivity to changes in flow conditions near the transition region. The mean values of the five reading numbers were ±10% of the predicted values with the same "±10% about the mean" repeatability band as with the suction surface. Three-dimensional effects at the pressure surface trailing edge (due to a step-type trailing edge simulation) seem to be evident in the higher than predicted heat fluxes.

The real proof of the simulation procedure is in the behavior of the non-dimensional heat transfer parameter, the Stanton number. Figures 40-44 and 46-50 are the Stanton number variations for the suction and pressure surfaces, respectively, for the five readings taken near the design flow conditions. The trend along the suction surface follows the predicted trend quite closely. The values however, are shown to be about 20% lower than predicted (see Figure 45). On the pressure surface, the data falls within a ± 10% band of the predicted value (see Figure 51) except for a region following transition in which the heat conductance decay along the surface is much more severe than predicted, followed by a rapid recovery back to a level and decay rate as expected for such flow conditions. This region's behavior is still under investigation and will be analyzed in more detail following future dry wall testing.

The water coolant channels below the skins of the test vanes were valved in such a way as to minimize conduction effects along the wall and provide a uniform wall boundary condition. Figures 52-56 show both the lateral (along the span) and axial (along surface contour) temperature distributions. The most significant temperature gradient occurred at the trailing edges where the copper surfaces join the stainless steel support structure. In general, this maximum temperature deviates at most 10% from the mean surface temperature. Such a gradient is analyzed in Appendix B, providing an estimate of the amount of heat carried by wall conduction as compared to the total heat input to the high gradient region supplied by convection. The temperature distributions indicate a uniform boundary condition with at least 78% of all measured wall temperatures within 2.4% of the calculated mean value.

In addition to the data taken at the design condition, measurements were made over a range of total pressures from 35.2 psia to 71.6 psia, corresponding to a variation of the inlet Reynolds number of 56,774 to 103,540 based on the leading edge radius. The Mach number level and distribution remained unchanged during this total pressure variation. Figures 57 and 58 display the increase in the heat transfer coefficient for the suction surface with increasing total pressure level. As seen in Figure 59, the increase in the heat transfer coefficient depends upon the pressure to the 0.8 power fairly well for the lower pressure levels. However, as Figures 57 and 58 show, there is a marked deviation from the expected trends at the upper pressure levels. Perhaps a separation phenomenon is occuring at these higher Reynolds numbers. The pressure surface behaved more predictably at all pressure levels as shown in

Figures 60 and 61. Calculating approximate expected heat transfer increases based on flat plate, zero pressure gradient relations shows the pressure surface to follow the 0.8 power relation within $\pm 5\%$ up to 70 psia, in which case the inlet Reynolds number is well over 100,000. It appears, based on the heat flux variation with increasing Reynolds number, that the heat flux measuring technique is providing reliable data and responds correctly to changes in overall flow conditions.

CONCLUSIONS

The following items may be listed as the most significant findings of this test series:

1. The use of Gardon-type, thin foil heat flux transducers has proved to be a convenient, reliable and rugged device for measuring incident heat fluxes within severe thermal environments.

2. The present facility is capable of matching the significant similarity variables such as Mach number, weight flow, dimensionless temperature ratio, and free-stream turbulence intensity that should insure reliable Stanton number variations along the test surface. Measured Stanton numbers follow the predicted trends within 20% on the suction surface and within $\pm$ 10% on the pressure surface (excluding the transition region and a small region thereafter).

3. Care must be exercised in the manner in which the data is taken to eliminate such extraneous effects as probe interference and sensor contamination.

4. Flow condition reproduction is at worst within $\pm$ 10% of a mean value of all readings.

BIBLIOGRAPHY

1. "Thermodynamic and Transport Properties of Air and the Combustion Products of Natural Gas and of ASTM-A-1 Fuel with Air", David J. Poferl, et al; NASA TN D-5452, October, 1969.

2. "Heat Transfer to the Transpired Turbulent Boundary Layer", William M. Kays; ASME paper 71-HT-44

3. "Similarity Constraints in Testing of Cooled Engine Parts", Colladay, R.S. and Stepka, F.S.; NASA TN D-7707, June, 1974.

PRESSURE SURFACE

	PRESSURE TAPS	THERMOCOUPLES	HEAT FLUX GAGES
1	-0.35	-0.35	0.69
2	-0.35	-0.35	1.23
3	0.37	0.37	2.03
4	0.37	0.965	2.59
5	0.965	0.965	3.09
6	0.965	2.31	3.63
7	0.965	2.31	4.725
8	1.755	2.31	
9	2.83	3.38	
10	2.83	4.45	
11	2.83	5.57	
12	3.91		
13	5.01		
14	5.01		
15	5.01		

SUCTION SURFACE

	PRESSURE TAPS	THERMOCOUPLES	HEAT FLUX GAGES
1	0.32	0.32	1.15
2	0.32	0.32	1.69
3	0.95	0.95	2.58
4	0.95	1.51	3.13
5	1.51	1.51	3.72
6	1.51	2.87	4.27
7	1.51	2.87	5.37
8	2.26	2.87	6.47
9	3.45	3.99	
10	3.45	5.11	
11	3.45	6.21	
12	4.56	7.29	
13	5.64		
14	6.73		
15	6.73		
16	6.73		
17	-0.24		

INSTRUMENTATION LOCATIONS
(all dimensions in inches with
reference to stagnation line)

TABLE 1.

TABLE 2.

Rdg.No.	P_{total}	P_{static}	T_{total}	M_{inlet}	RE_{inlet}	Tu %	$T_{w,ave.}$ °R	M_{exit}
53	58.8	57.4	1226	0.187	92,164	6.0	560	0.76
54	45.5	44.4	1242	0.190	71,374	6.0	560	0.76
56	35.3	34.5	1220	0.191	56,774	6.0	555	0.76
57	71.2	69.5	1241	0.190	111,460	6.0	560	0.76
58	60.6	59.1	1244	0.190	93,550	6.0	560	0.76
59	60.9	59.6	1251	0.178	88,723	---	560	0.75
60	47.3	46.3	1228	0.180	71,394	---	560	0.76
61	37.3	36.5	1235	0.180	55,969	---	560	0.76
62	71.6	70.1	1251	0.176	103,540	---	565	0.76
63	60.4	59.1	1246	0.178	88,706	---	560	0.76
69	51.9	50.4	1233	0.213	91,613	---	565	0.77
73	45.8	44.4	1263	0.213	78,783	---	565	0.78
75	59.1	57.4	1235	0.208	101,840	---	570	0.75
77	50.9	49.4	1244	0.211	87,889	---	570	0.76
79	51.9	50.4	1238	0.212	90,596	---	570	0.77
81	45.6	44.2	1234	0.213	80,457	---	565	0.78
83	58.7	57.0	1241	0.209	100,930	---	570	0.75
85	51.9	50.3	1242	0.211	89,705	---	570	0.76
87	51.7	50.2	1255	0.209	87,607	11.0	560	0.77
89	45.2	43.9	1238	0.211	78,724	11.0	565	0.76
91	59.7	58.0	1246	0.206	100,840	11.0	575	0.75
93	51.7	50.2	1245	0.207	87,726	11.0	570	0.76

Underline designates design conditions

* Unless otherwise noted the following symbols apply to the following reading numbers

⬡ Rdg.69 ⊙ Rdg.79 ⊡ Rdg.85 ◇ Rdg.87 ◭ Rdg.93 ✕ Rdg.62

FLOW CONDITIONS
TABLE 2.

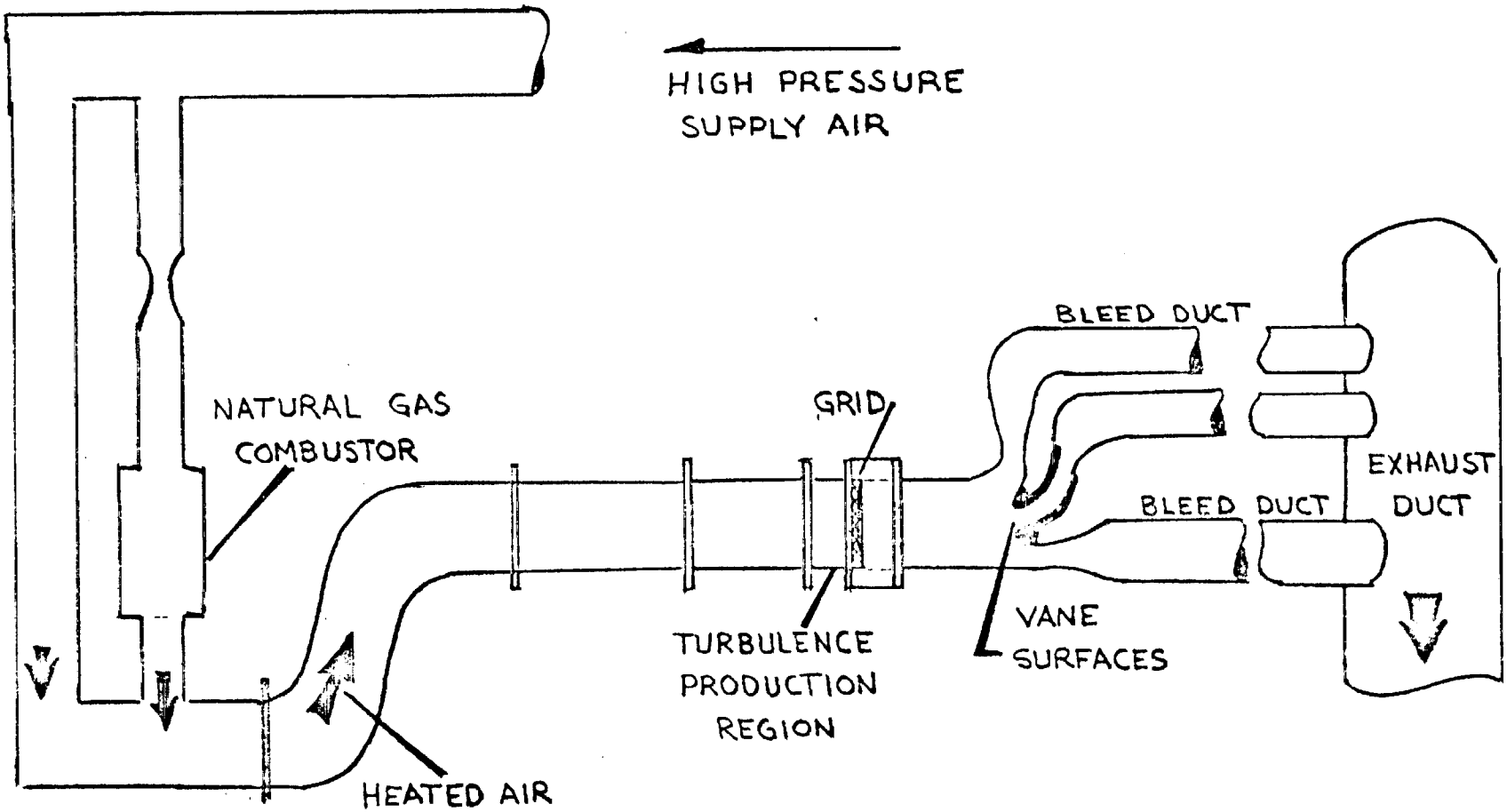

TEST FACILITY SCHEMATIC

FIGURE 1.

TEST SECTION
FIGURE 2.

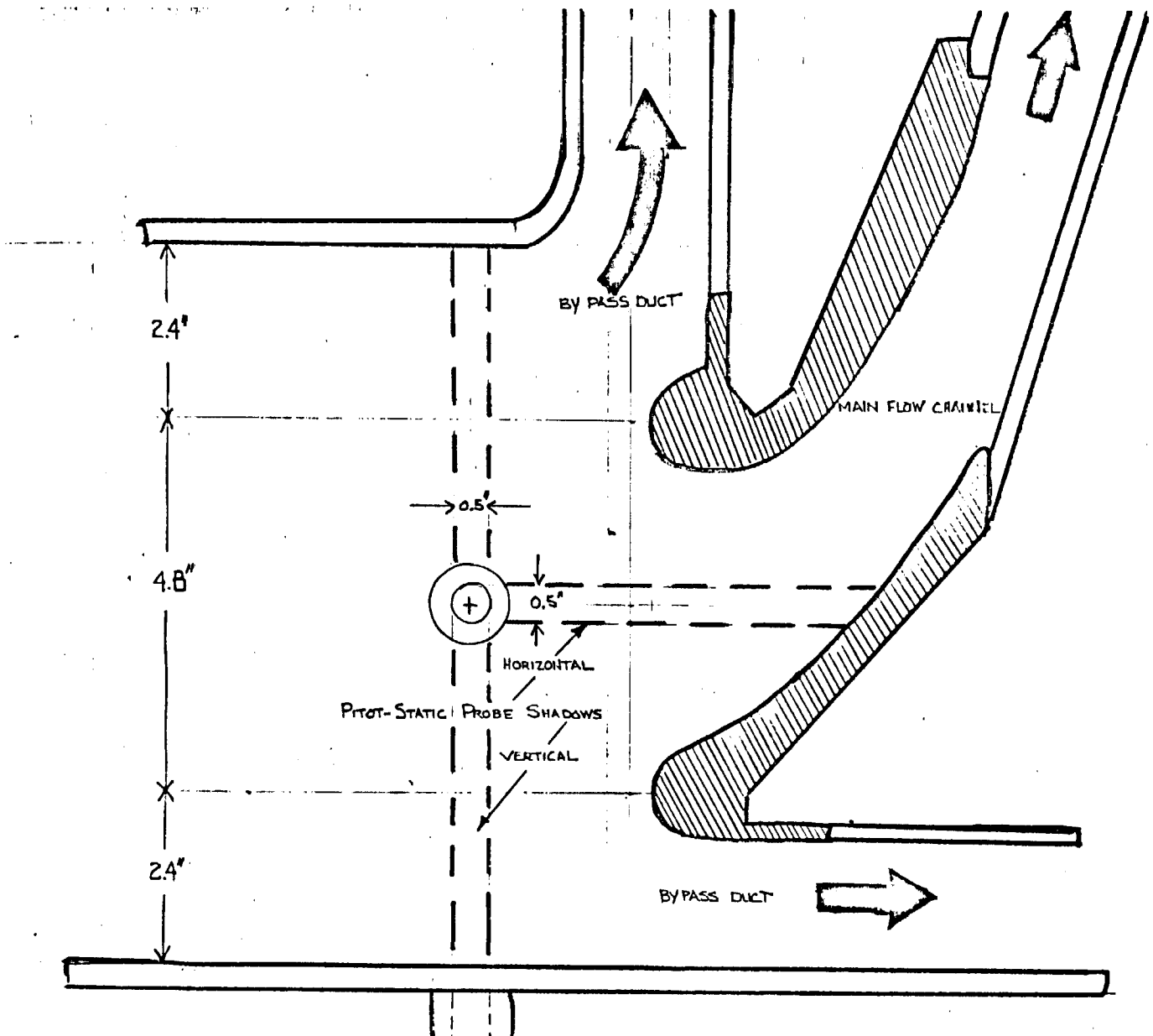

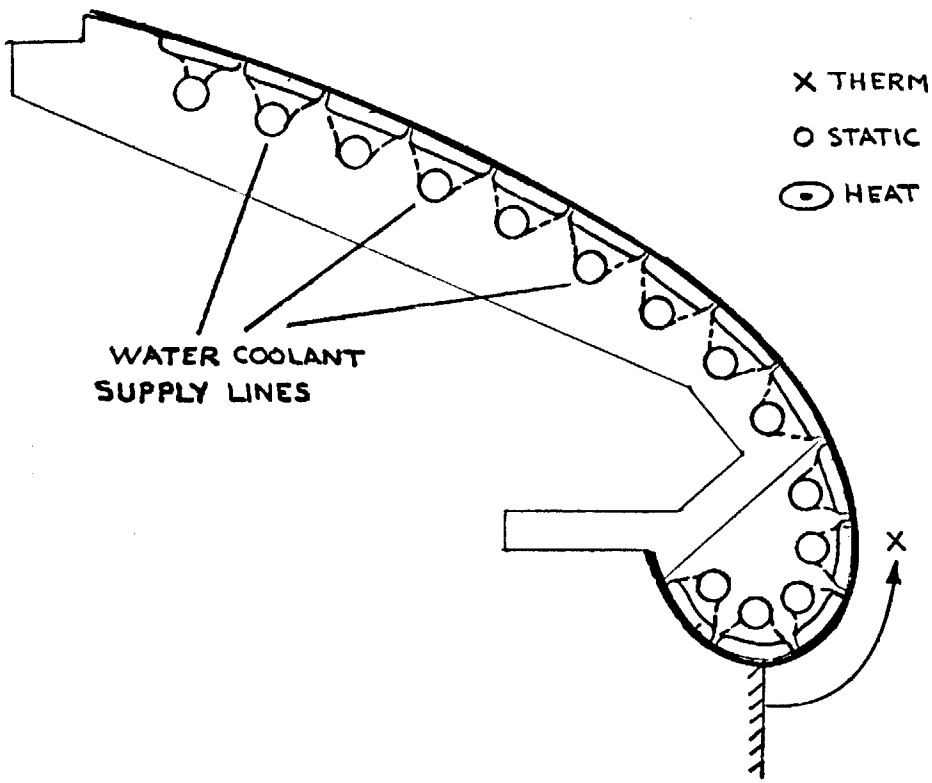

A. SUCTION SURFACE CONTOUR

X THERMOCOUPLE

O STATIC PRESSURE PORT

HEAT FLUX SENSOR

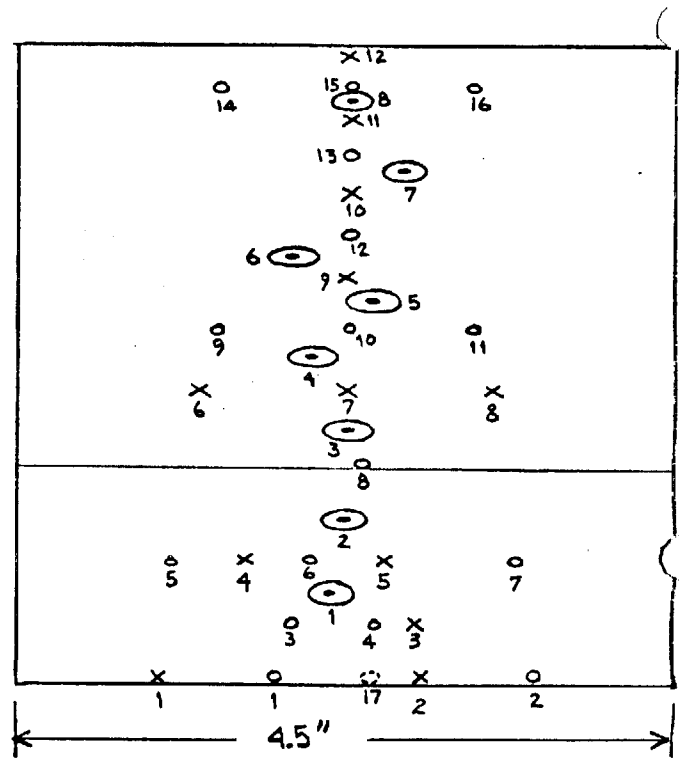

B. INSTRUMENTATION LOCATIONS

FIGURE 3.

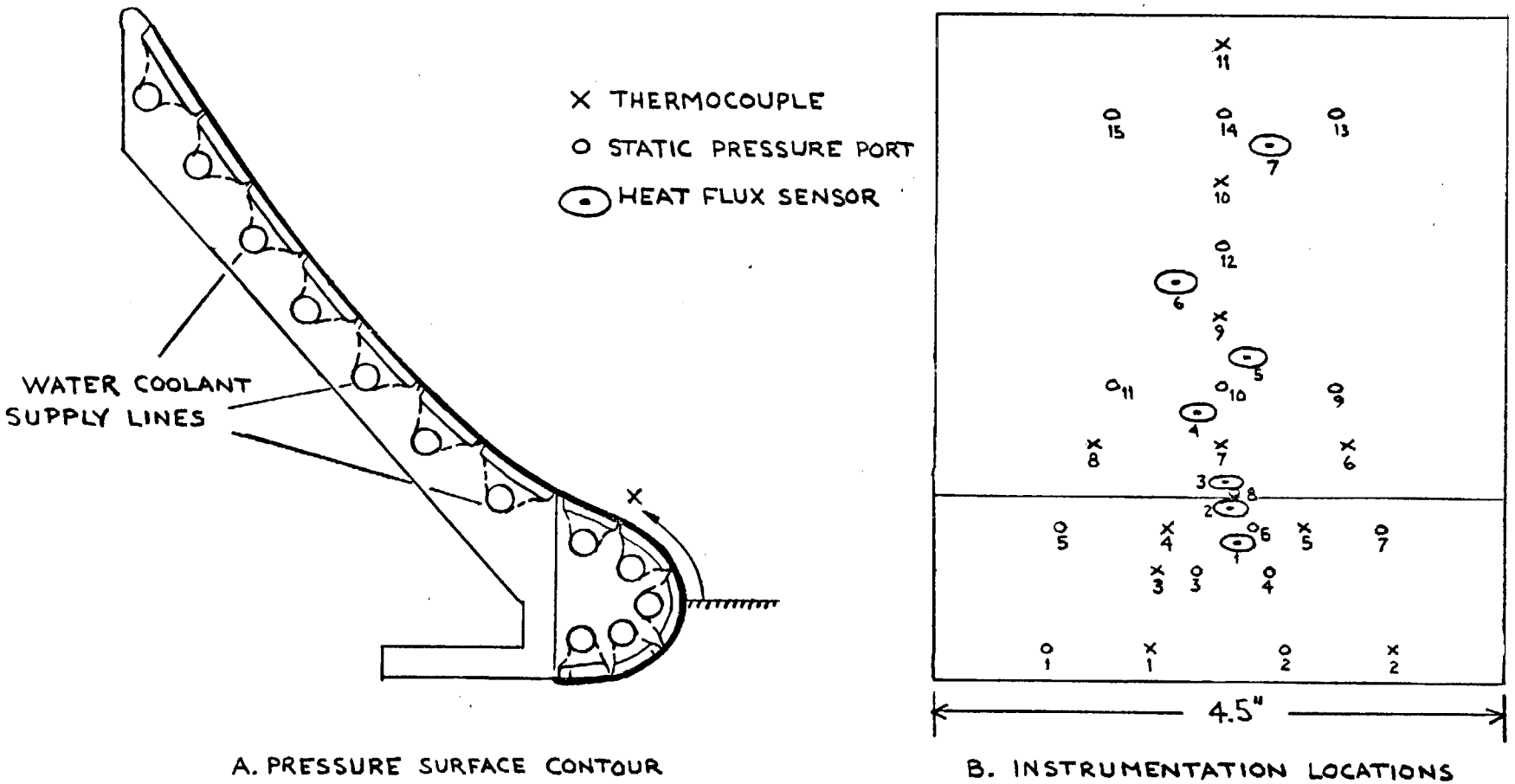

A. PRESSURE SURFACE CONTOUR

B. INSTRUMENTATION LOCATIONS

PRESSURE SURFACE INSTRUMENTATION
FIGURE 4.

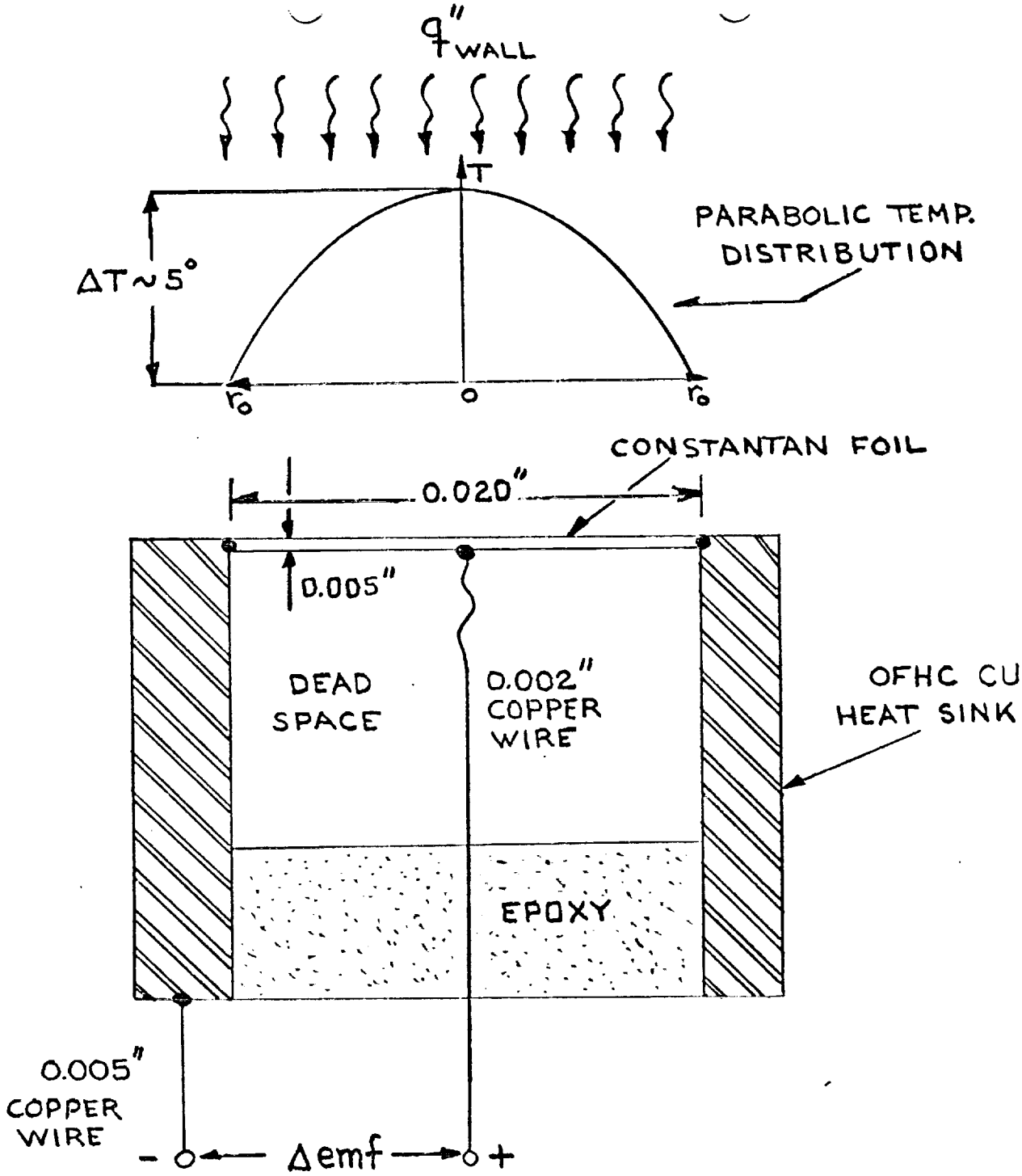

THIN FOIL HEAT FLUX TRANSDUCER

FIGURE 5.

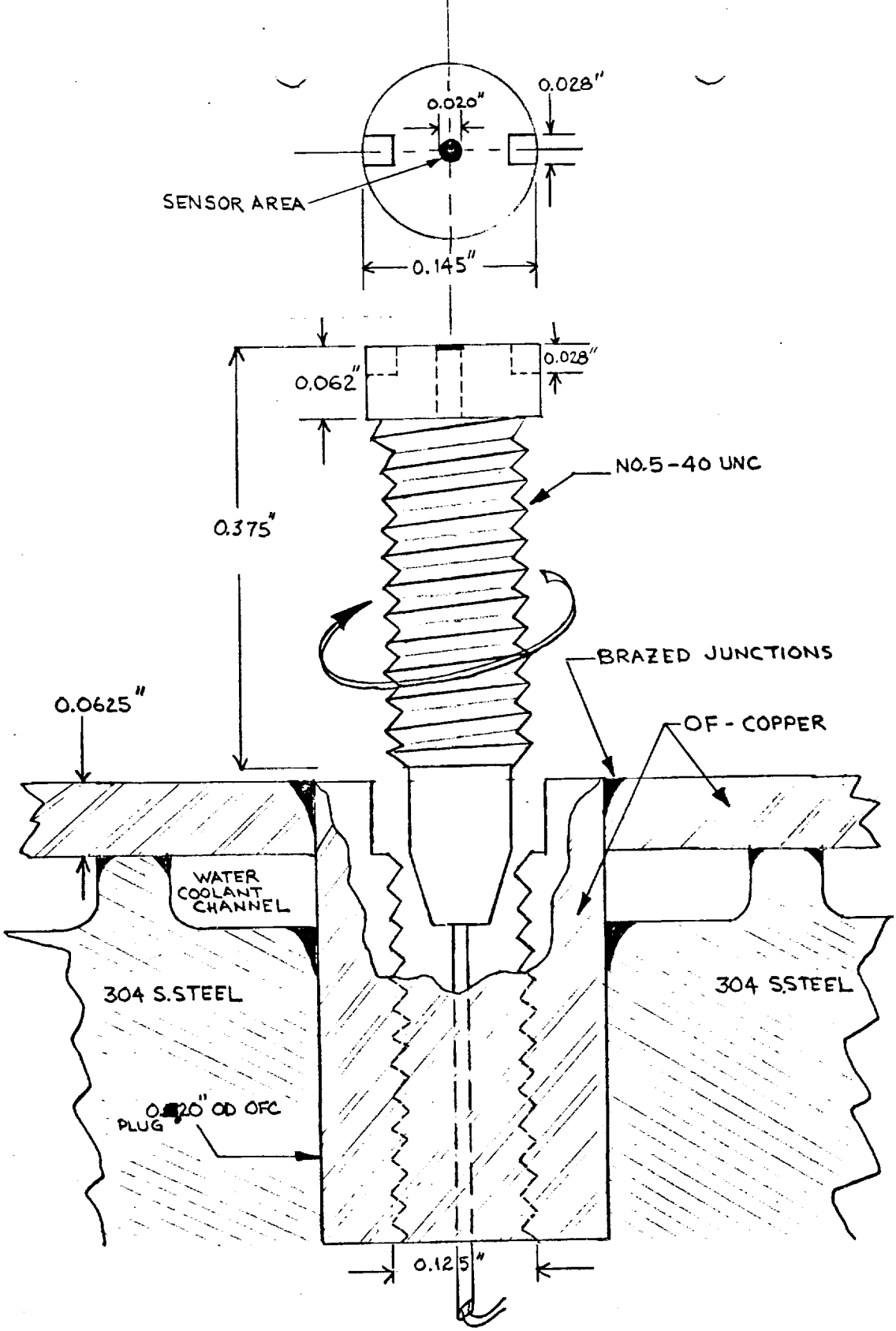

INSTALLATION TECHNIQUE OF HEAT FLUX TRANSDUCERS INTO TEST SURFACE

FIGURE 6.

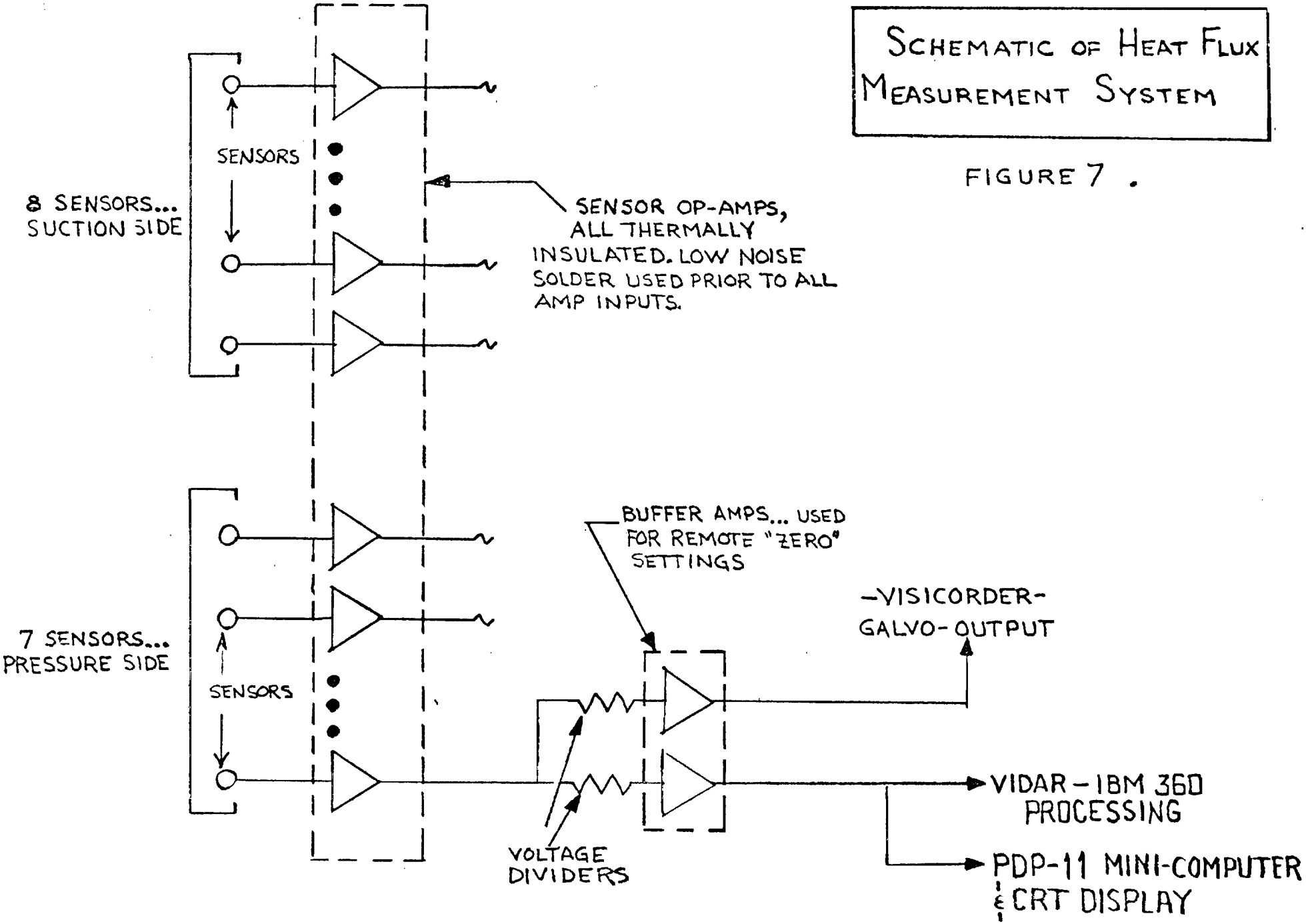

SCHEMATIC OF HEAT FLUX MEASUREMENT SYSTEM

FIGURE 7.

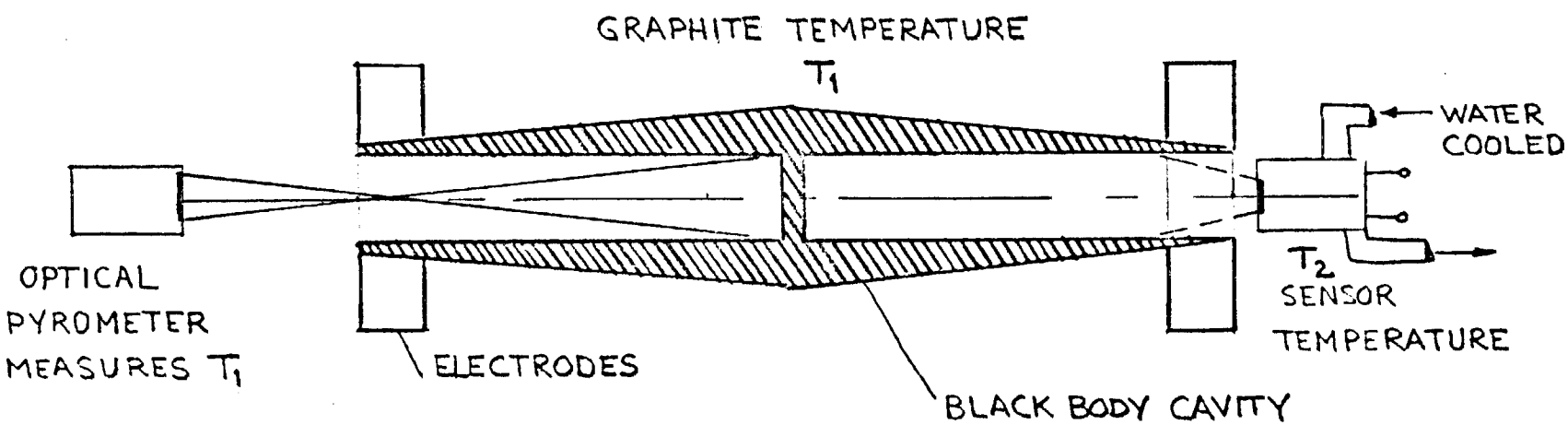

$$q'' = \sigma F_{12} \epsilon (T_1^4 - T_2^4)$$

CALIBRATION TECHNIQUE

FIGURE 8.

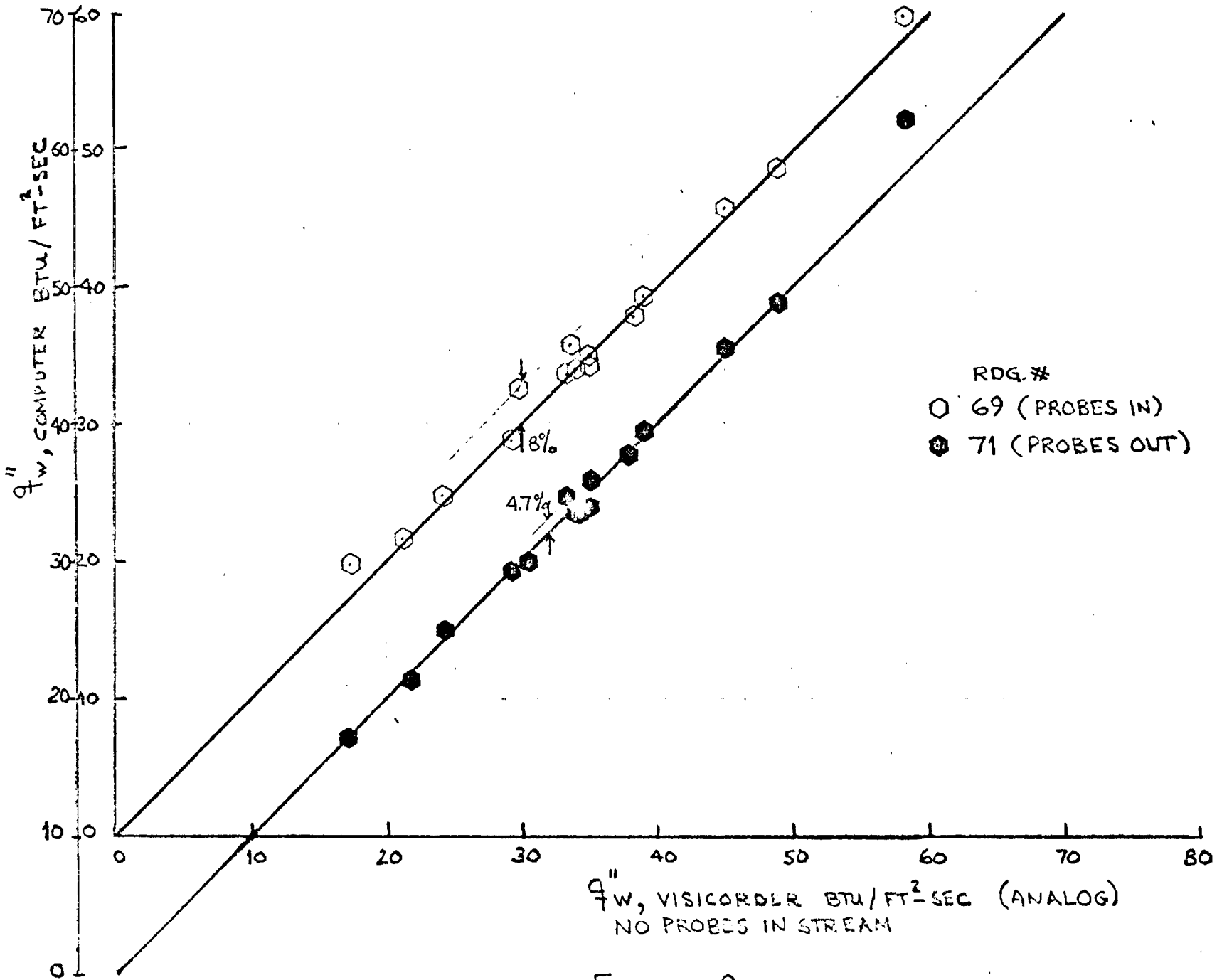
RDG. #
69 (PROBES IN)
71 (PROBES OUT)
8%
4.7%
q''_w, COMPUTER BTU/FT²-SEC
q''_w, VISICORDER BTU/FT²-SEC (ANALOG)
NO PROBES IN STREAM
0
10
20
30
40
50
60
70
80

FIGURE 9.

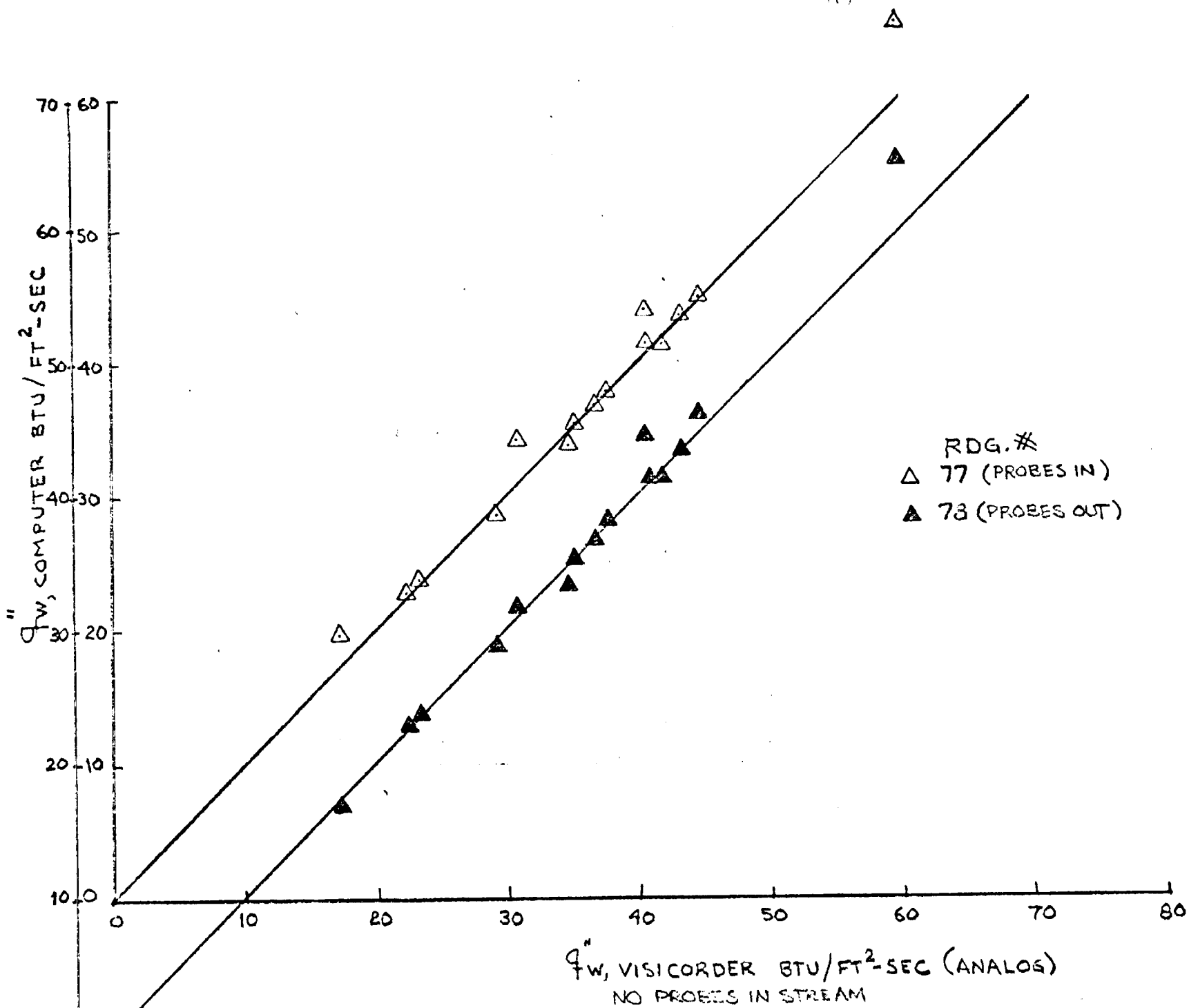
RDG.#
77 (PROBES IN)
78 (PROBES OUT)
q"w, COMPUTER BTU/FT²-SEC
q"w, VISICORDER BTU/FT²-SEC (ANALOG)
NO PROBES IN STREAM
0
10
20
30
40
50
60
70
80

FIGURE 10.

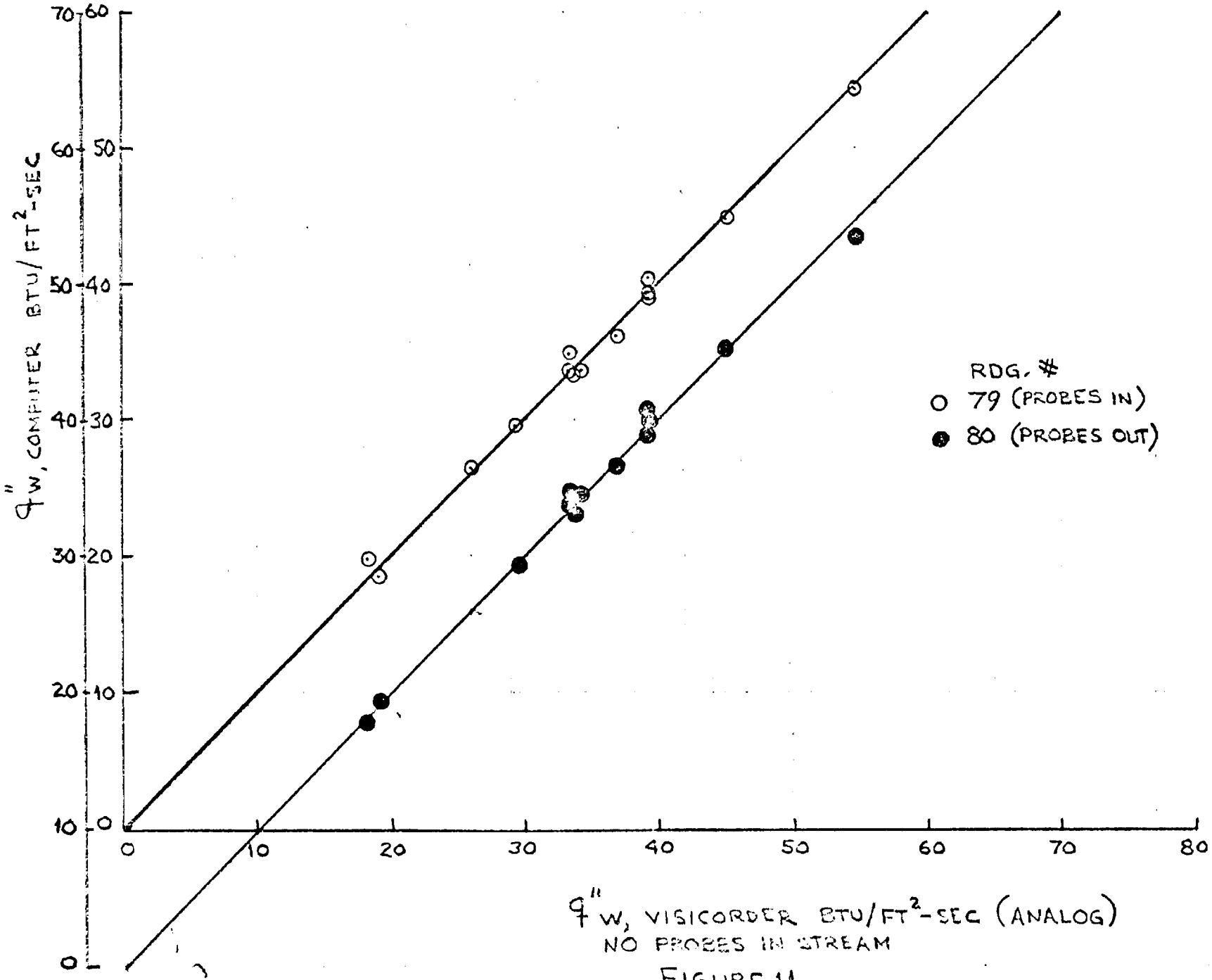
CALCULATED AND TO VISICORDER
RDG. #
79 (PROBES IN)
80 (PROBES OUT)
q"w, COMPUTER BTU/FT²-SEC
q"w, VISICORDER BTU/FT²-SEC (ANALOG)
NO PROBES IN STREAM
0
10
20
30
40
50
60
70
80

FIGURE 11.

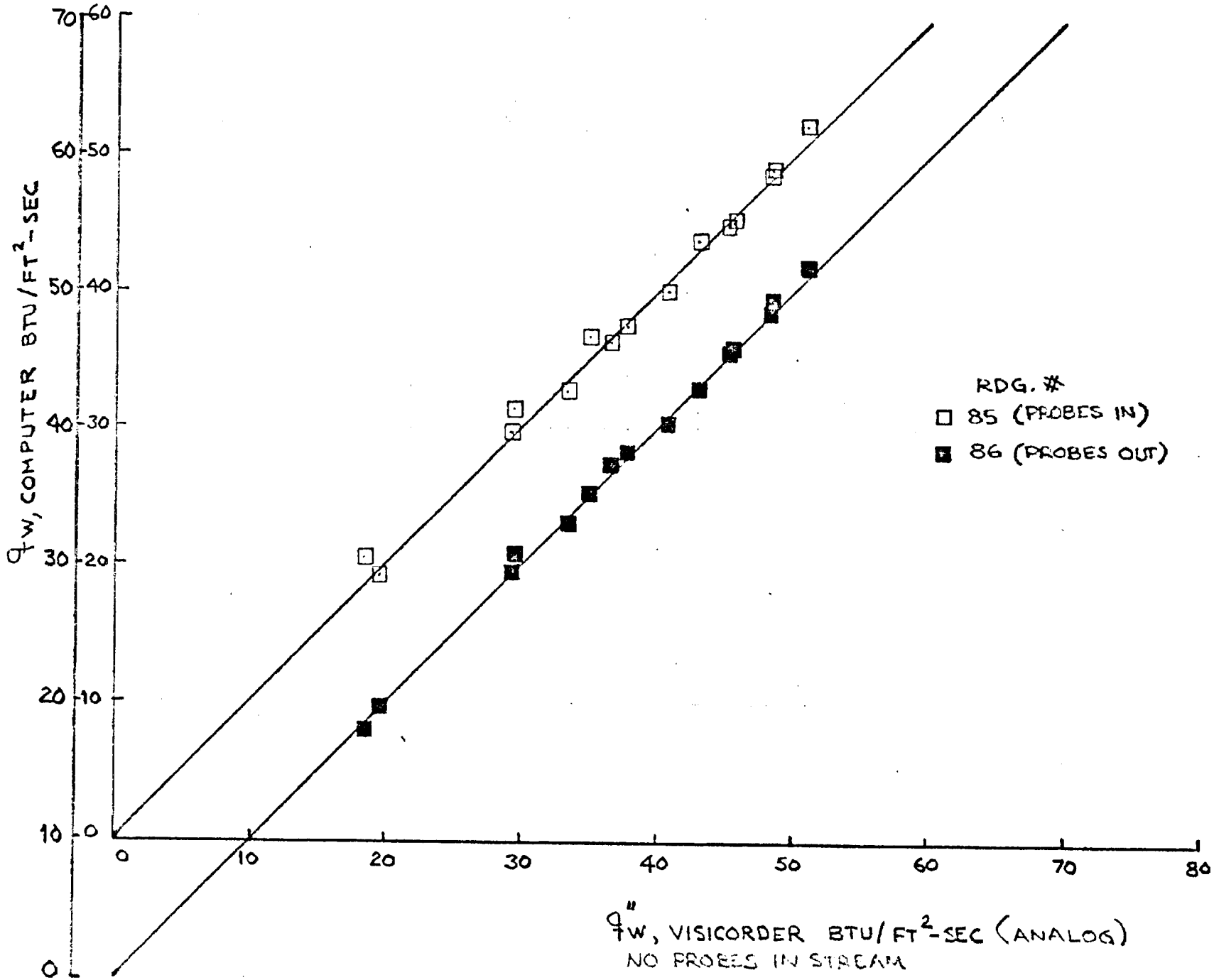
70
60
50
40
30
20
10
0
60
50
40
30
20
10
0
q_{tw}, COMPUTER BTU/FT^2-SEC
0
10
20
30
40
50
60
70
80
q''_{tw}, VISICORDER BTU/FT^2-SEC (ANALOG)
NO PROBES IN STREAM
RDG. #
85 (PROBES IN)
86 (PROBES OUT)

FIGURE 12.

Rdg 69

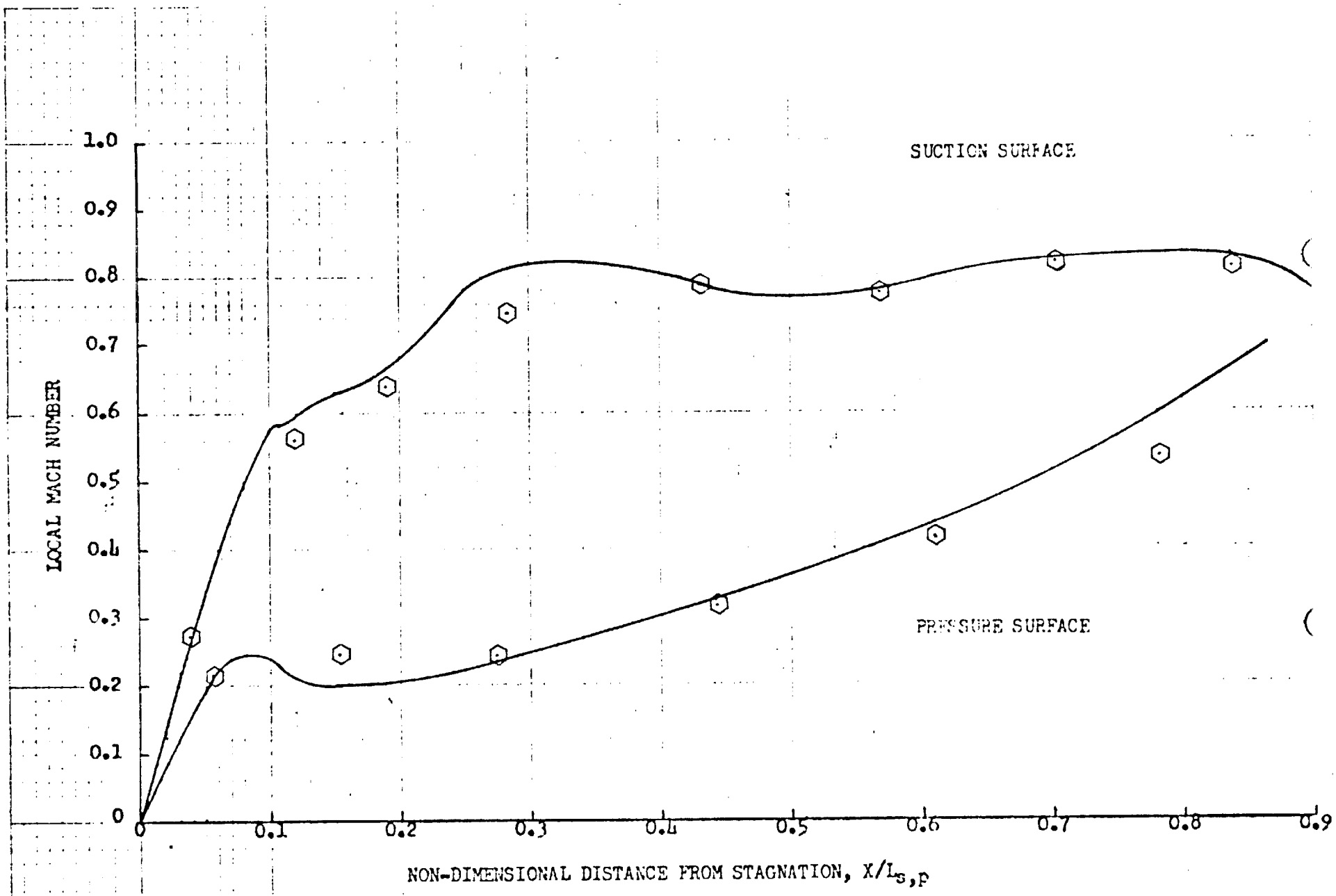

FIGURE 13.

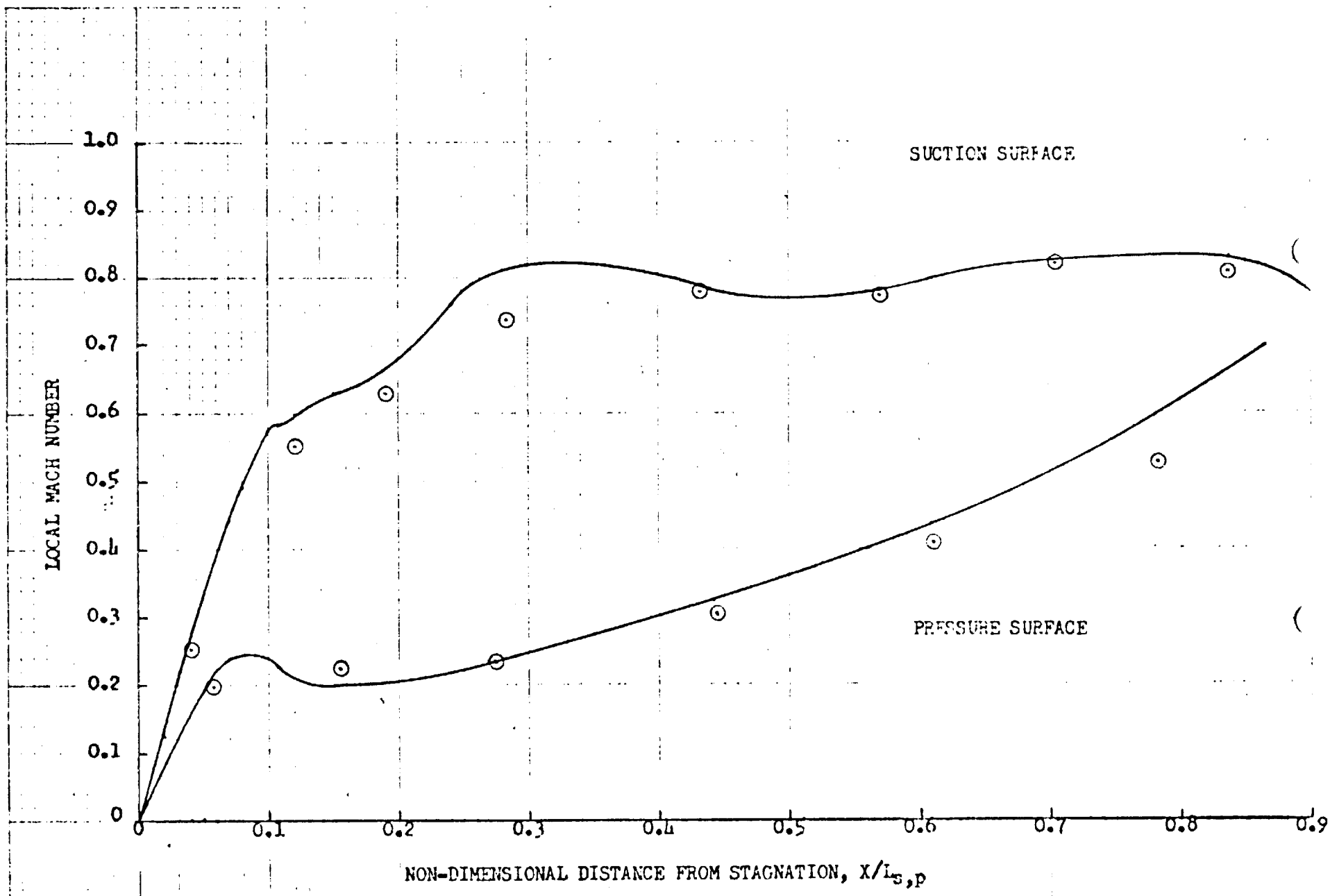
SUCTION SURFACE
PRESSURE SURFACE
LOCAL MACH NUMBER
1.0
0.9
0.8
0.7
0.6
0.5
0.4
0.3
0.2
0.1
0
0.1
0.2
0.3
0.4
0.5
0.6
0.7
0.8
0.9
NON-DIMENSIONAL DISTANCE FROM STAGNATION, $X/L_{s,p}$

FIGURE 14.

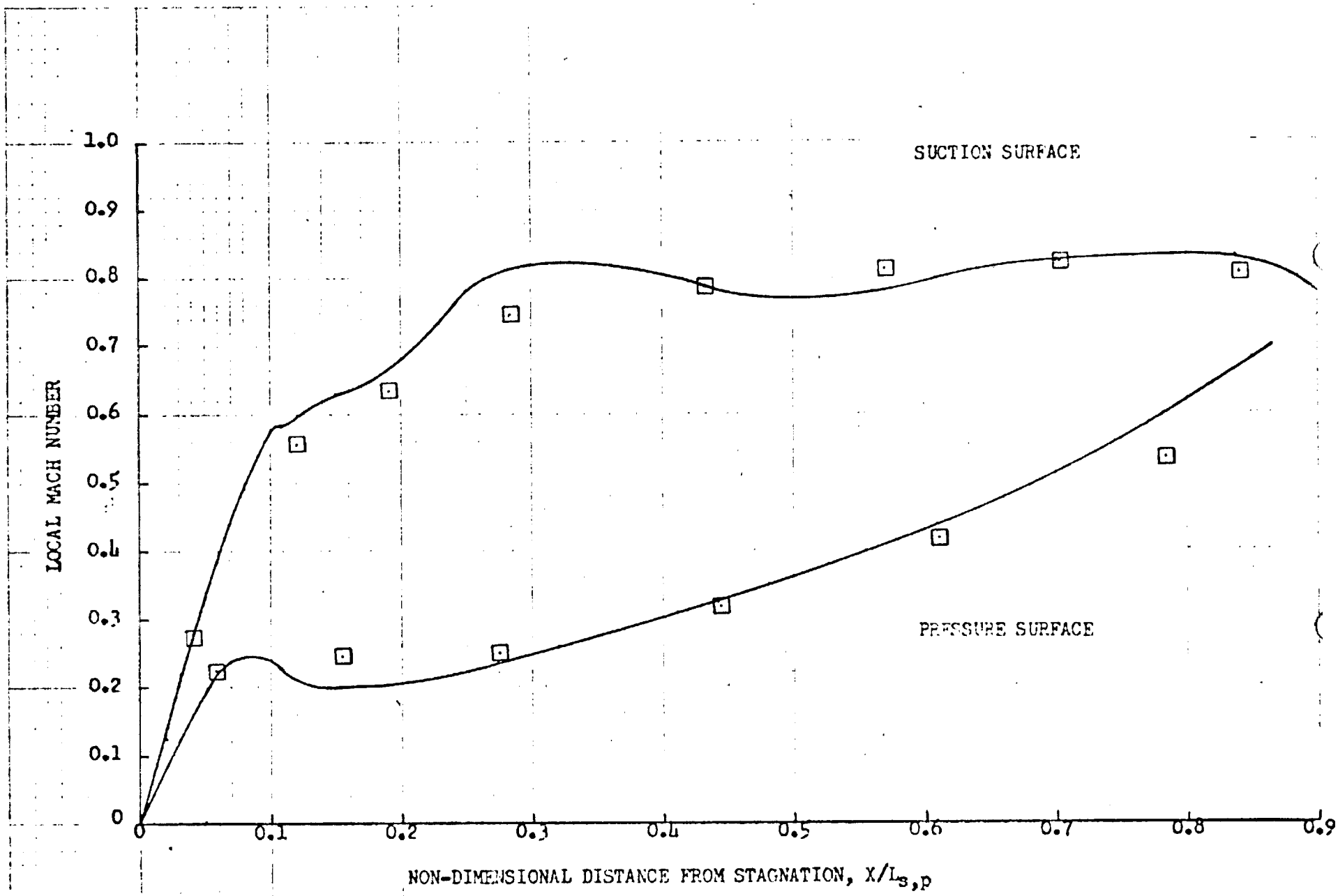
SUCTION SURFACE
PRESSURE SURFACE
LOCAL MACH NUMBER
1.0
0.9
0.8
0.7
0.6
0.5
0.4
0.3
0.2
0.1
0
0.1
0.2
0.3
0.4
0.5
0.6
0.7
0.8
0.9
NON-DIMENSIONAL DISTANCE FROM STAGNATION, $X/L_{s,p}$

FIGURE 15.

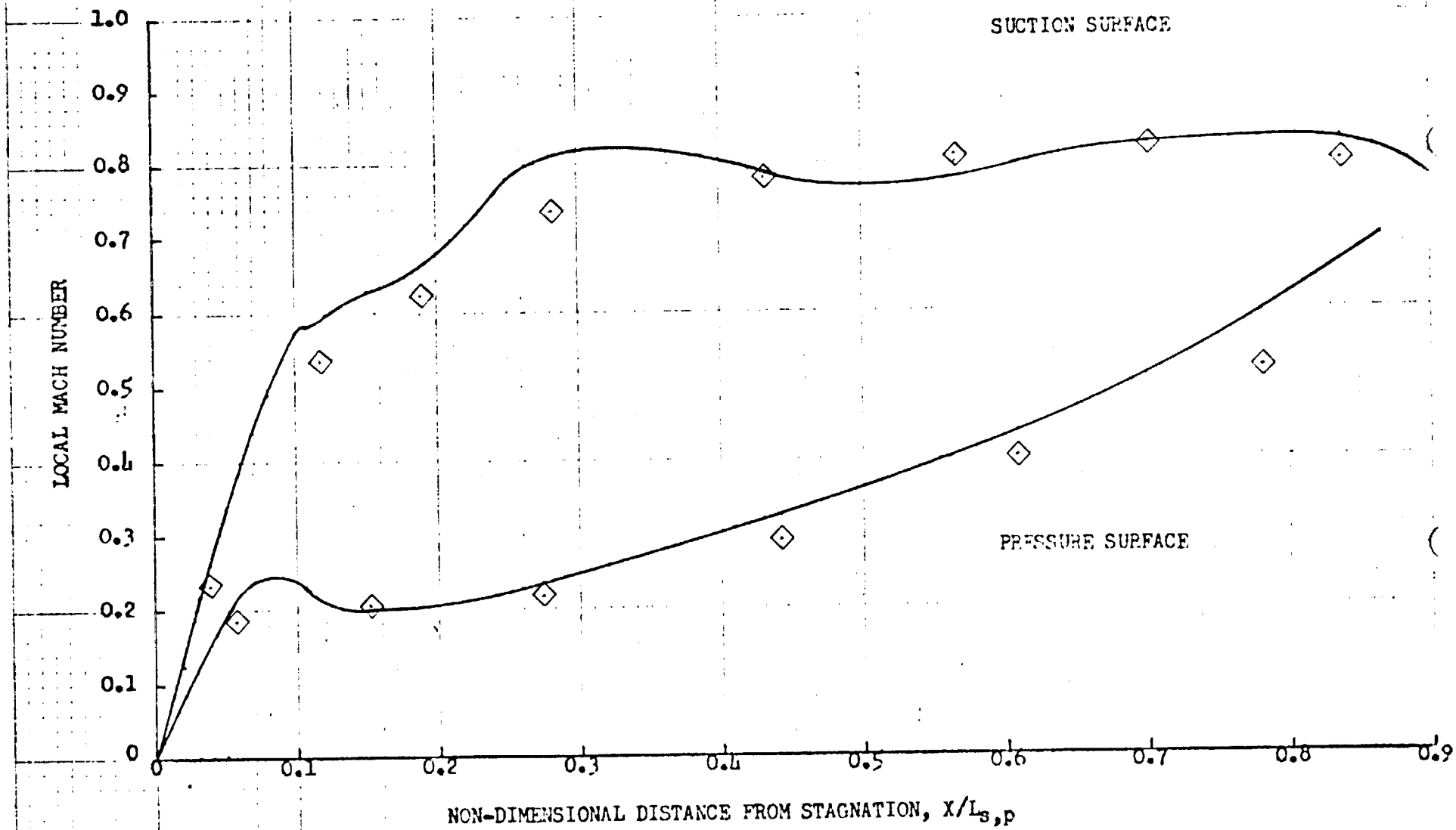
SUCTION SURFACE
PRESSURE SURFACE
LOCAL MACH NUMBER
1.0
0.9
0.8
0.7
0.6
0.5
0.4
0.3
0.2
0.1
0
0.1
0.2
0.3
0.4
0.5
0.6
0.7
0.8
0.9
NON-DIMENSIONAL DISTANCE FROM STAGNATION, $X/L_{s,p}$

FIGURE 16.

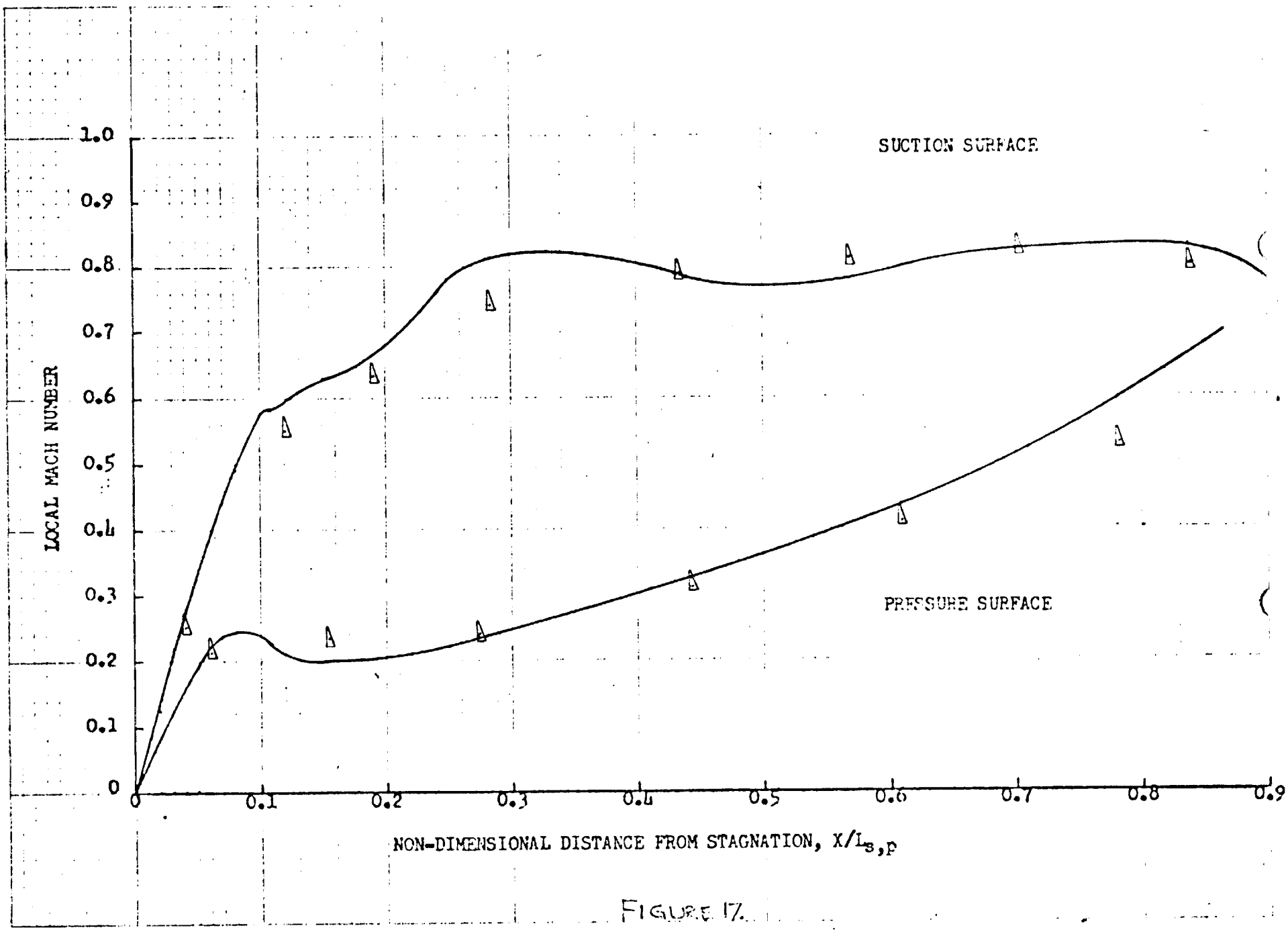
SUCTION SURFACE
PRESSURE SURFACE
LOCAL MACH NUMBER
1.0
0.9
0.8
0.7
0.6
0.5
0.4
0.3
0.2
0.1
0
0.1
0.2
0.3
0.4
0.5
0.6
0.7
0.8
0.9
NON-DIMENSIONAL DISTANCE FROM STAGNATION, $X/L_{s,p}$

FIGURE 17.

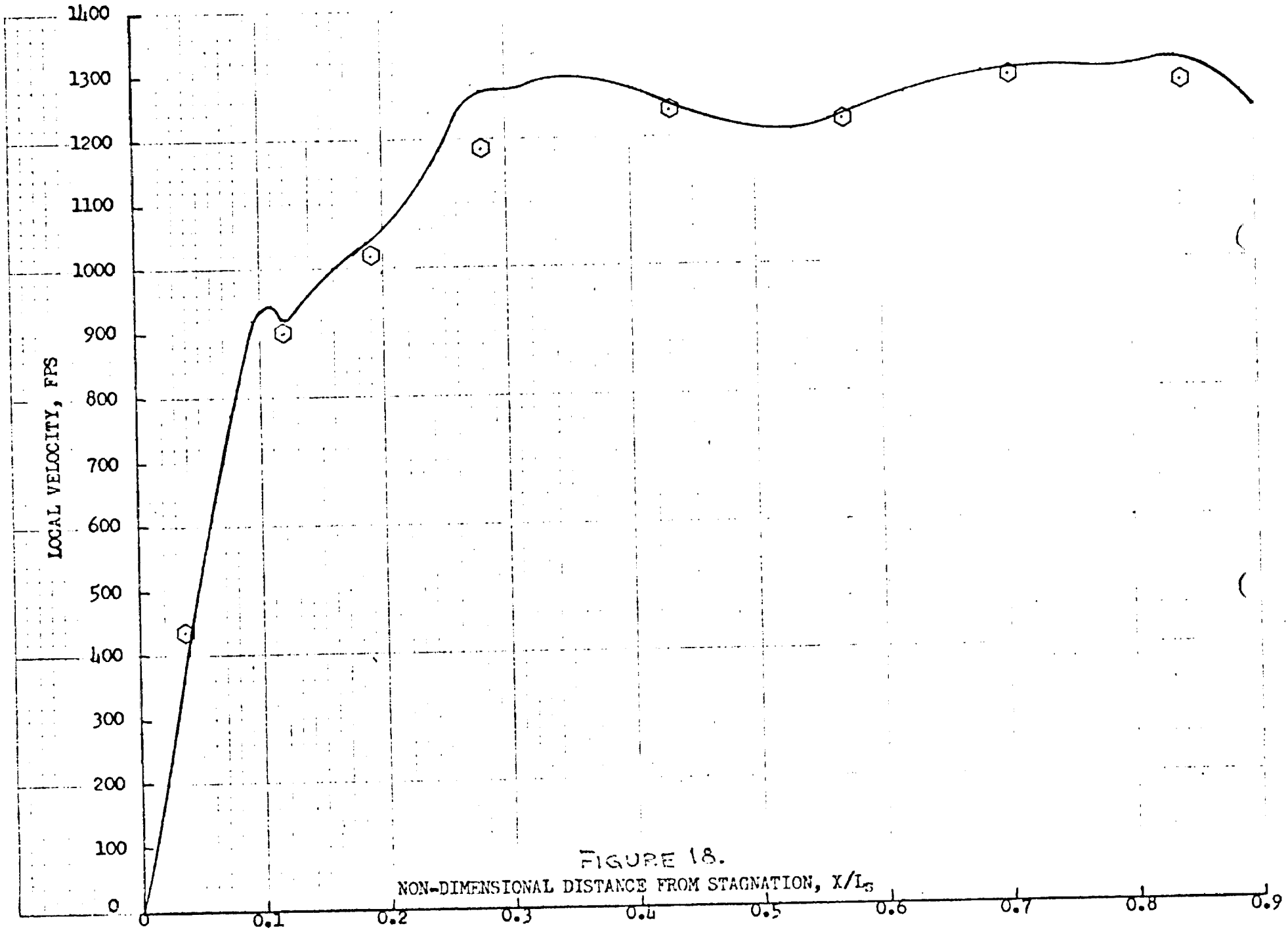
LOCAL VELOCITY, FPS
1400
1300
1200
1100
1000
900
800
700
600
500
400
300
200
100
0
0
0.1
0.2
0.3
0.4
0.5
0.6
0.7
0.8
0.9
NON-DIMENSIONAL DISTANCE FROM STAGNATION, X/L

FIGURE 18.

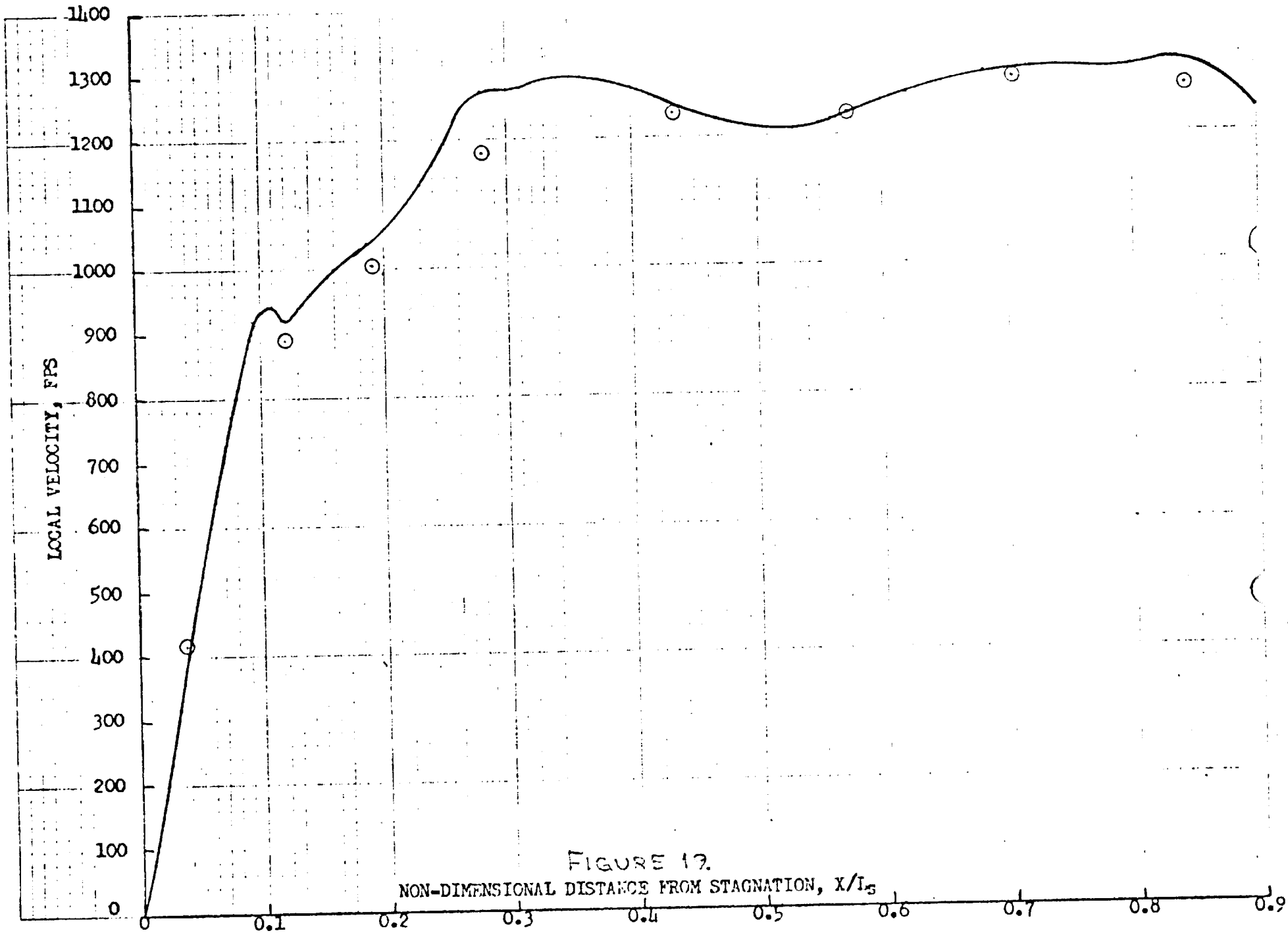
LOCAL VELOCITY, FPS
1400
1300
1200
1100
1000
900
800
700
600
500
400
300
200
100
0
0
0.1
0.2
0.3
0.4
0.5
0.6
0.7
0.8
0.9
NON-DIMENSIONAL DISTANCE FROM STAGNATION, X/L_S

FIGURE 19.

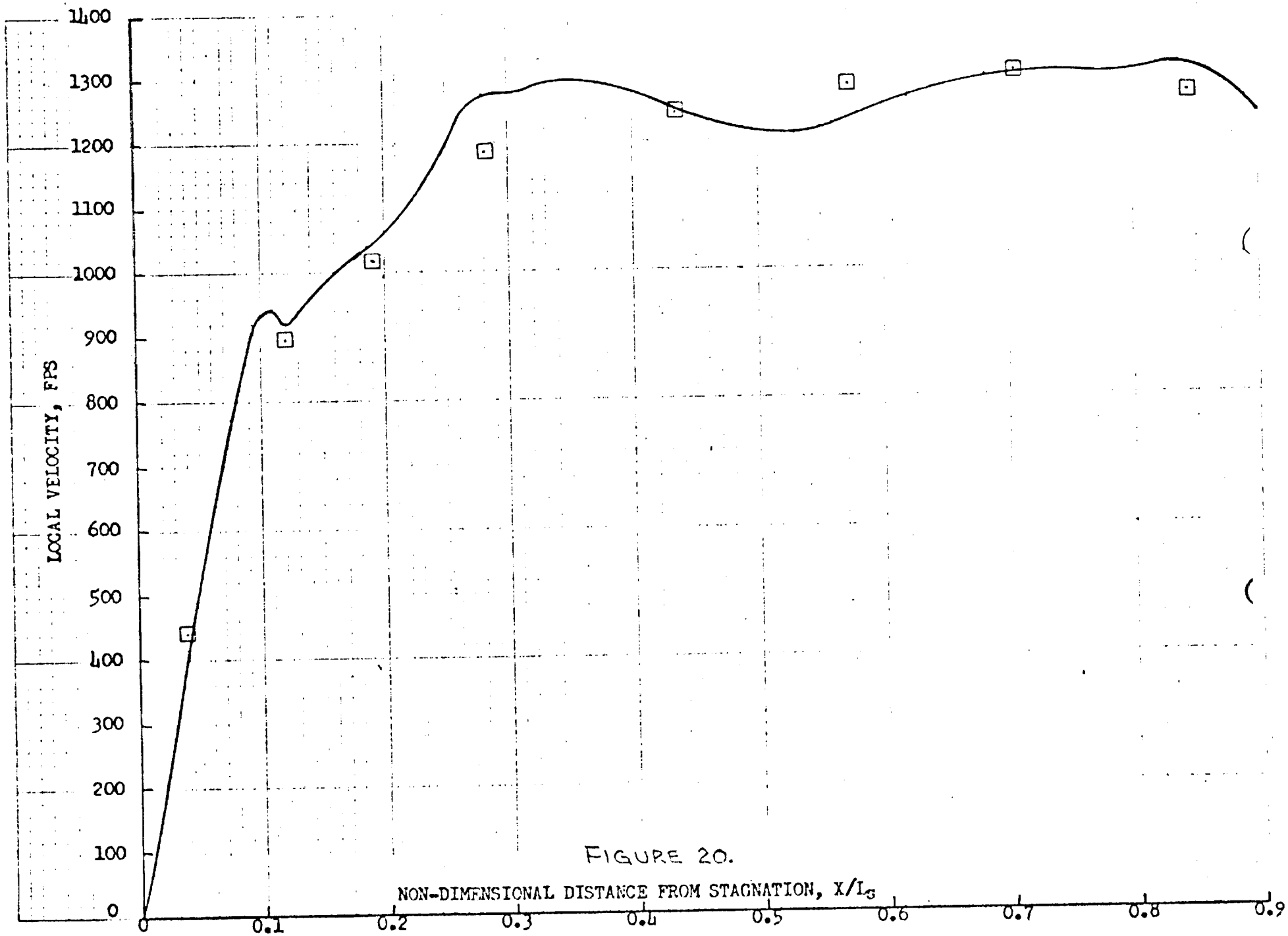
LOCAL VELOCITY, FPS
1400
1300
1200
1100
1000
900
800
700
600
500
400
300
200
100
0
NON-DIMENSIONAL DISTANCE FROM STAGNATION, X/L_S
0
0.1
0.2
0.3
0.4
0.5
0.6
0.7
0.8
0.9

FIGURE 20.

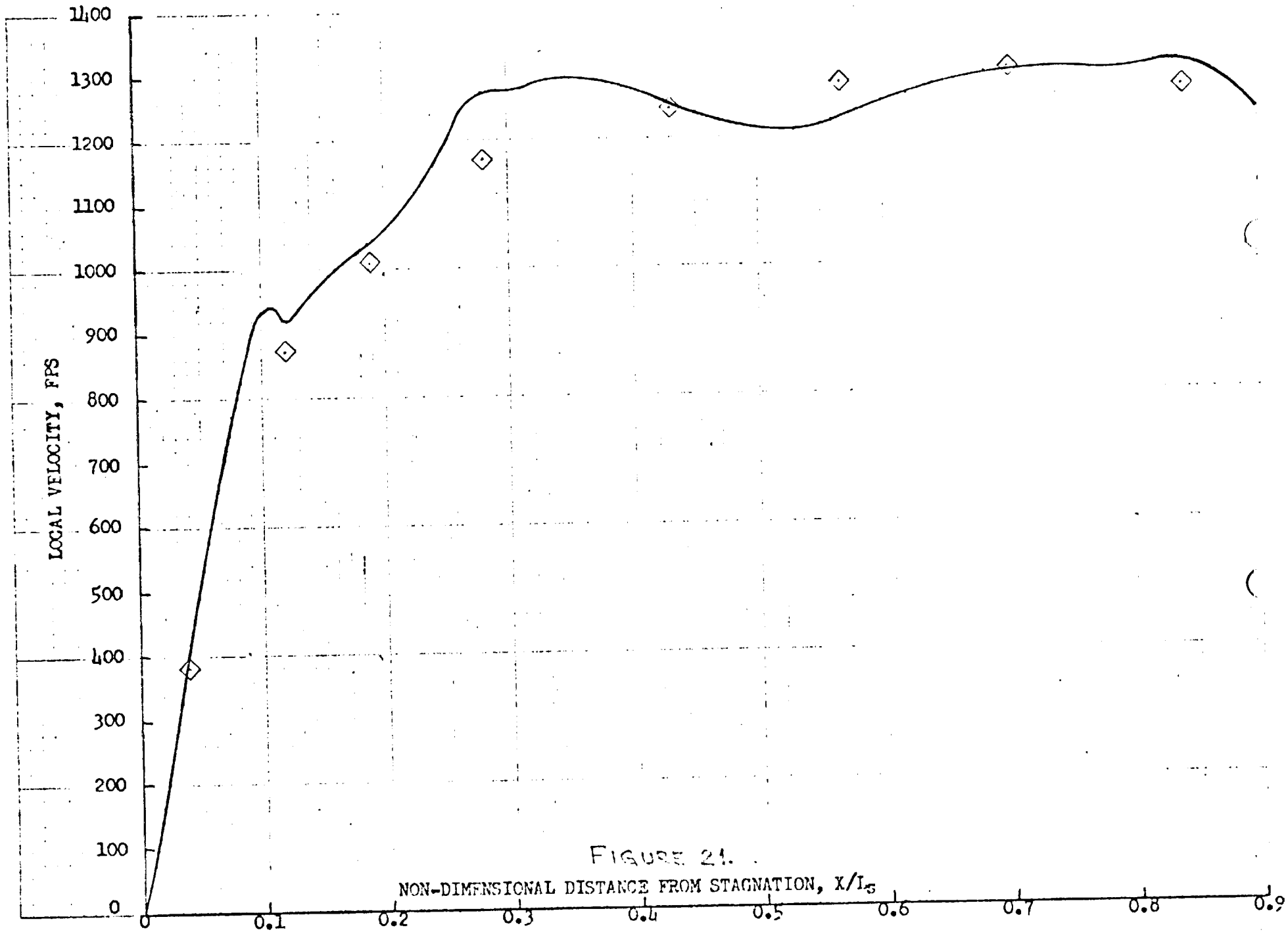
LOCAL VELOCITY, FPS
1400
1300
1200
1100
1000
900
800
700
600
500
400
300
200
100
0
NON-DIMENSIONAL DISTANCE FROM STAGNATION, X/L_S
0
0.1
0.2
0.3
0.4
0.5
0.6
0.7
0.8
0.9

FIGURE 21.

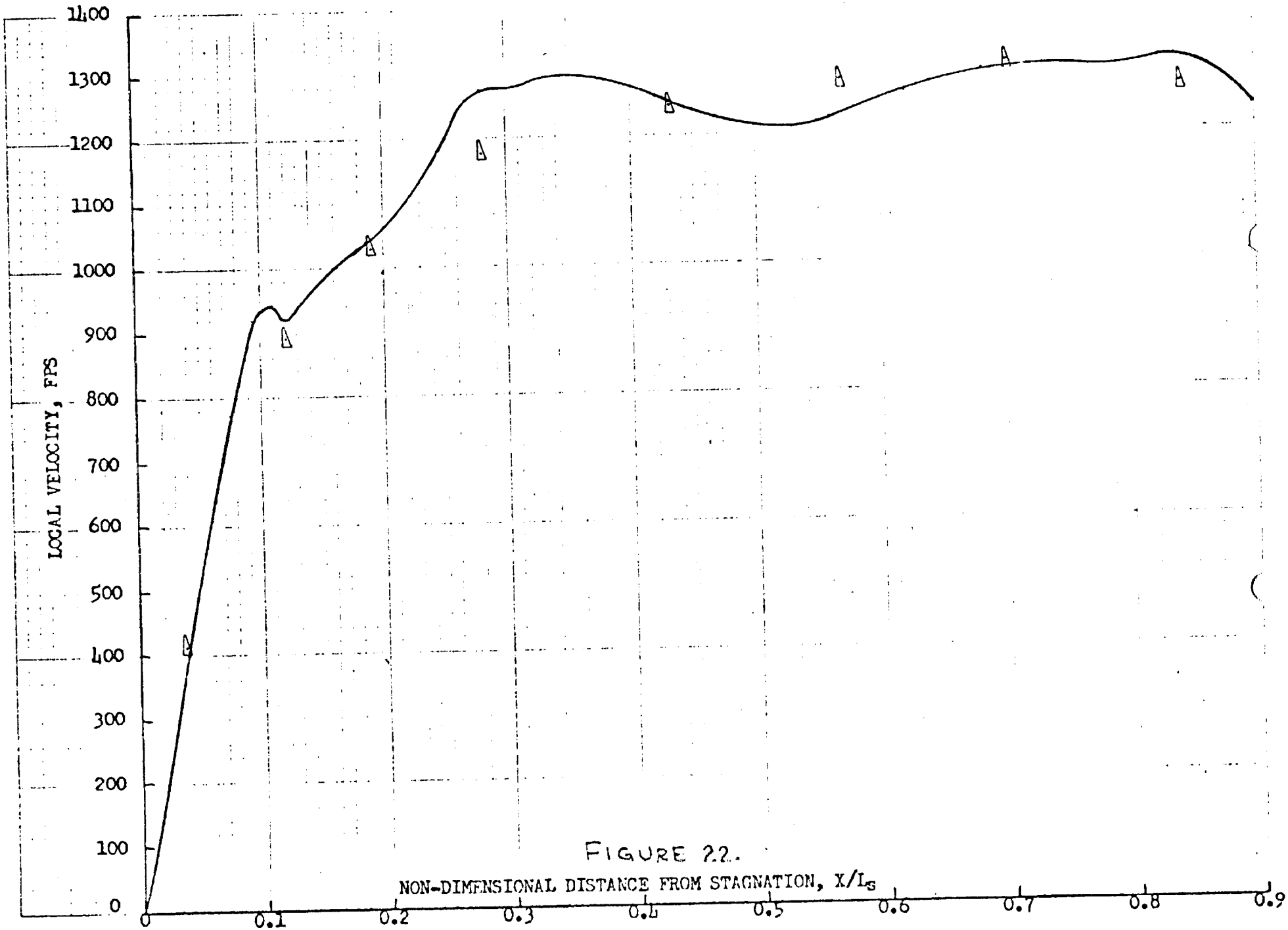
LOCAL VELOCITY, FPS
1400
1300
1200
1100
1000
900
800
700
600
500
400
300
200
100
0
0
0.1
0.2
0.3
0.4
0.5
0.6
0.7
0.8
0.9
NON-DIMENSIONAL DISTANCE FROM STAGNATION, X/L_S

FIGURE 22.

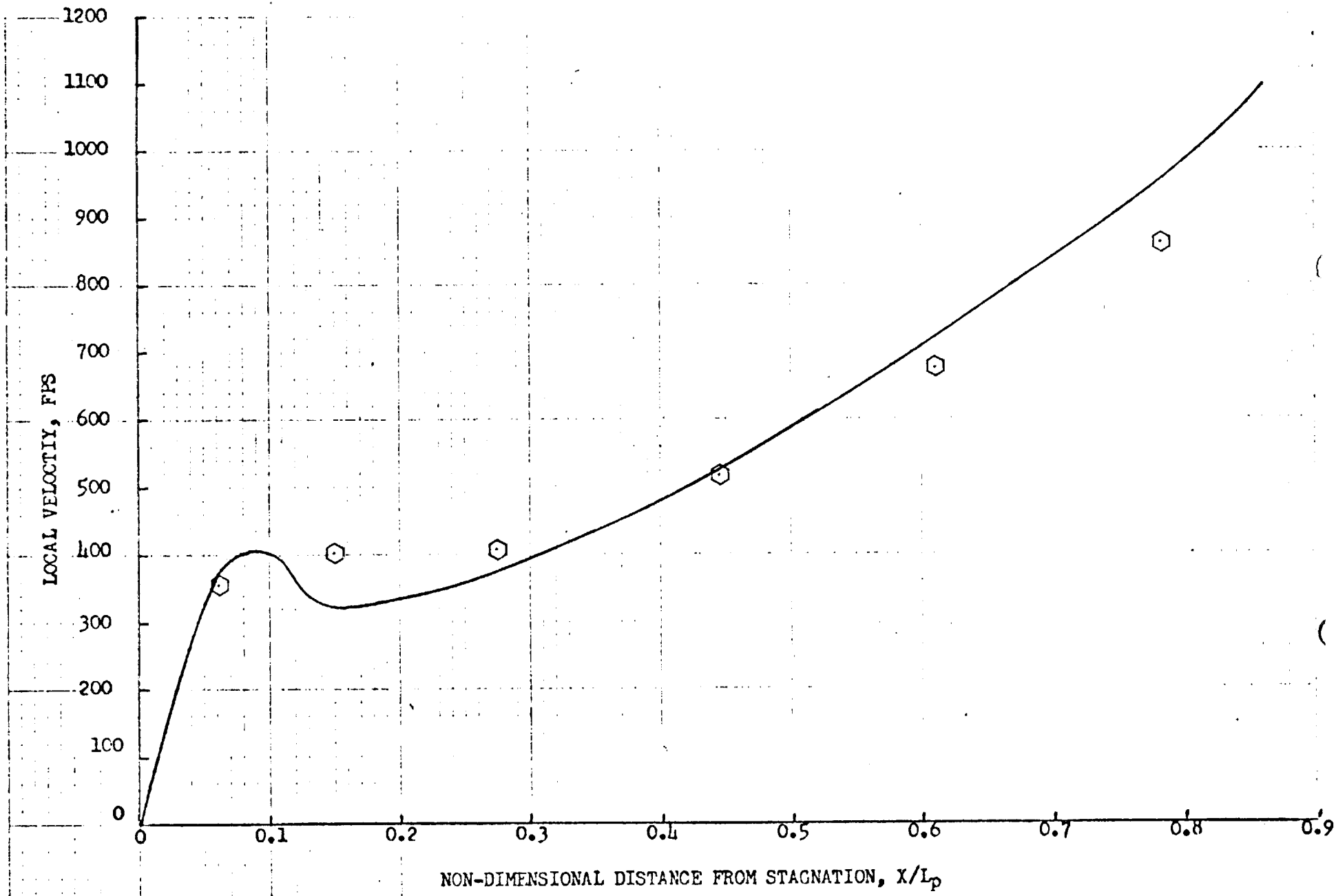
1200
1100
1000
900
800
700
600
500
400
300
200
100
0
LOCAL VELOCTIY, FPS
0
0.1
0.2
0.3
0.4
0.5
0.6
0.7
0.8
0.9
NON-DIMENSIONAL DISTANCE FROM STAGNATION, X/Lp

FIGURE 23.

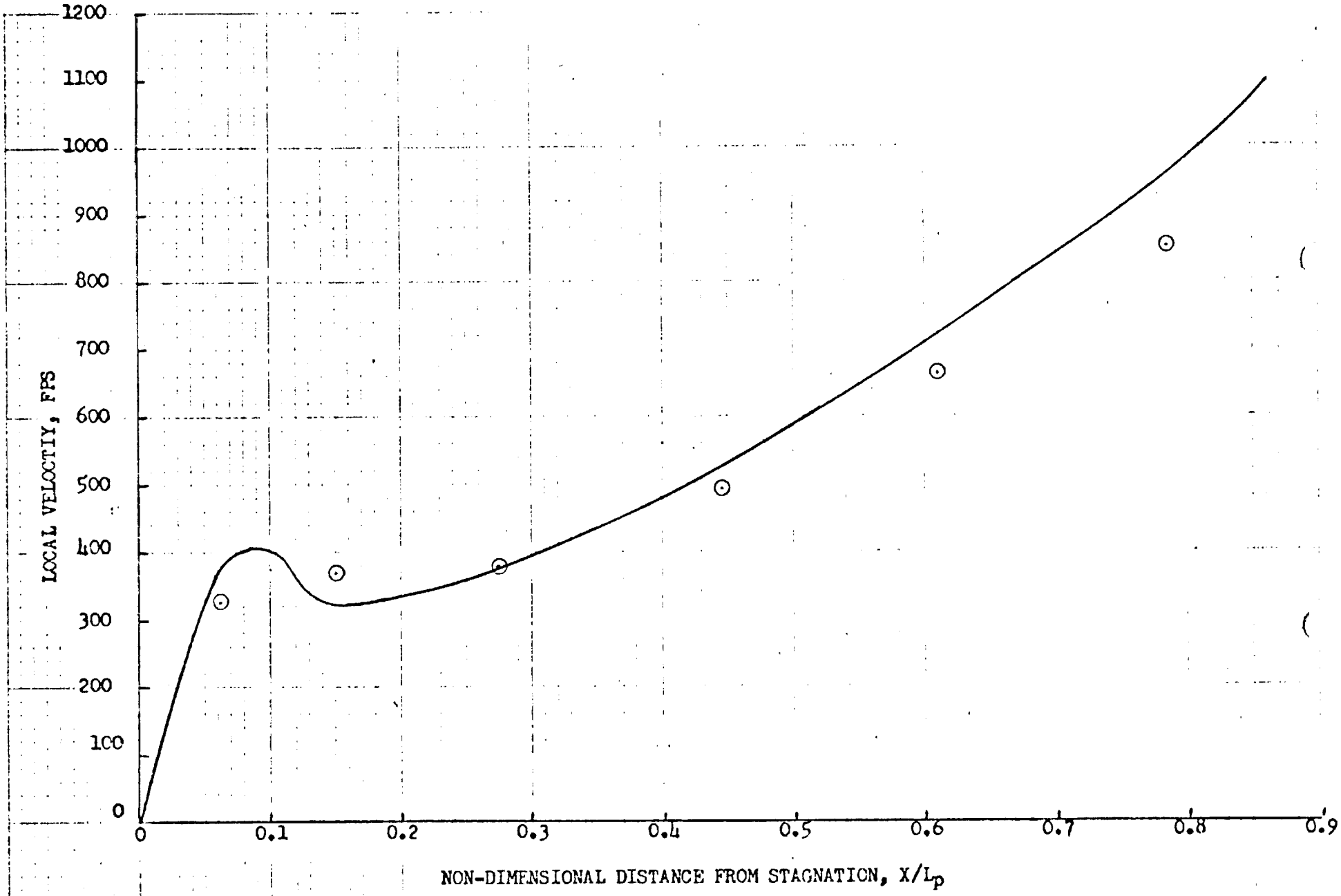
1200
1100
1000
900
800
700
600
500
400
300
200
100
0
LOCAL VELOCTIY, FPS
0
0.1
0.2
0.3
0.4
0.5
0.6
0.7
0.8
0.9
NON-DIMENSIONAL DISTANCE FROM STAGNATION, X/Lp

FIGURE 24.

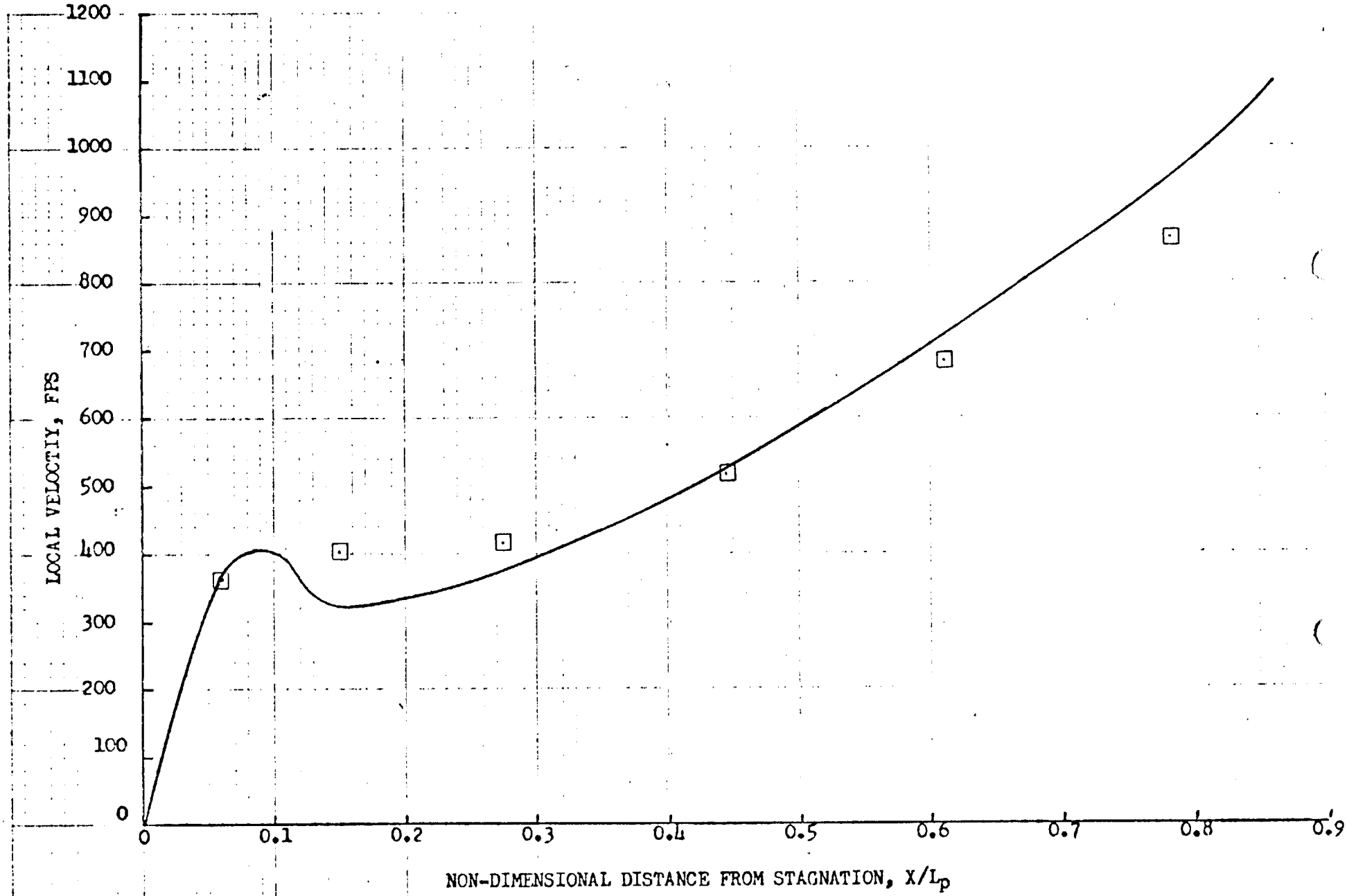
1200
1100
1000
900
800
700
600
500
400
300
200
100
0
LOCAL VELOCTIY, FPS
0
0.1
0.2
0.3
0.4
0.5
0.6
0.7
0.8
0.9
NON-DIMENSIONAL DISTANCE FROM STAGNATION, X/Lp

FIGURE 25.

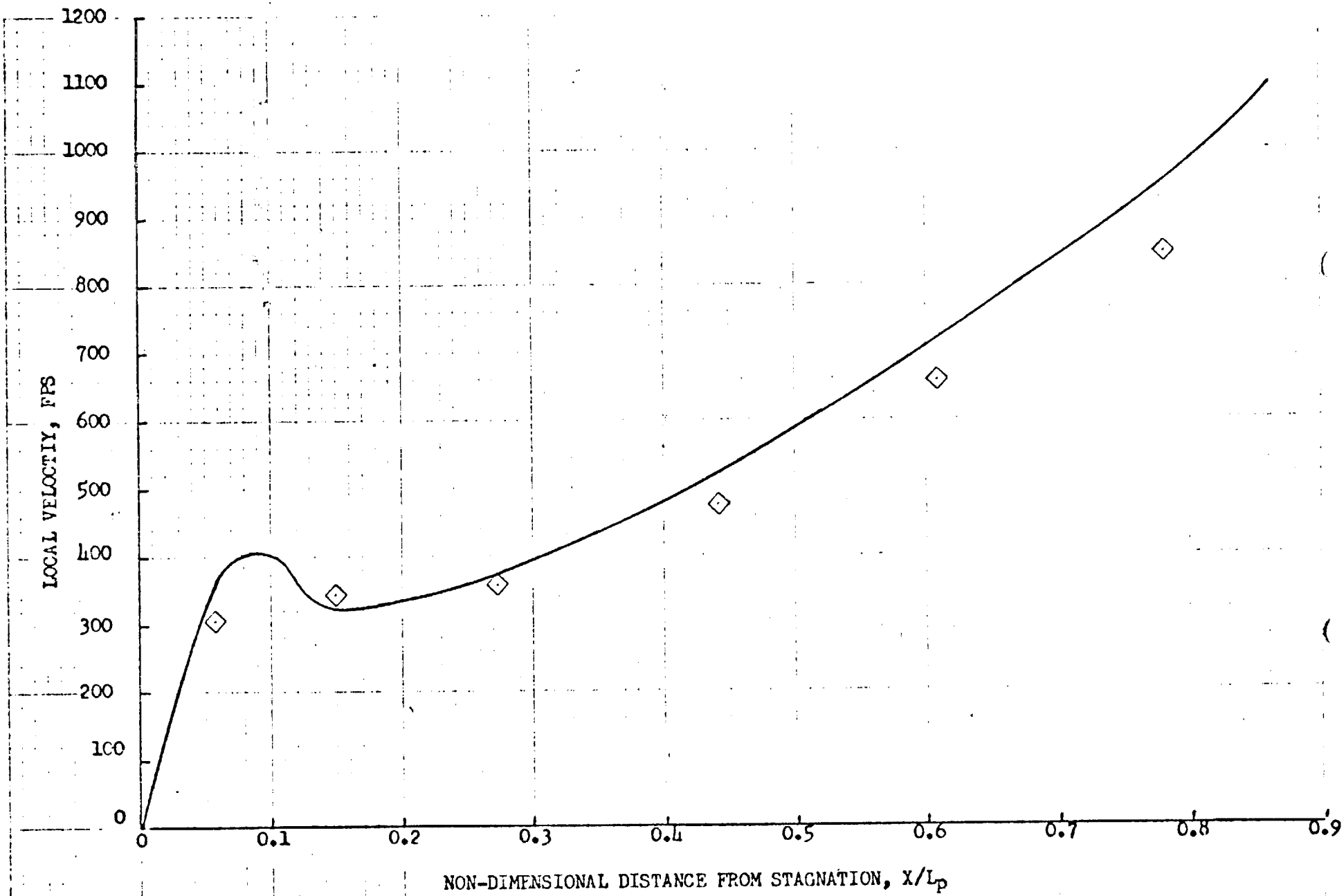
1200
1100
1000
900
800
700
600
500
400
300
200
100
0
LOCAL VELOCTIY, FPS
0
0.1
0.2
0.3
0.4
0.5
0.6
0.7
0.8
0.9
NON-DIMENSIONAL DISTANCE FROM STAGNATION, X/Lp

FIGURE 26.

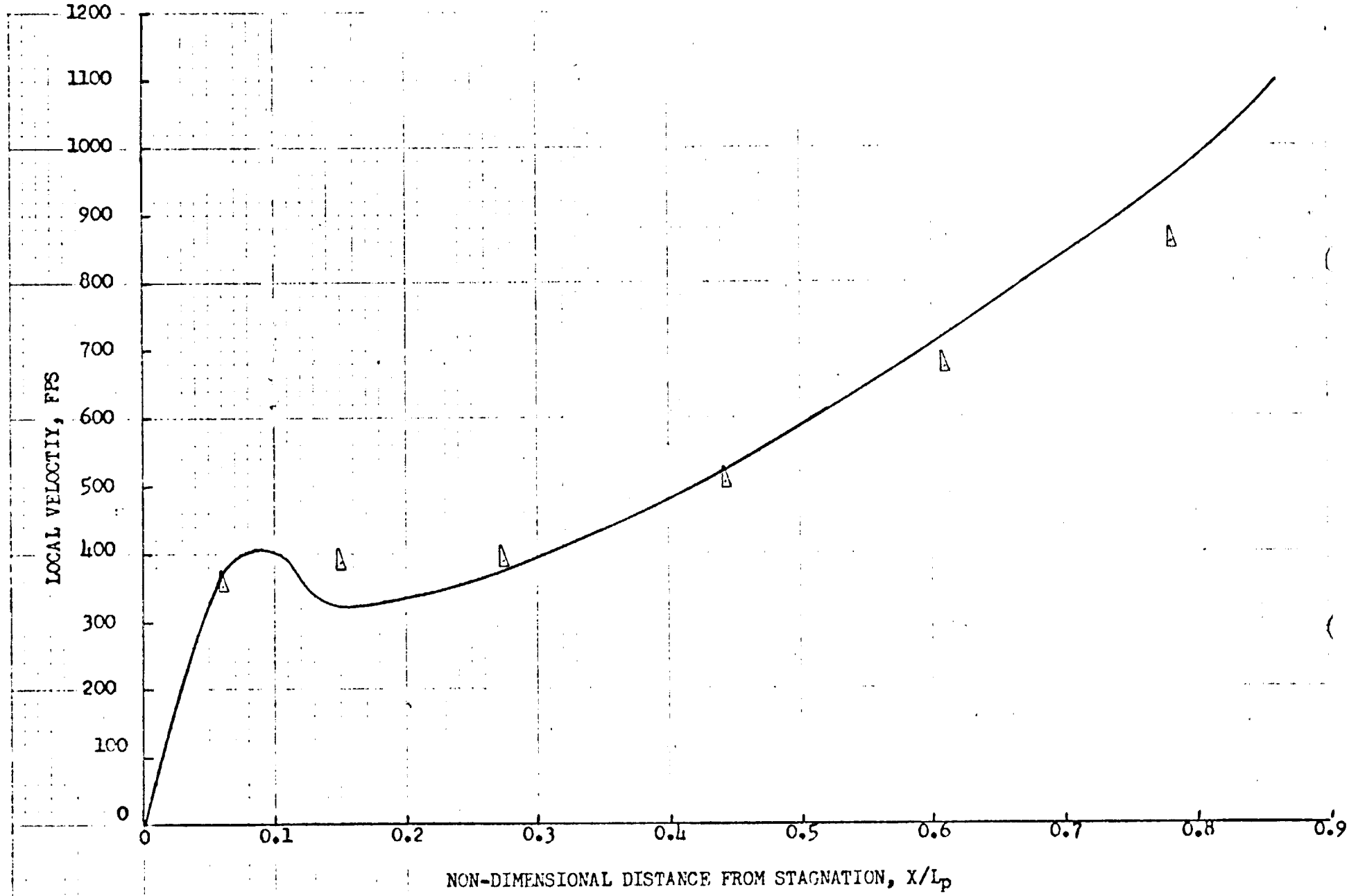
1200
1100
1000
900
800
700
600
500
400
300
200
100
0
LOCAL VELOCTIY, FPS
0
0.1
0.2
0.3
0.4
0.5
0.6
0.7
0.8
0.9
NON-DIMENSIONAL DISTANCE FROM STAGNATION, X/Lp

FIGURE 27.

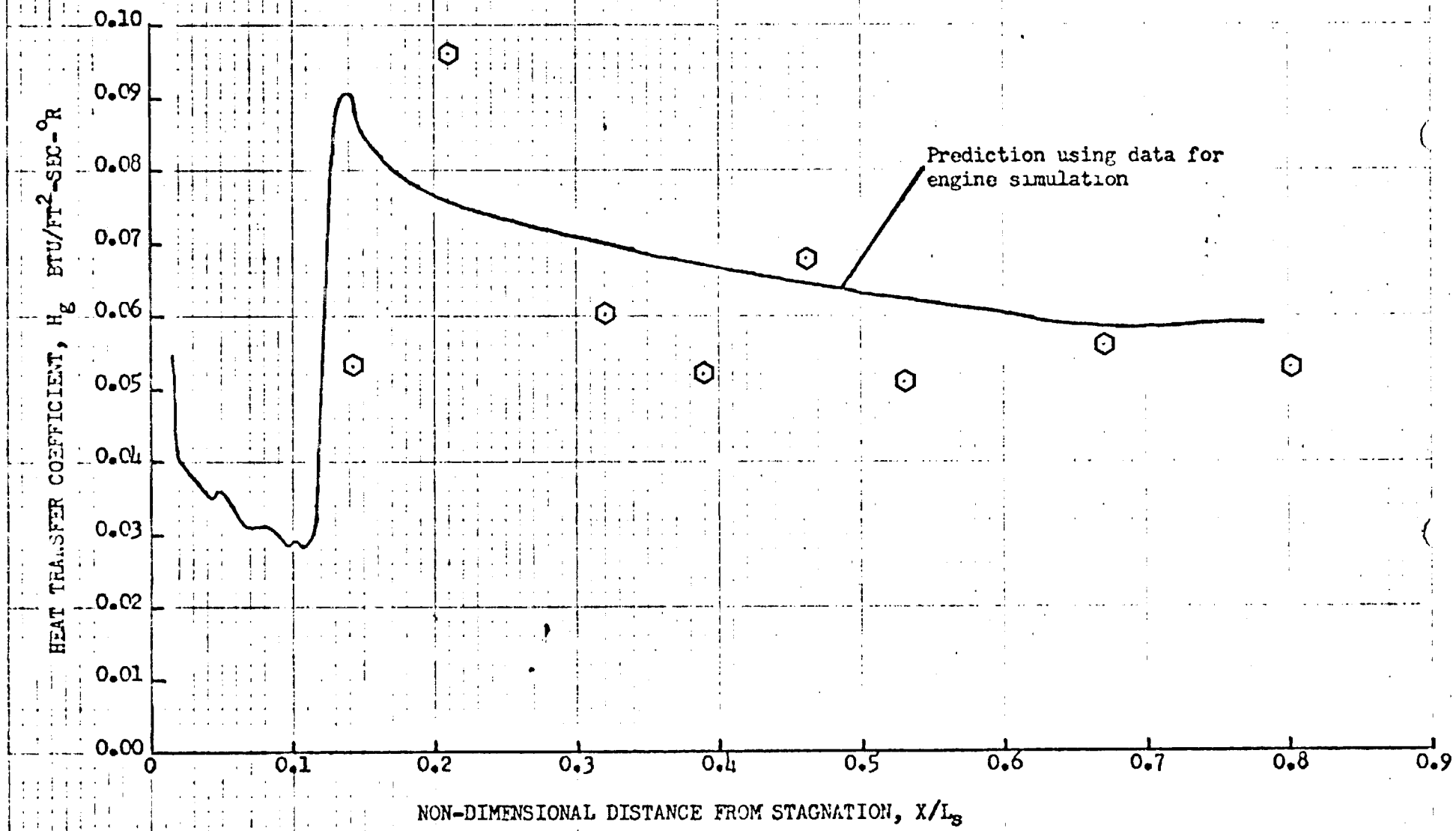
HEAT TRANSFER COEFFICIENT, H_g BTU/FT^2-SEC-^{o}R
0.10
0.09
0.08
0.07
0.06
0.05
0.04
0.03
0.02
0.01
0.00
0
0.1
0.2
0.3
0.4
0.5
0.6
0.7
0.8
0.9
NON-DIMENSIONAL DISTANCE FROM STAGNATION, X/L_s
Prediction using data for engine simulation

FIGURE 28.

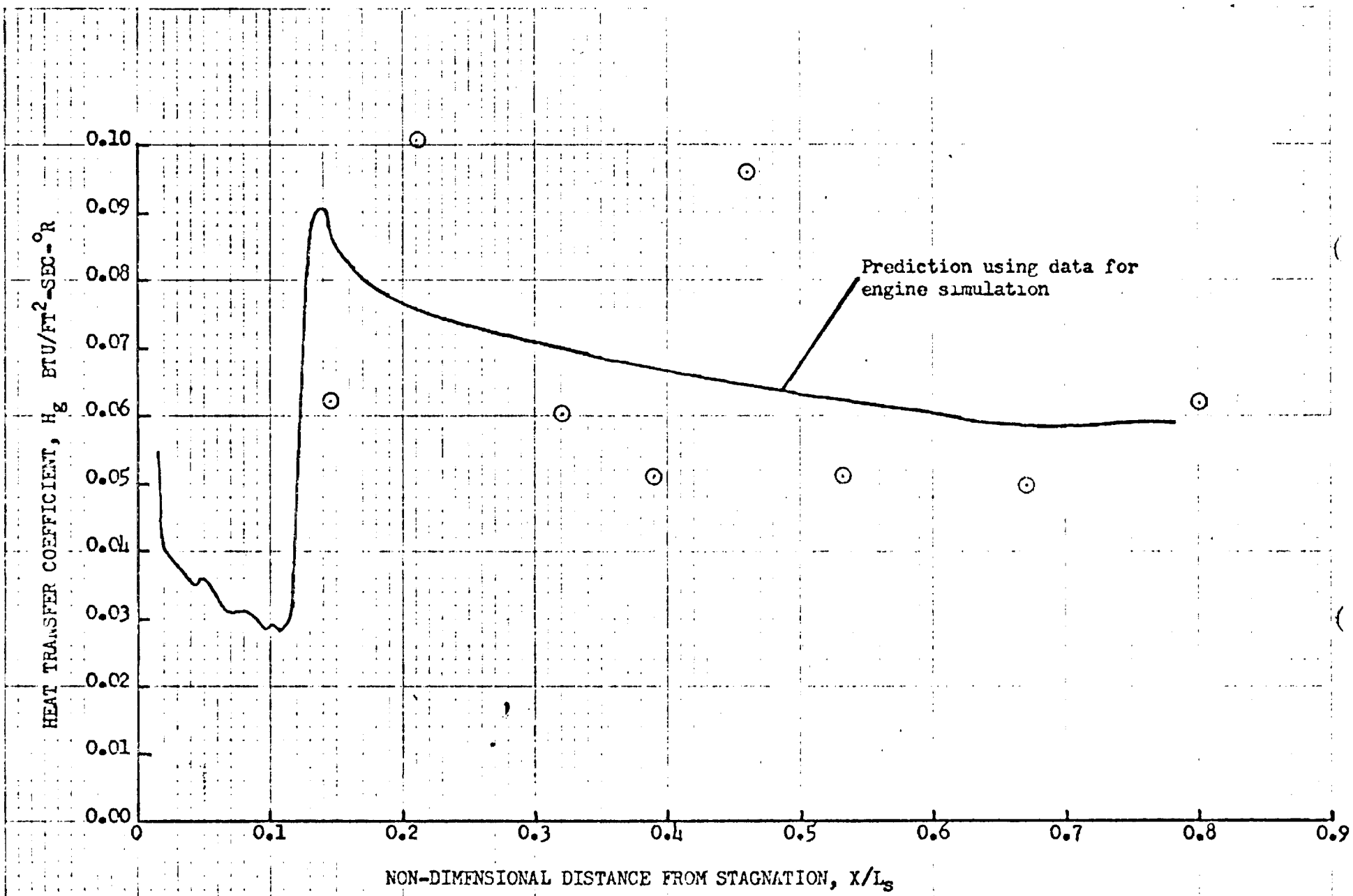
0.10
0.09
0.08
0.07
0.06
0.05
0.04
0.03
0.02
0.01
0.00
HEAT TRANSFER COEFFICIENT, H_g BTU/FT^2-SEC-$^\circ$R
0
0.1
0.2
0.3
0.4
0.5
0.6
0.7
0.8
0.9
NON-DIMENSIONAL DISTANCE FROM STAGNATION, X/L_s
Prediction using data for engine simulation

FIGURE 29.

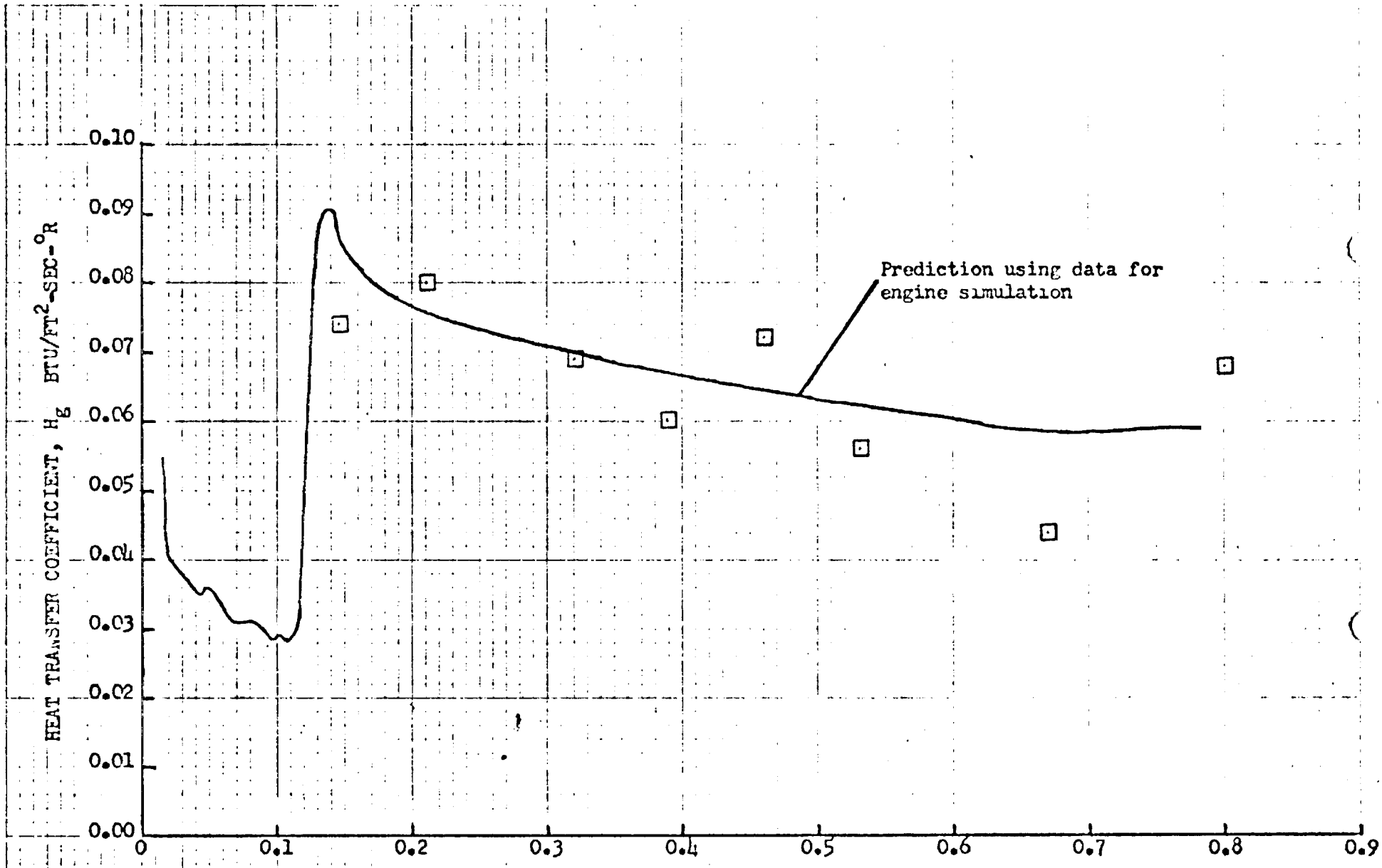
HEAT TRANSFER COEFFICIENT, H_g BTU/FT^2-SEC-^{o}R
0.10
0.09
0.08
0.07
0.06
0.05
0.04
0.03
0.02
0.01
0.00
0
0.1
0.2
0.3
0.4
0.5
0.6
0.7
0.8
0.9
NON-DIMENSIONAL DISTANCE FROM STAGNATION, X/L_s
Prediction using data for engine simulation

FIGURE 30.

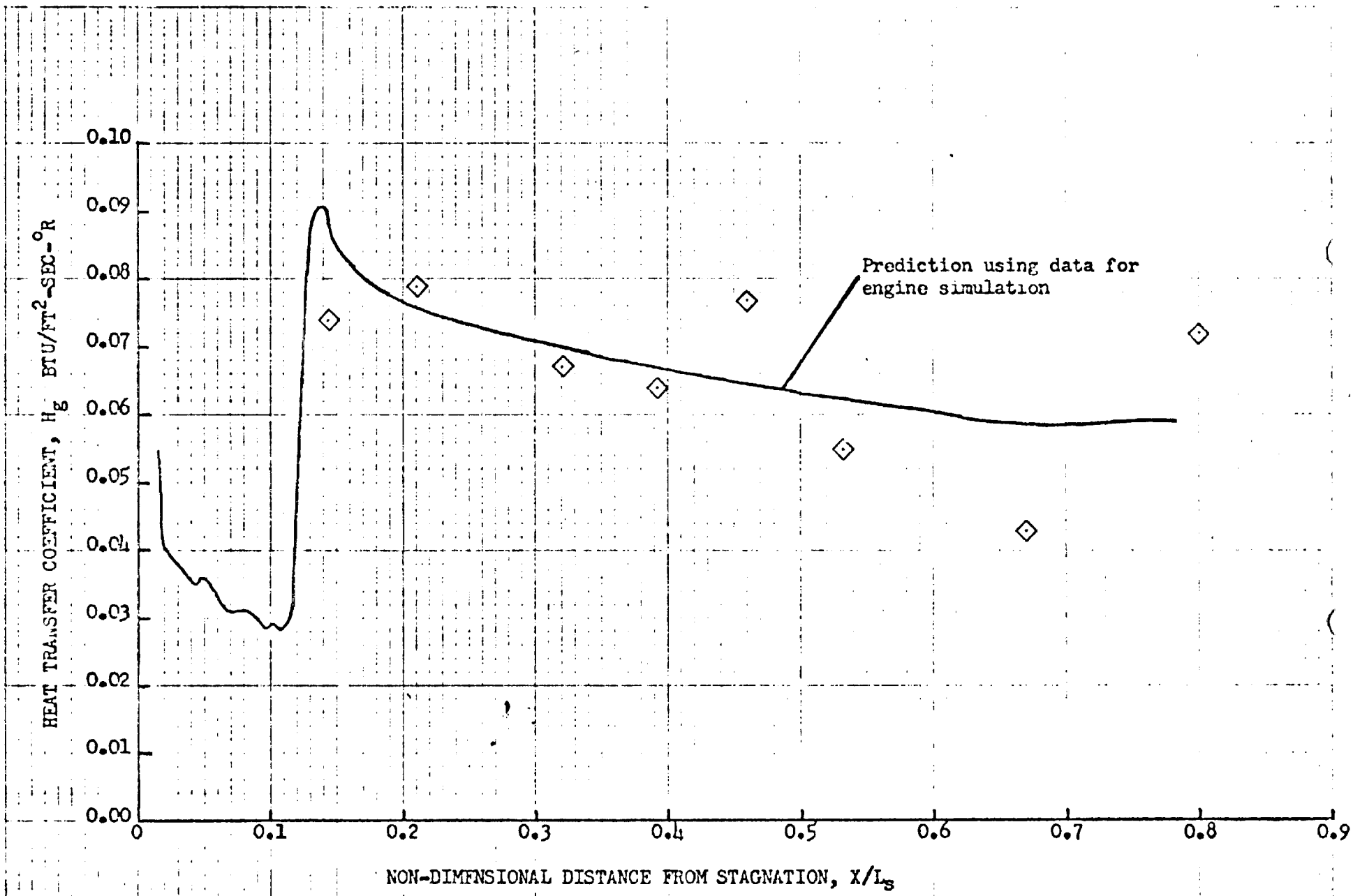
HEAT TRANSFER COEFFICIENT, H_g BTU/FT^2-SEC-$^\circ$R
0.10
0.09
0.08
0.07
0.06
0.05
0.04
0.03
0.02
0.01
0.00
0
0.1
0.2
0.3
0.4
0.5
0.6
0.7
0.8
0.9
NON-DIMENSIONAL DISTANCE FROM STAGNATION, X/L_s
Prediction using data for engine simulation

FIGURE 31.

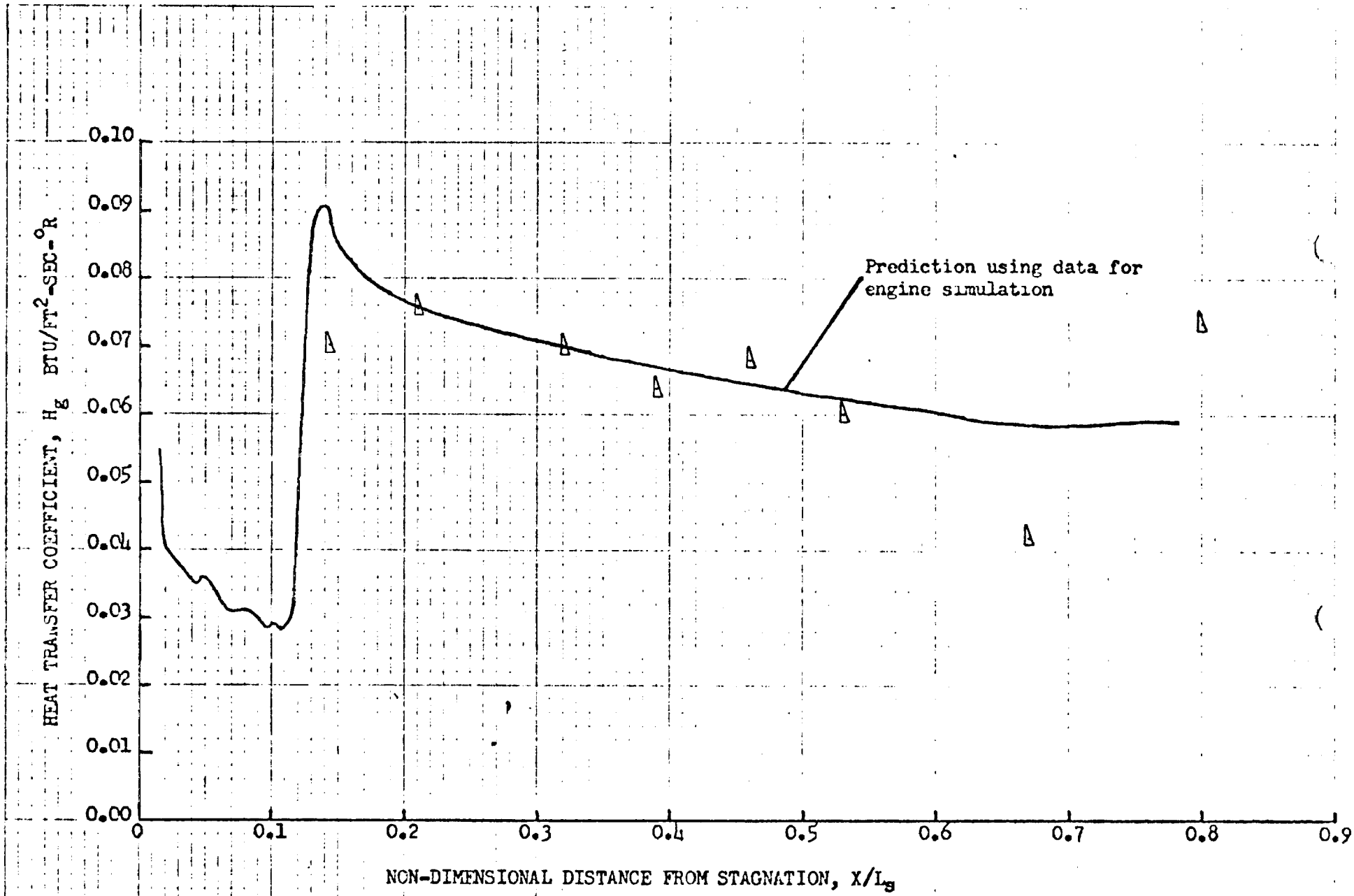
0.10
0.09
0.08
0.07
0.06
0.05
0.04
0.03
0.02
0.01
0.00
HEAT TRANSFER COEFFICIENT, H_g BTU/FT^2-SEC-^{o}R
0
0.1
0.2
0.3
0.4
0.5
0.6
0.7
0.8
0.9
NON-DIMENSIONAL DISTANCE FROM STAGNATION, X/L_s
Prediction using data for engine simulation

FIGURE 32.

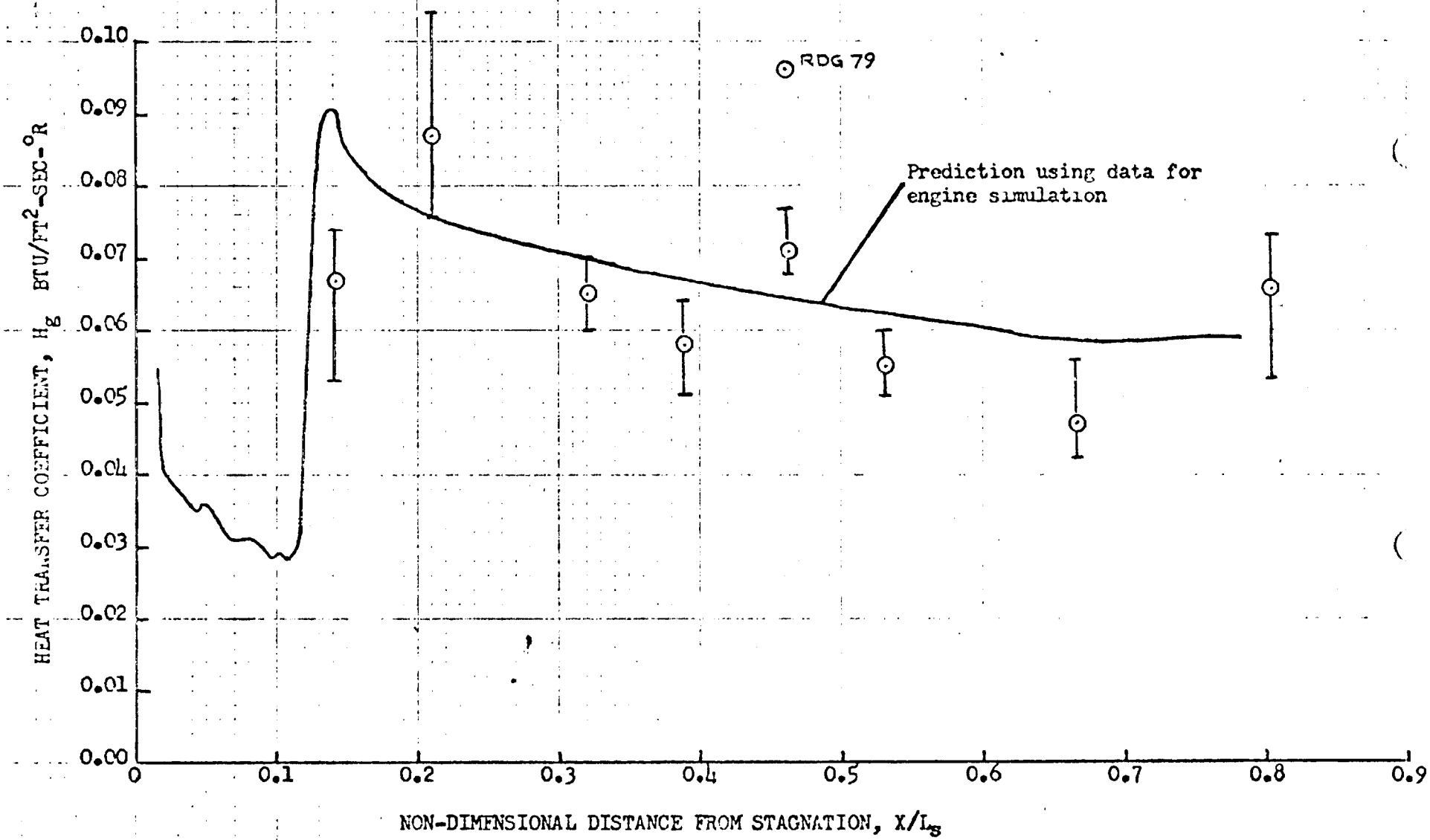
RDG 79
Prediction using data for engine simulation
HEAT TRANSFER COEFFICIENT, H_g BTU/FT^2-SEC-^{o}R
0.10
0.09
0.08
0.07
0.06
0.05
0.04
0.03
0.02
0.01
0.00
0
0.1
0.2
0.3
0.4
0.5
0.6
0.7
0.8
0.9
NON-DIMENSIONAL DISTANCE FROM STAGNATION, X/L_s

FIGURE 33.

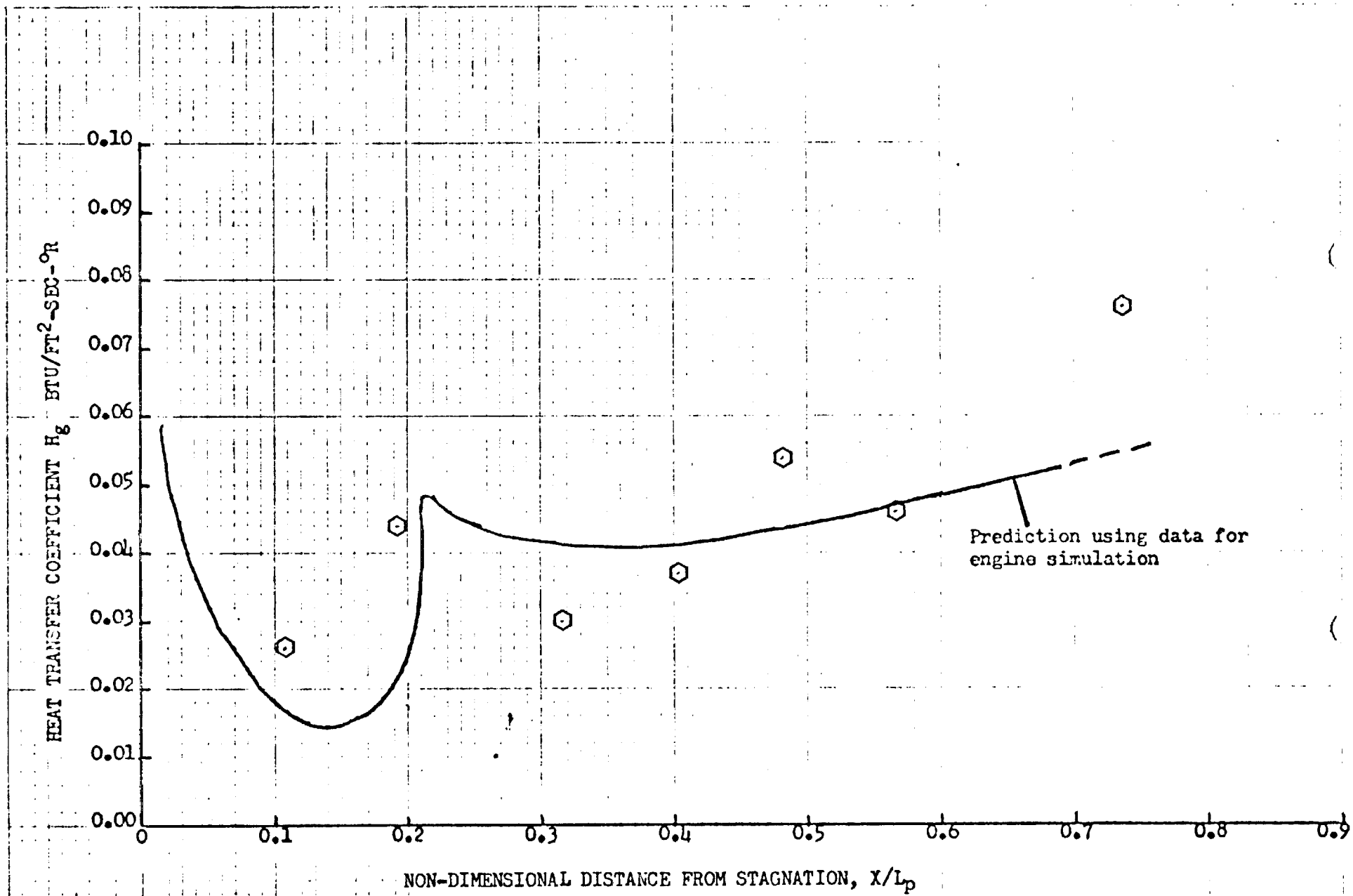
HEAT TRANSFER COEFFICIENT H_g BTU/FT^2-SEC-^{o}R
0.10
0.09
0.08
0.07
0.06
0.05
0.04
0.03
0.02
0.01
0.00
0
0.1
0.2
0.3
0.4
0.5
0.6
0.7
0.8
0.9
NON-DIMENSIONAL DISTANCE FROM STAGNATION, X/L_p
Prediction using data for engine simulation

FIGURE 34.

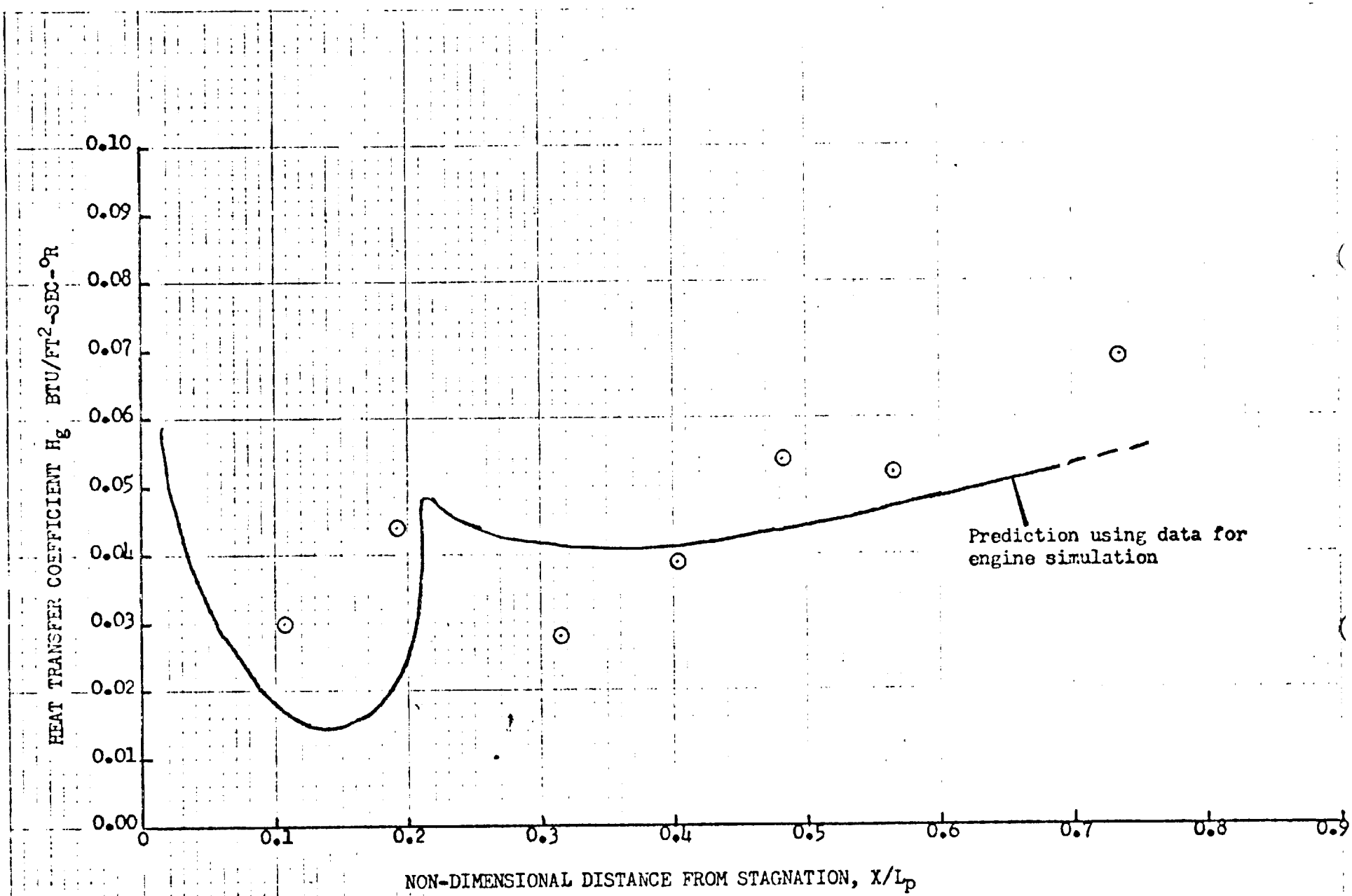
HEAT TRANSFER COEFFICIENT H_g BTU/FT^2-SEC-^{o}R
0.10
0.09
0.08
0.07
0.06
0.05
0.04
0.03
0.02
0.01
0.00
0
0.1
0.2
0.3
0.4
0.5
0.6
0.7
0.8
0.9
NON-DIMENSIONAL DISTANCE FROM STAGNATION, X/L_p
Prediction using data for engine simulation

FIGURE 35.

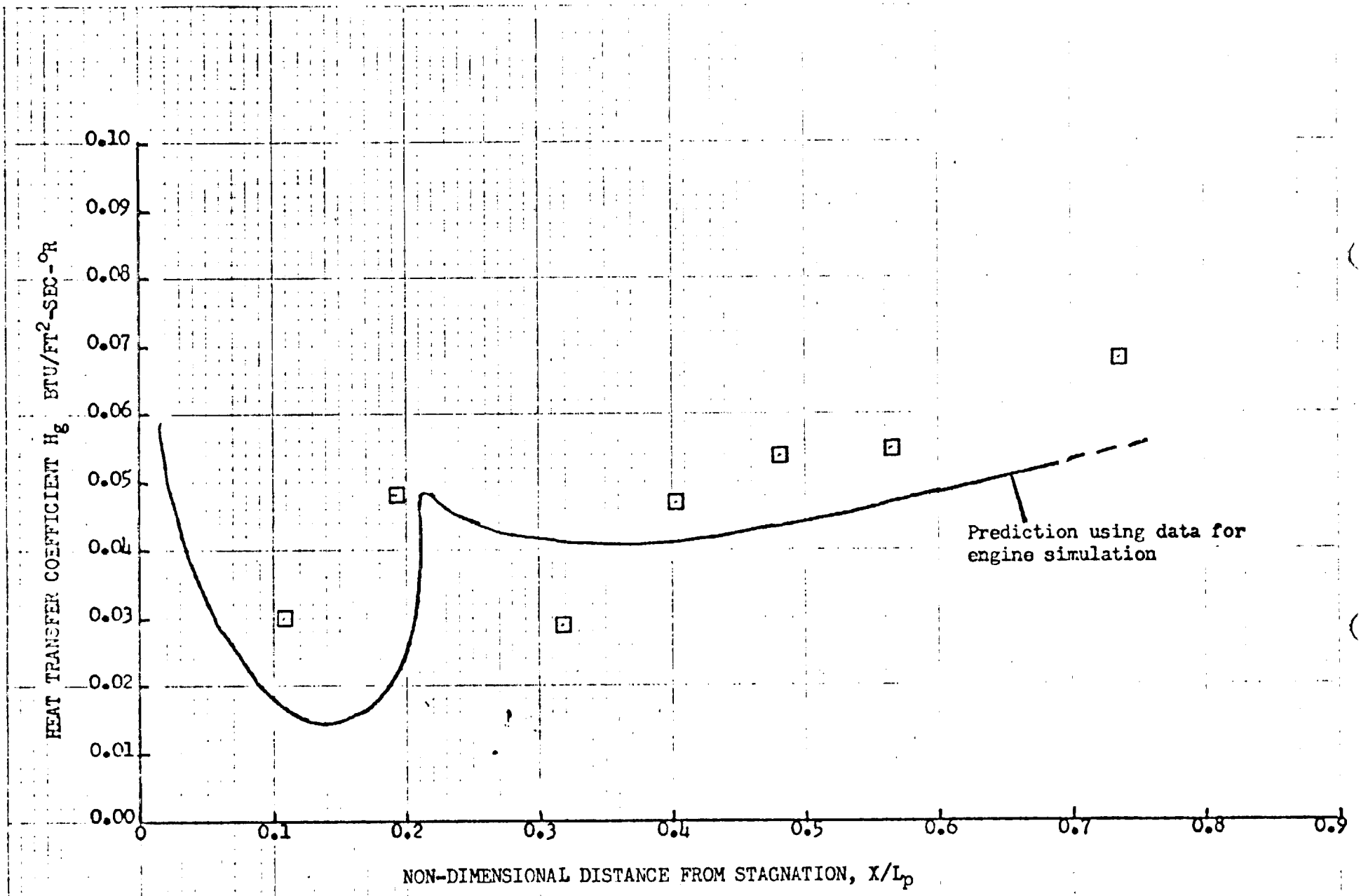
HEAT TRANSFER COEFFICIENT H_g BTU/FT^2-SEC-^{o}R
0.10
0.09
0.08
0.07
0.06
0.05
0.04
0.03
0.02
0.01
0.00
0
0.1
0.2
0.3
0.4
0.5
0.6
0.7
0.8
0.9
NON-DIMENSIONAL DISTANCE FROM STAGNATION, X/L_p
Prediction using data for engine simulation

FIGURE 34.

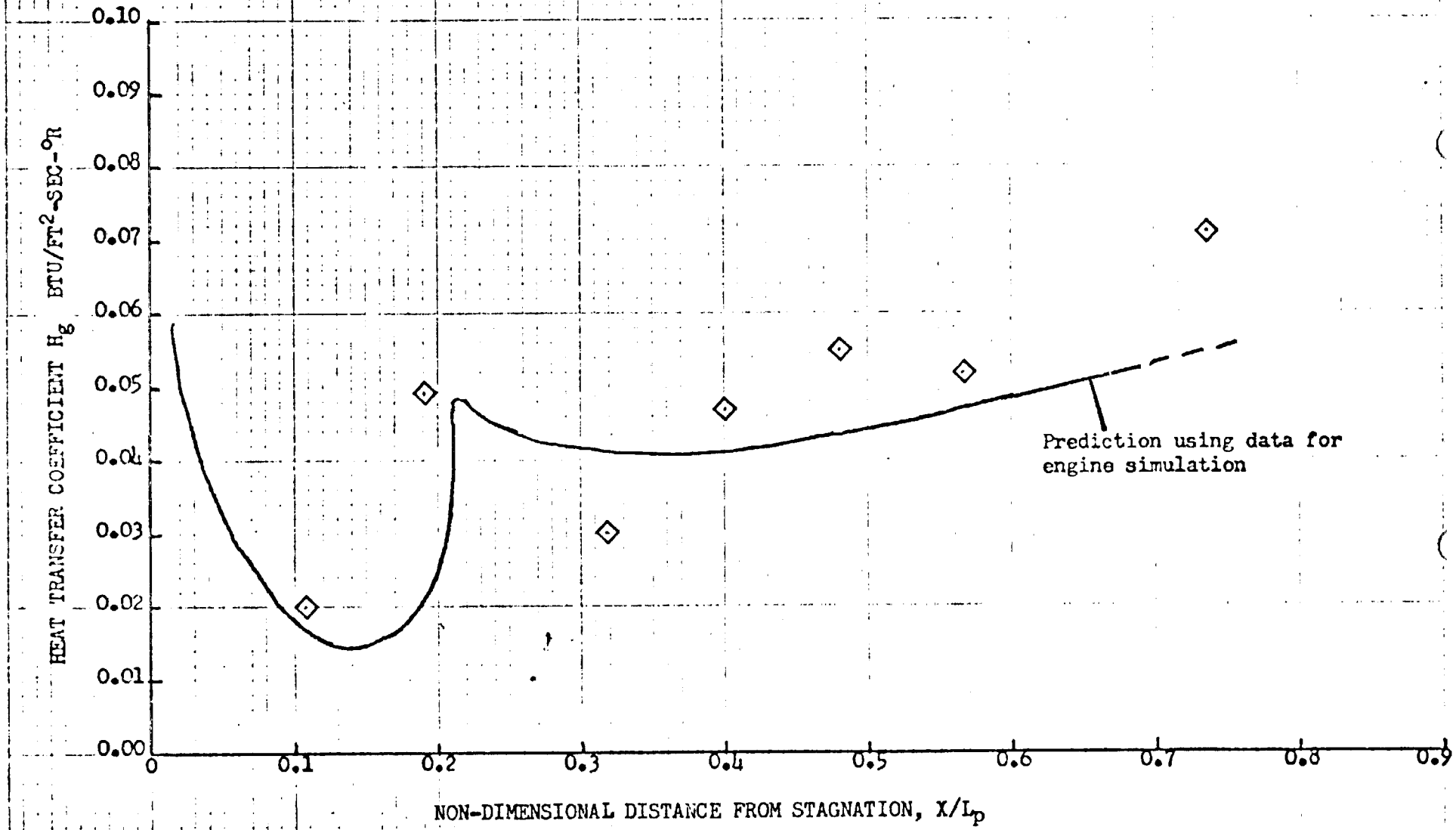
HEAT TRANSFER COEFFICIENT H_g BTU/FT^2-SEC-^{o}R
0.10
0.09
0.08
0.07
0.06
0.05
0.04
0.03
0.02
0.01
0.00
0
0.1
0.2
0.3
0.4
0.5
0.6
0.7
0.8
0.9
NON-DIMENSIONAL DISTANCE FROM STAGNATION, X/L_p
Prediction using data for engine simulation

FIGURE 37.

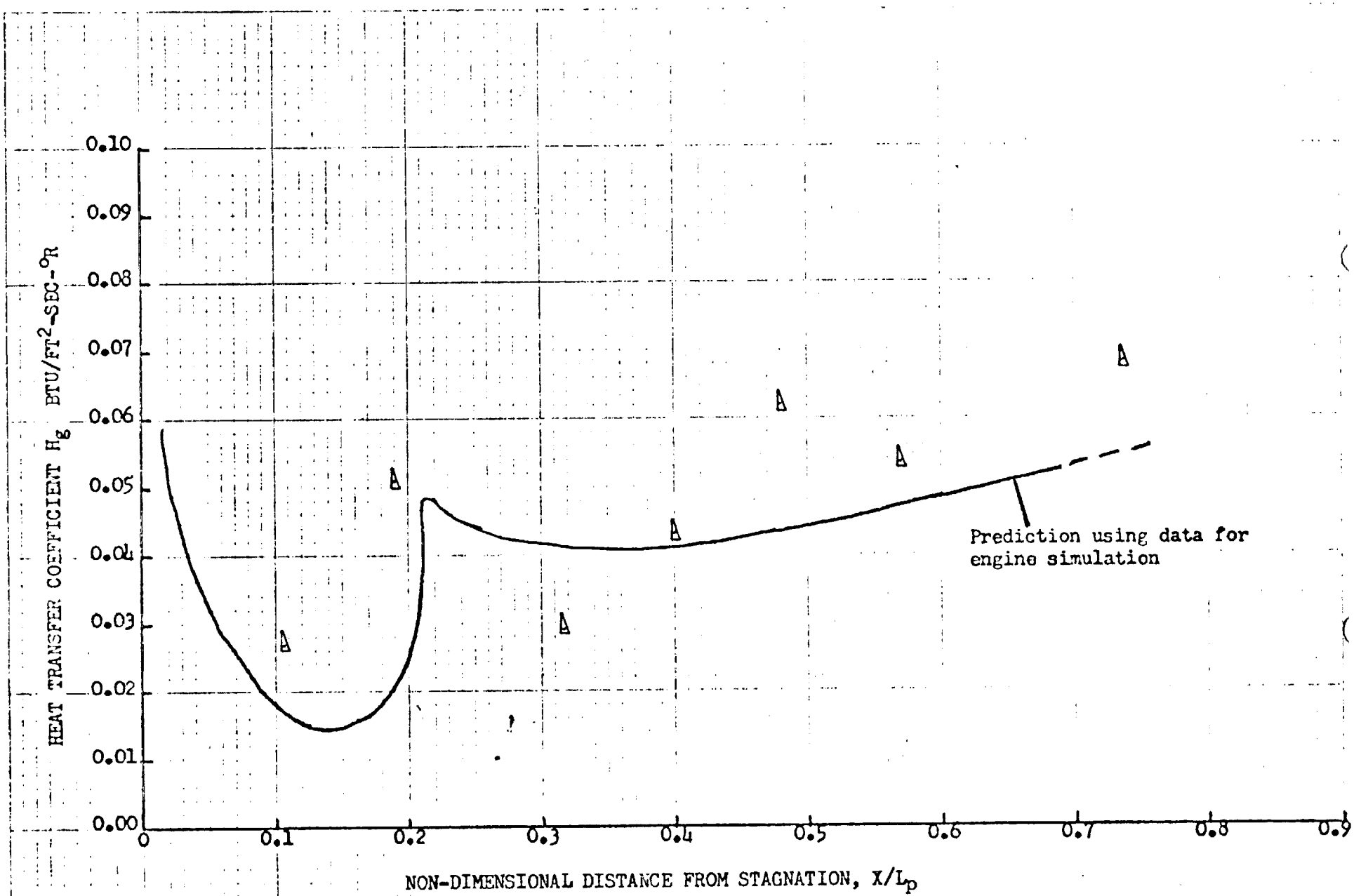
HEAT TRANSFER COEFFICIENT H_g BTU/FT^2-SEC-^{o}R
0.10
0.09
0.08
0.07
0.06
0.05
0.04
0.03
0.02
0.01
0.00
0
0.1
0.2
0.3
0.4
0.5
0.6
0.7
0.8
0.9
NON-DIMENSIONAL DISTANCE FROM STAGNATION, X/L_p
Prediction using data for engine simulation

FIGURE 38.

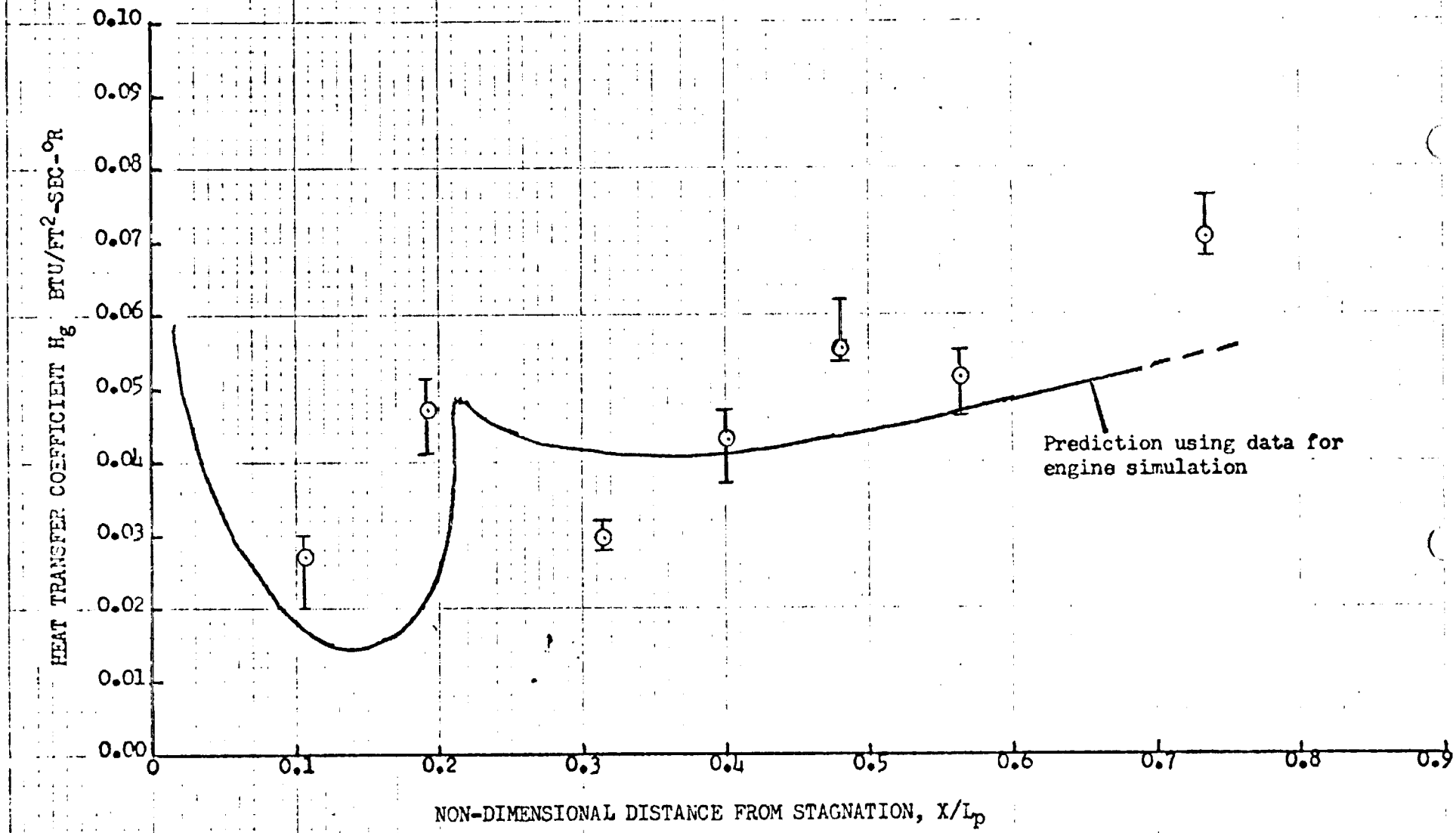
HEAT TRANSFER COEFFICIENT H_g BTU/FT^2-SEC-^{o}R
0.10
0.09
0.08
0.07
0.06
0.05
0.04
0.03
0.02
0.01
0.00
0
0.1
0.2
0.3
0.4
0.5
0.6
0.7
0.8
0.9
NON-DIMENSIONAL DISTANCE FROM STAGNATION, X/L_p
Prediction using data for engine simulation

FIGURE 39.

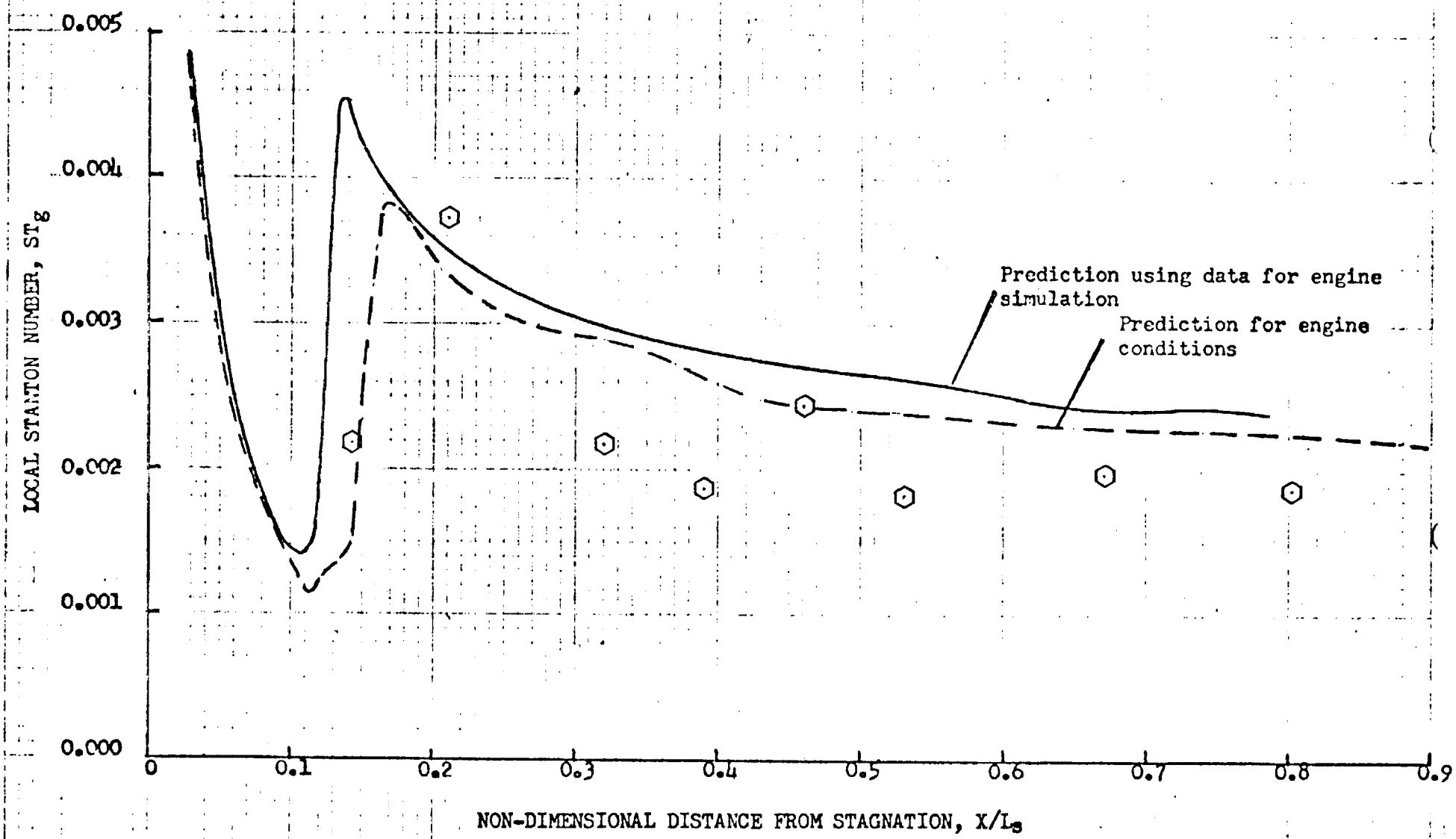
0.005
0.004
0.003
0.002
0.001
0.000
LOCAL STANTON NUMBER, ST_g
0
0.1
0.2
0.3
0.4
0.5
0.6
0.7
0.8
0.9
NON-DIMENSIONAL DISTANCE FROM STAGNATION, X/L_s
Prediction using data for engine simulation
Prediction for engine conditions

FIGURE 40.

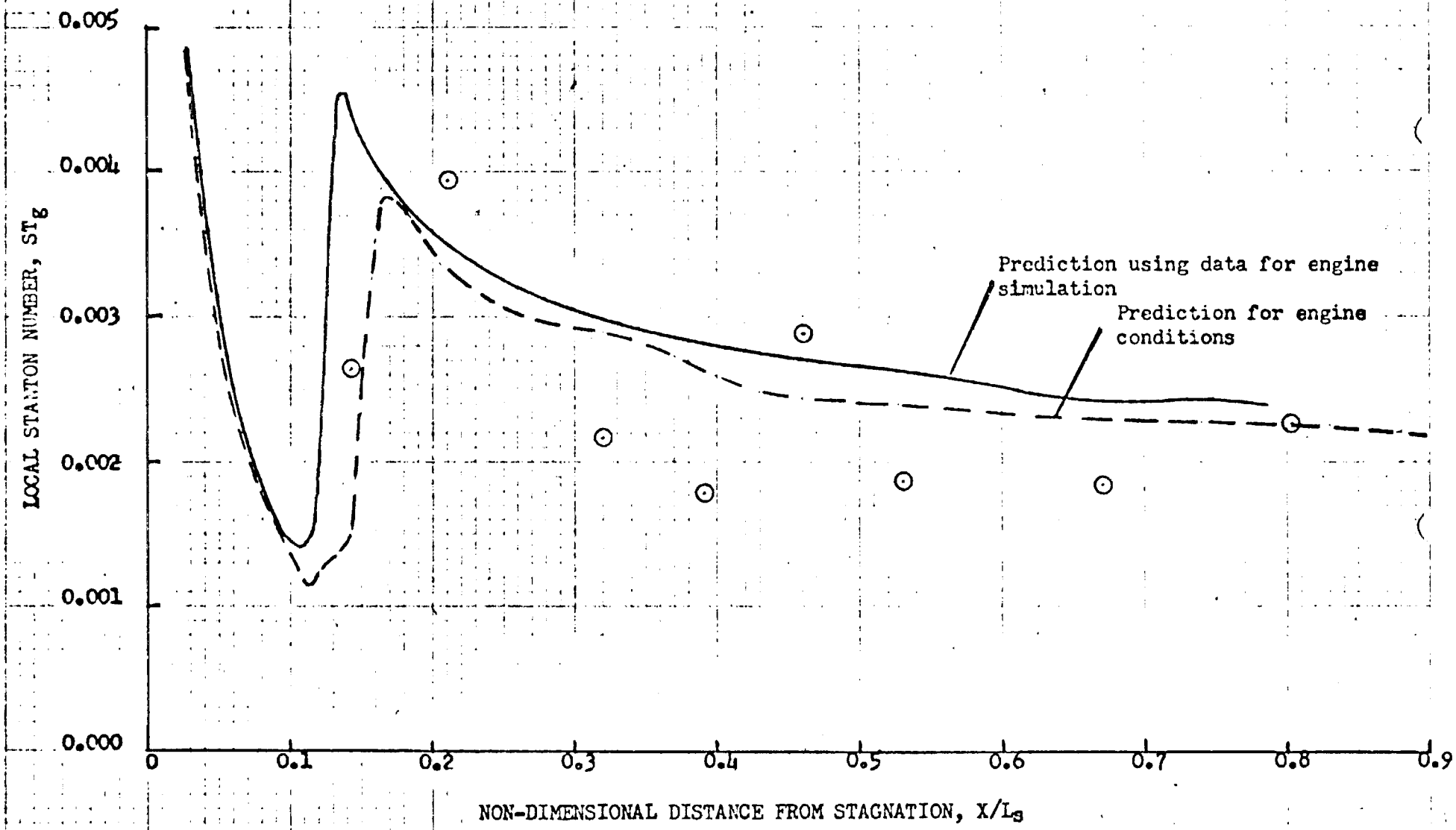
0.005
0.004
0.003
0.002
0.001
0.000
LOCAL STANTON NUMBER, ST_g
0
0.1
0.2
0.3
0.4
0.5
0.6
0.7
0.8
0.9
NON-DIMENSIONAL DISTANCE FROM STAGNATION, X/L_s
Prediction using data for engine simulation
Prediction for engine conditions

FIGURE 41.

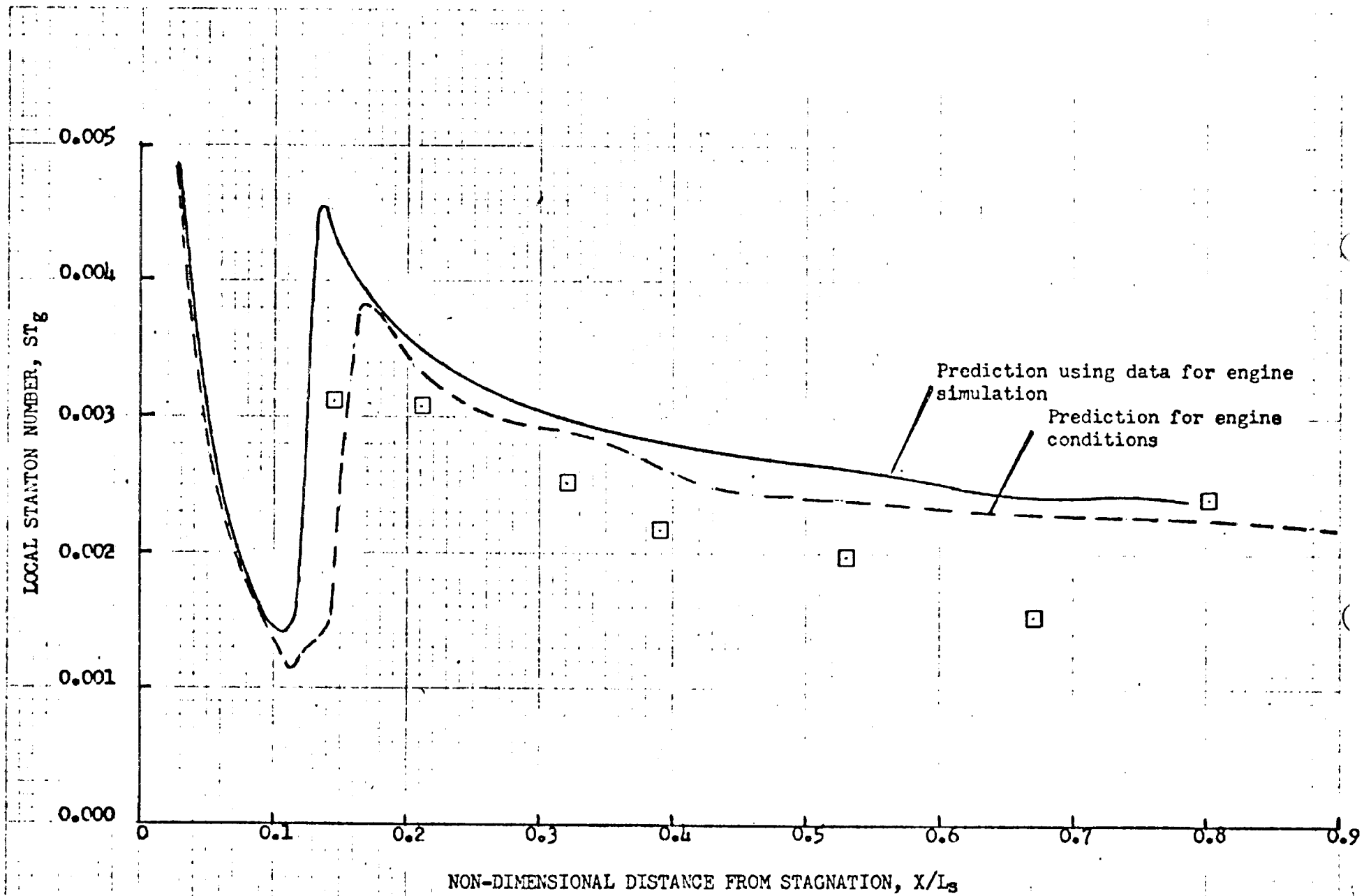
0.005
0.004
0.003
0.002
0.001
0.000
LOCAL STANTON NUMBER, ST_g
0
0.1
0.2
0.3
0.4
0.5
0.6
0.7
0.8
0.9
NON-DIMENSIONAL DISTANCE FROM STAGNATION, X/L_s
Prediction using data for engine simulation
Prediction for engine conditions

FIGURE 42.

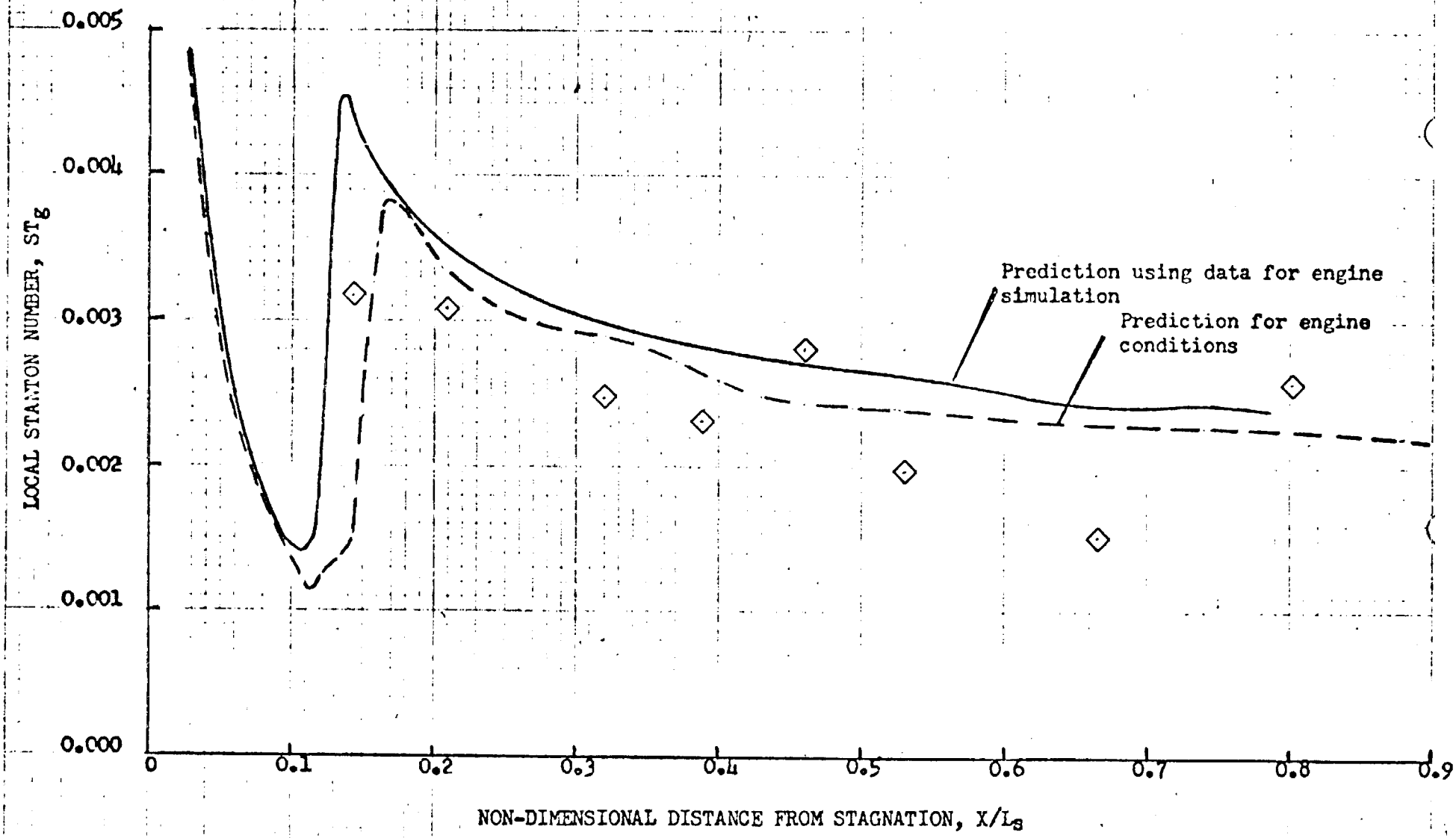
0.005
0.004
0.003
0.002
0.001
0.000
LOCAL STANTON NUMBER, ST_g
0
0.1
0.2
0.3
0.4
0.5
0.6
0.7
0.8
0.9
NON-DIMENSIONAL DISTANCE FROM STAGNATION, X/L_s
Prediction using data for engine simulation
Prediction for engine conditions

FIGURE 43.

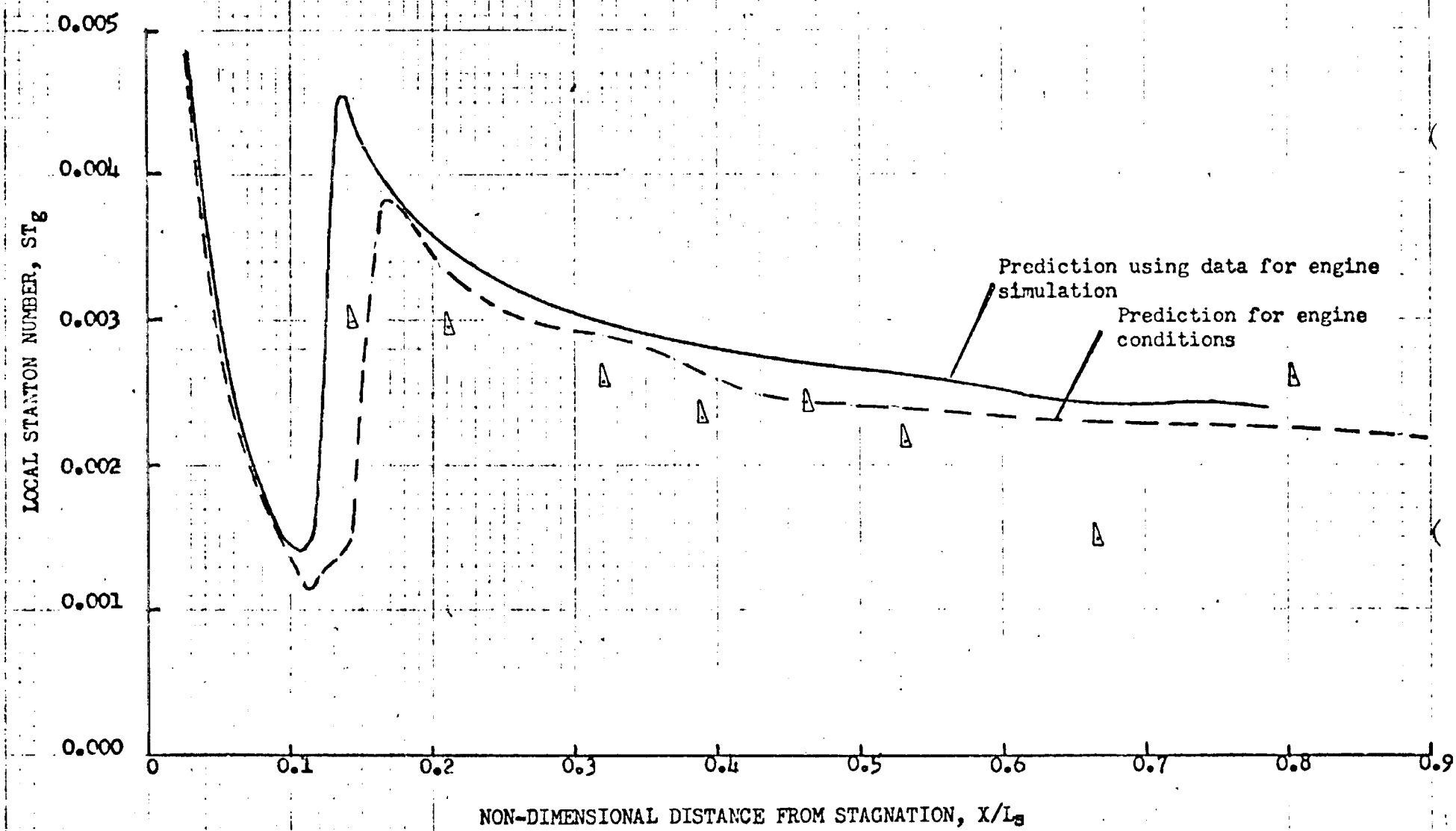
0.005
0.004
0.003
0.002
0.001
0.000
LOCAL STANTON NUMBER, ST_g
0
0.1
0.2
0.3
0.4
0.5
0.6
0.7
0.8
0.9
NON-DIMENSIONAL DISTANCE FROM STAGNATION, X/L_s
Prediction using data for engine simulation
Prediction for engine conditions

FIGURE 44.

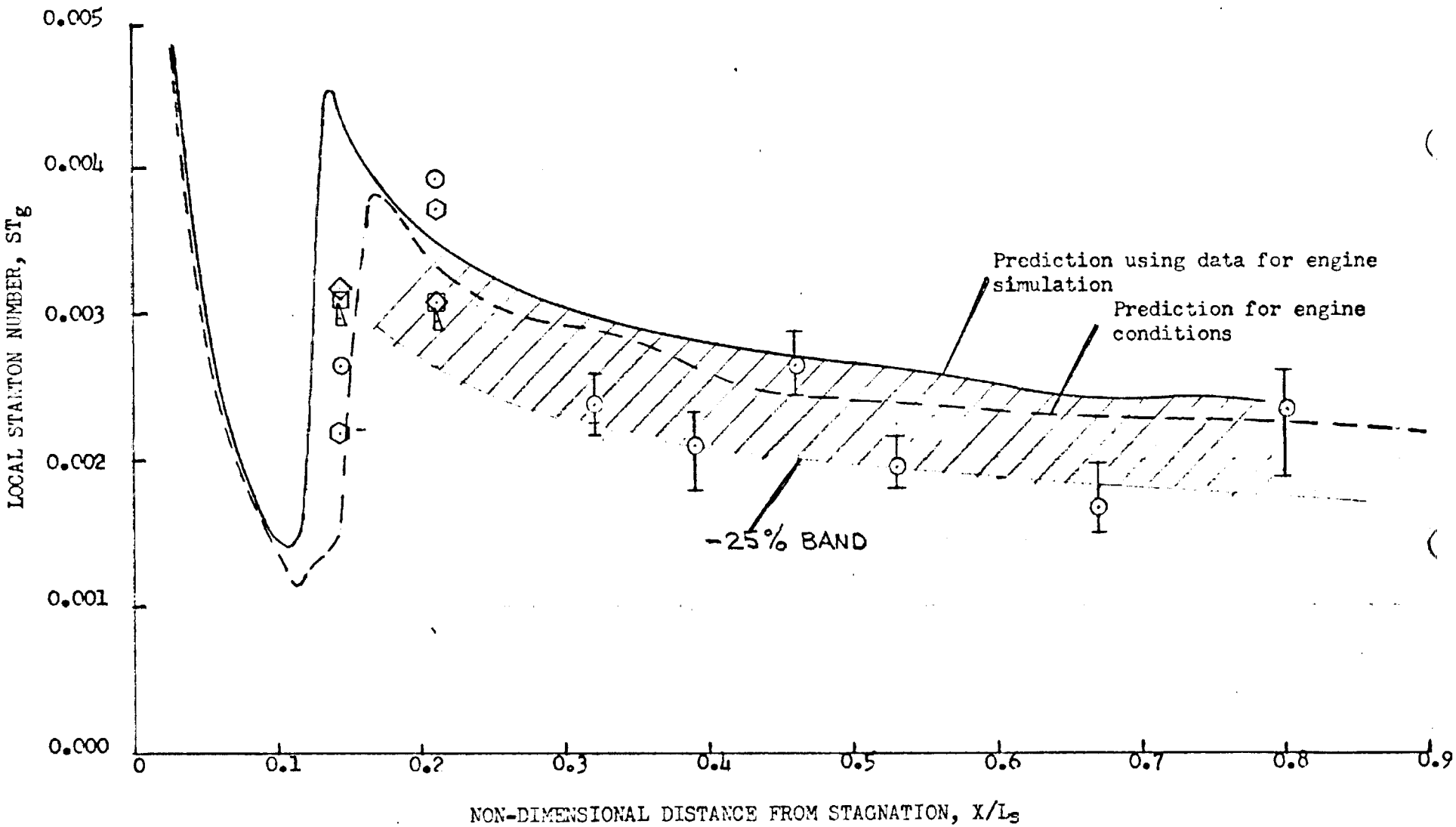
0.005
0.004
0.003
0.002
0.001
0.000
LOCAL STANTON NUMBER, ST_g
0
0.1
0.2
0.3
0.4
0.5
0.6
0.7
0.8
0.9
NON-DIMENSIONAL DISTANCE FROM STAGNATION, X/L_s
Prediction using data for engine simulation
Prediction for engine conditions
-25% BAND

FIGURE 45.

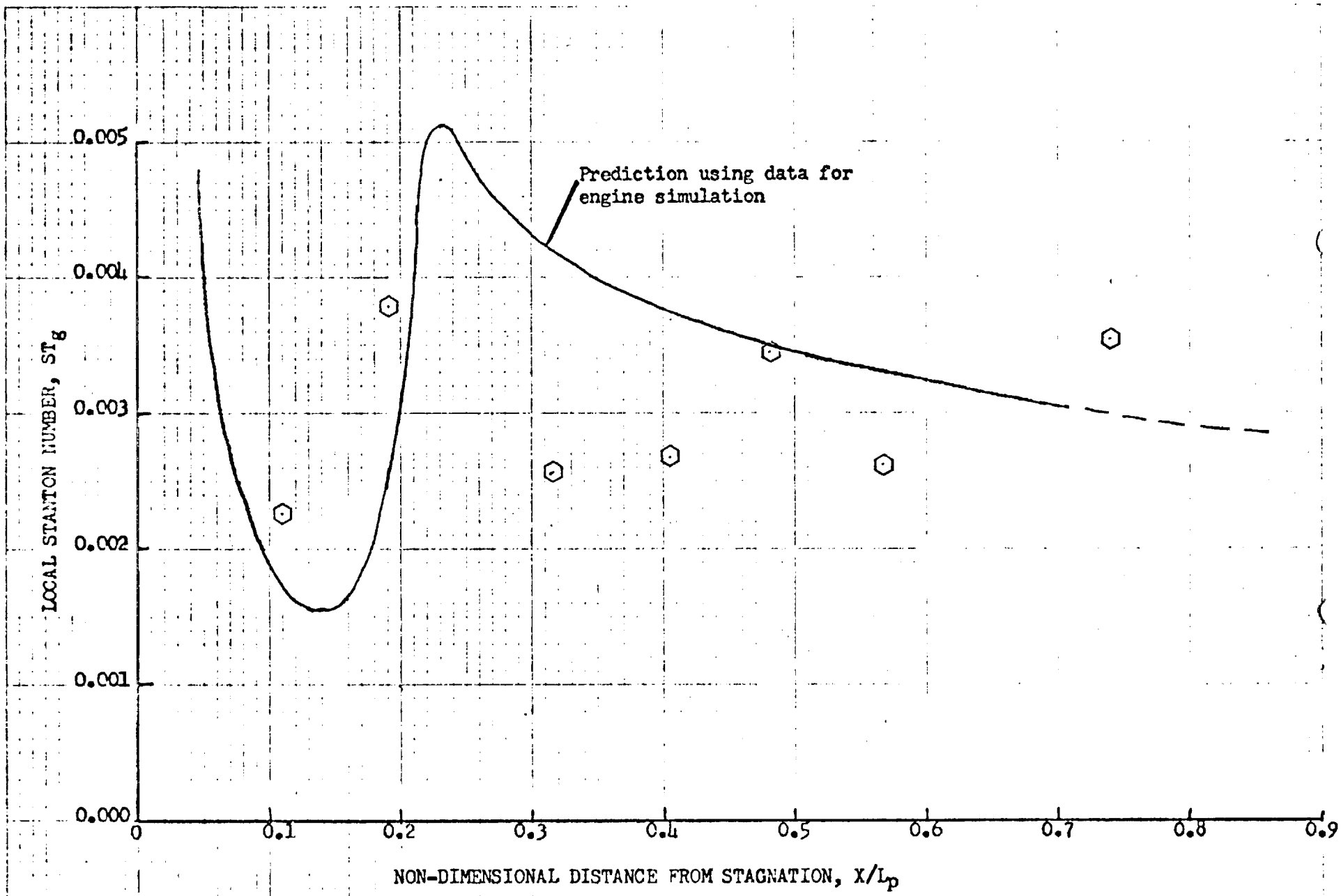
Prediction using data for engine simulation
LOCAL STANTON NUMBER, ST_g
0.005
0.004
0.003
0.002
0.001
0.000
0
0.1
0.2
0.3
0.4
0.5
0.6
0.7
0.8
0.9
NON-DIMENSIONAL DISTANCE FROM STAGNATION, X/L_p

FIGURE 46.

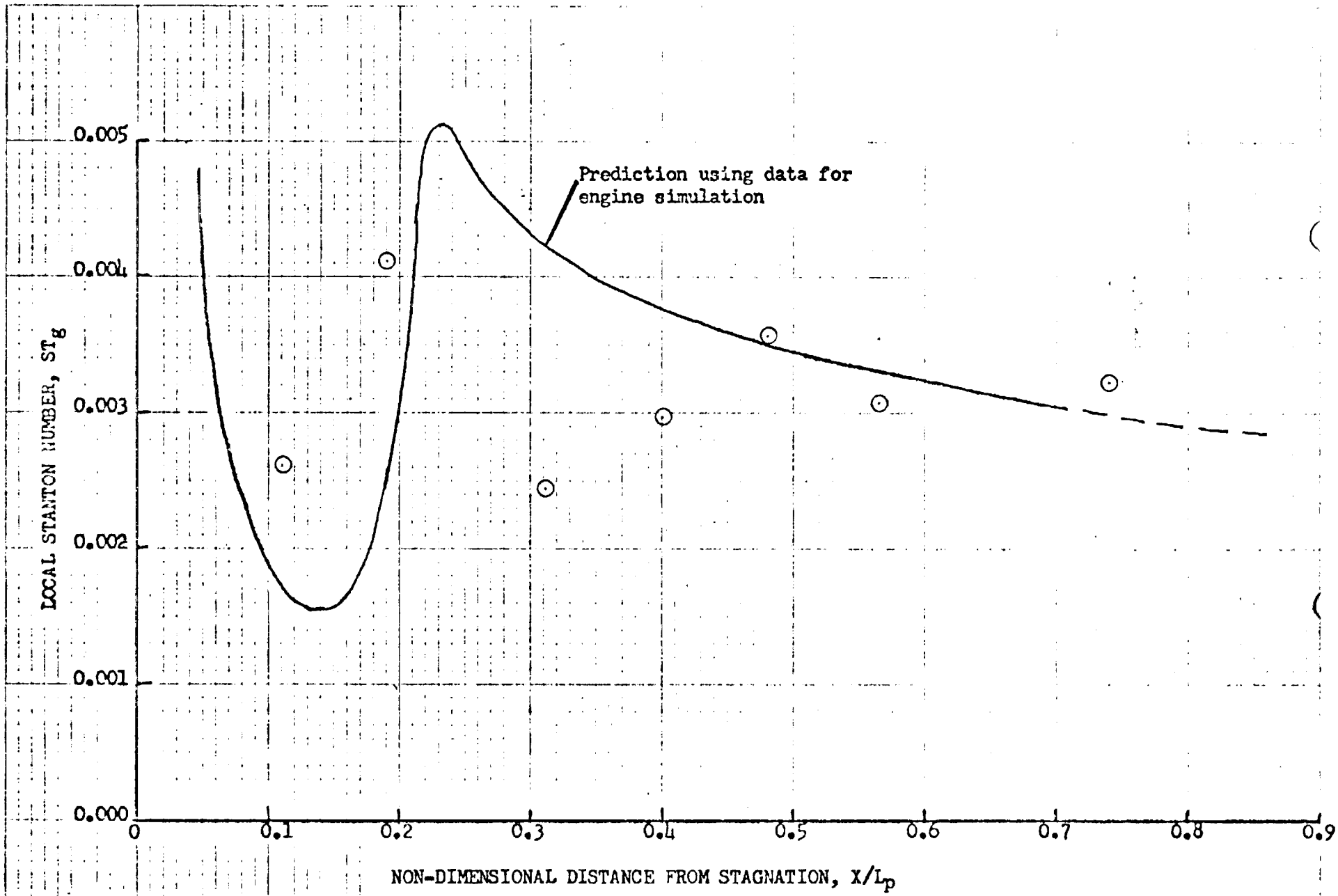
Prediction using data for engine simulation
LOCAL STANTON NUMBER, ST_g
0.005
0.004
0.003
0.002
0.001
0.000
0
0.1
0.2
0.3
0.4
0.5
0.6
0.7
0.8
0.9
NON-DIMENSIONAL DISTANCE FROM STAGNATION, X/L_p

FIGURE 47

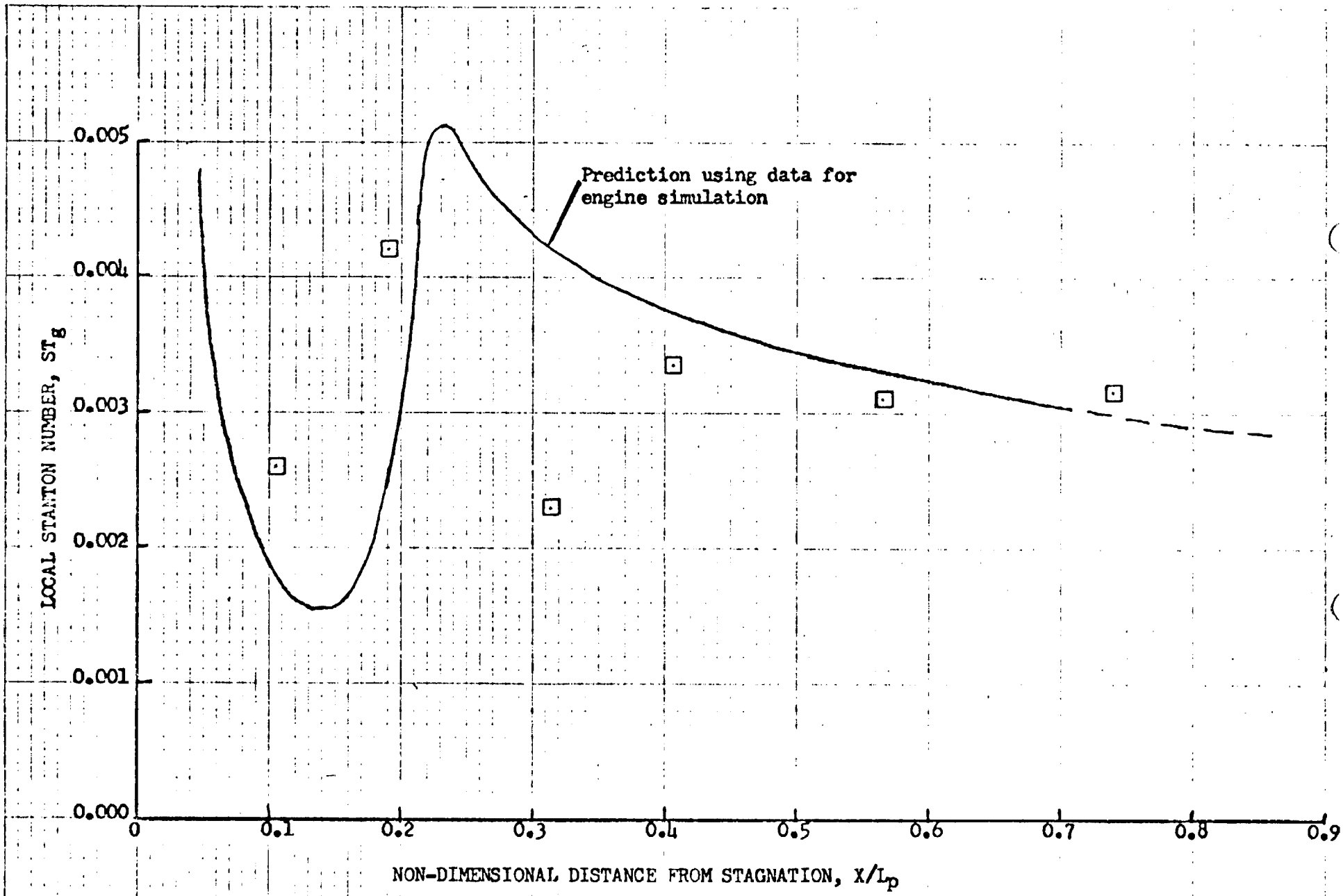
Prediction using data for engine simulation
LOCAL STANTON NUMBER, ST_g
0.005
0.004
0.003
0.002
0.001
0.000
0
0.1
0.2
0.3
0.4
0.5
0.6
0.7
0.8
0.9
NON-DIMENSIONAL DISTANCE FROM STAGNATION, X/L_p

FIGURE 48.

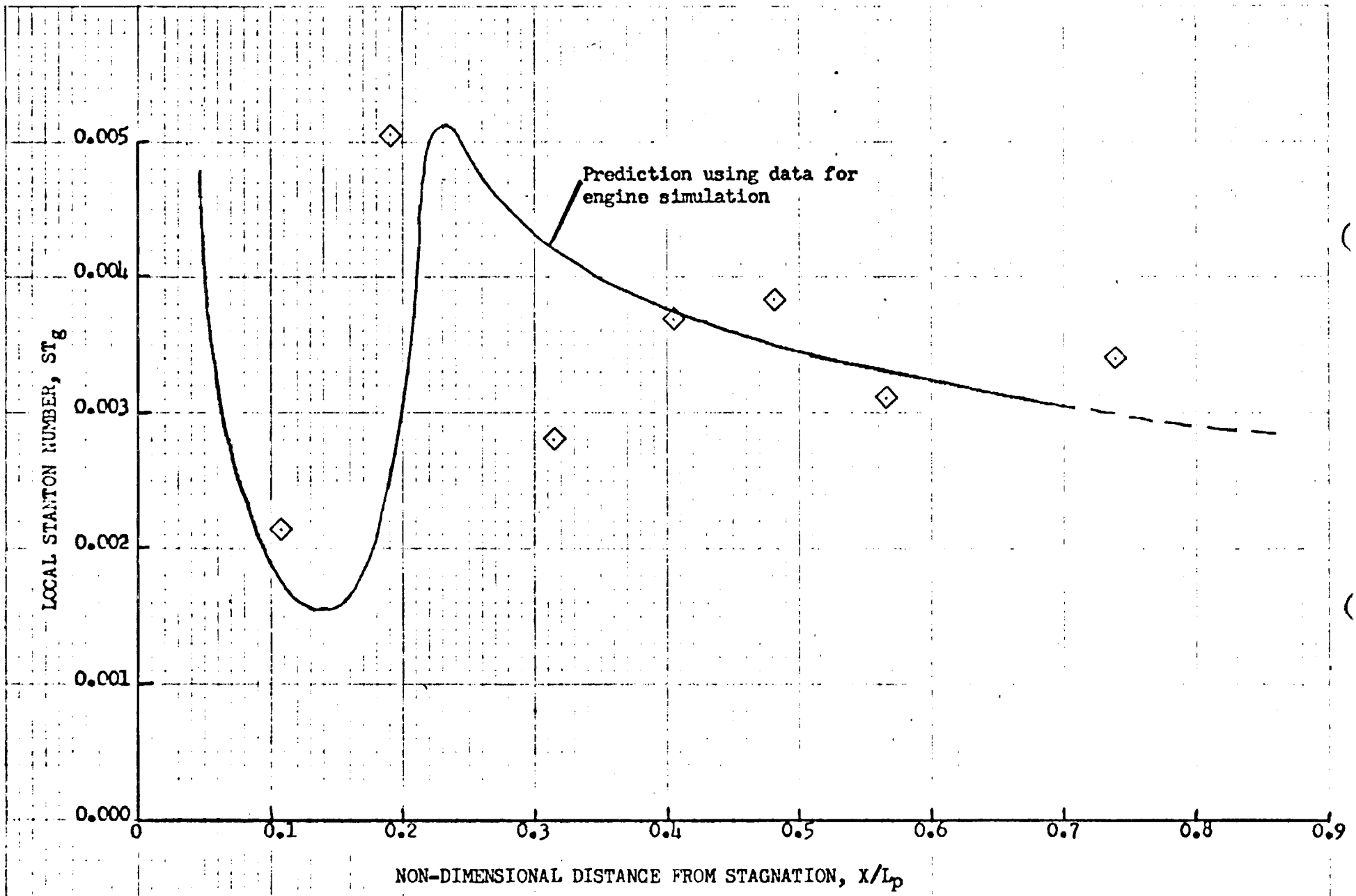
Prediction using data for engine simulation
LOCAL STANTON NUMBER, ST_g
0.005
0.004
0.003
0.002
0.001
0.000
0
0.1
0.2
0.3
0.4
0.5
0.6
0.7
0.8
0.9
NON-DIMENSIONAL DISTANCE FROM STAGNATION, X/L_p

FIGURE 49.

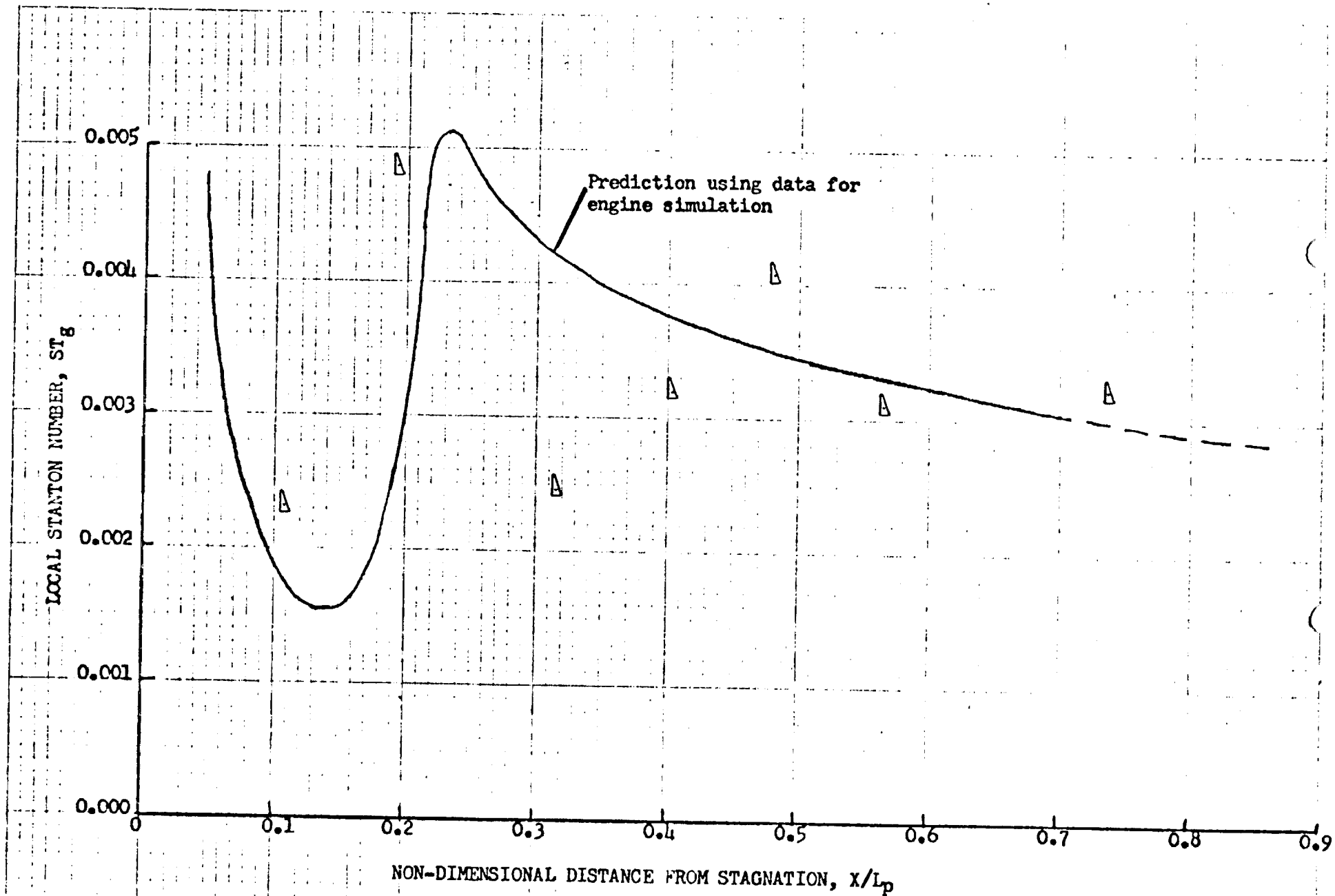
Prediction using data for engine simulation
LOCAL STANTON NUMBER, ST_g
0.005
0.004
0.003
0.002
0.001
0.000
0
0.1
0.2
0.3
0.4
0.5
0.6
0.7
0.8
0.9
NON-DIMENSIONAL DISTANCE FROM STAGNATION, X/L_p

FIGURE 50.

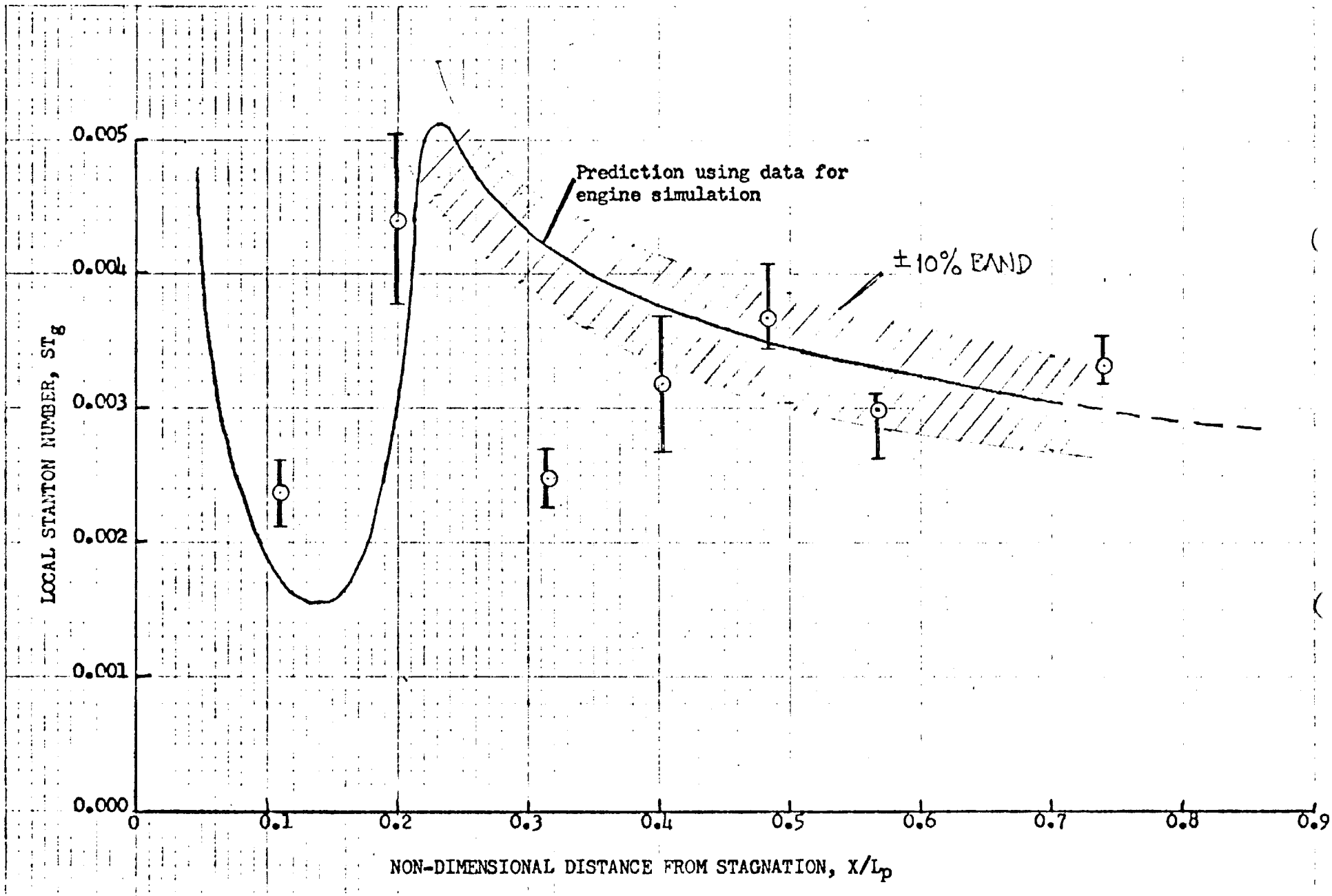
Prediction using data for engine simulation
±10% BAND
LOCAL STANTON NUMBER, ST_g
0.005
0.004
0.003
0.002
0.001
0.000
0
0.1
0.2
0.3
0.4
0.5
0.6
0.7
0.8
0.9
NON-DIMENSIONAL DISTANCE FROM STAGNATION, X/L_p

FIGURE 51.

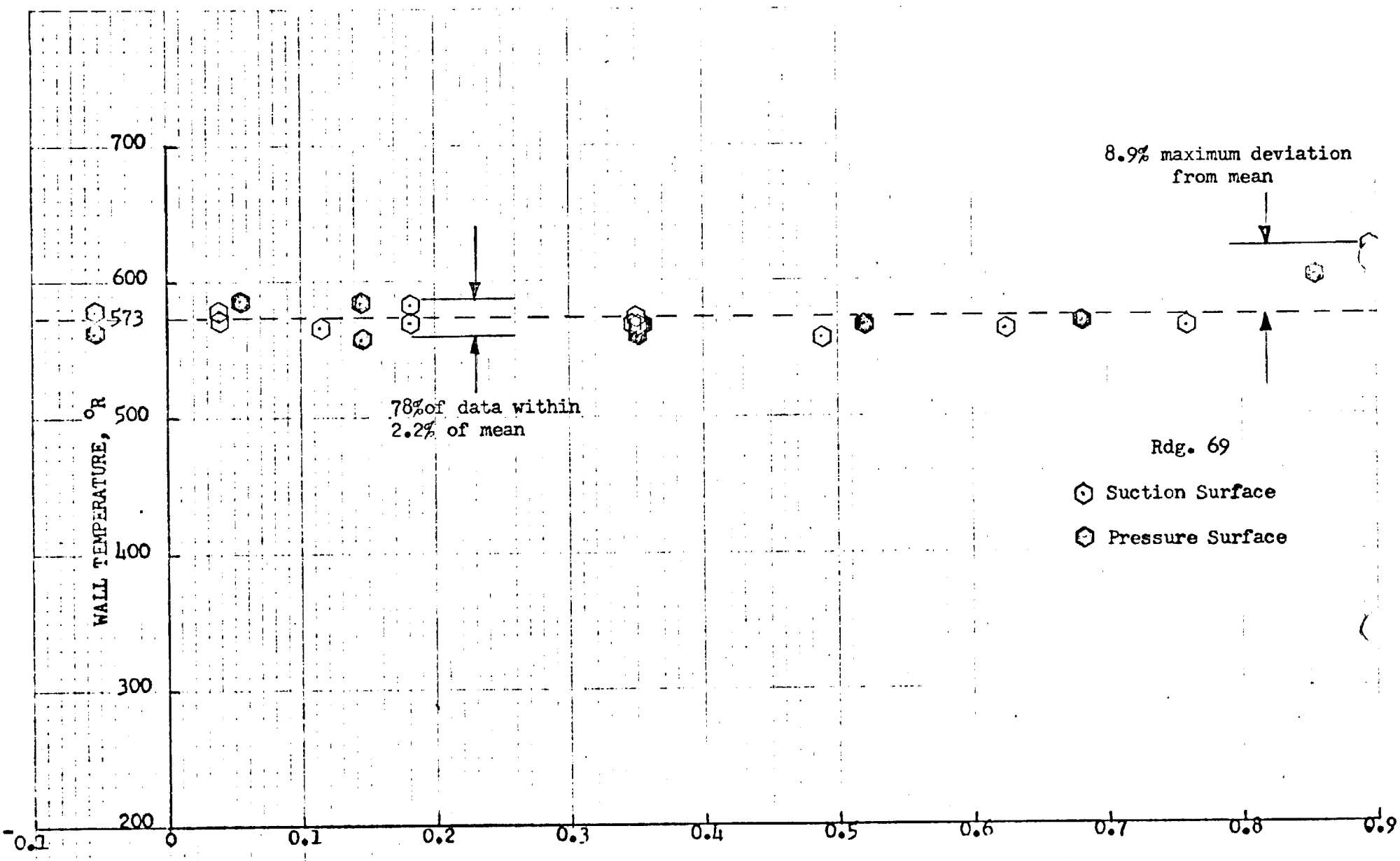
700
600
573
500
400
300
200
WALL TEMPERATURE, °R
-0.1
0
0.1
0.2
0.3
0.4
0.5
0.6
0.7
0.8
0.9
NON-DIMENSIONAL DISTANCE FROM STAGNATION, X/Ls,p
78% of data within 2.2% of mean
8.9% maximum deviation from mean
Rdg. 69
Suction Surface
Pressure Surface

FIGURE 52.

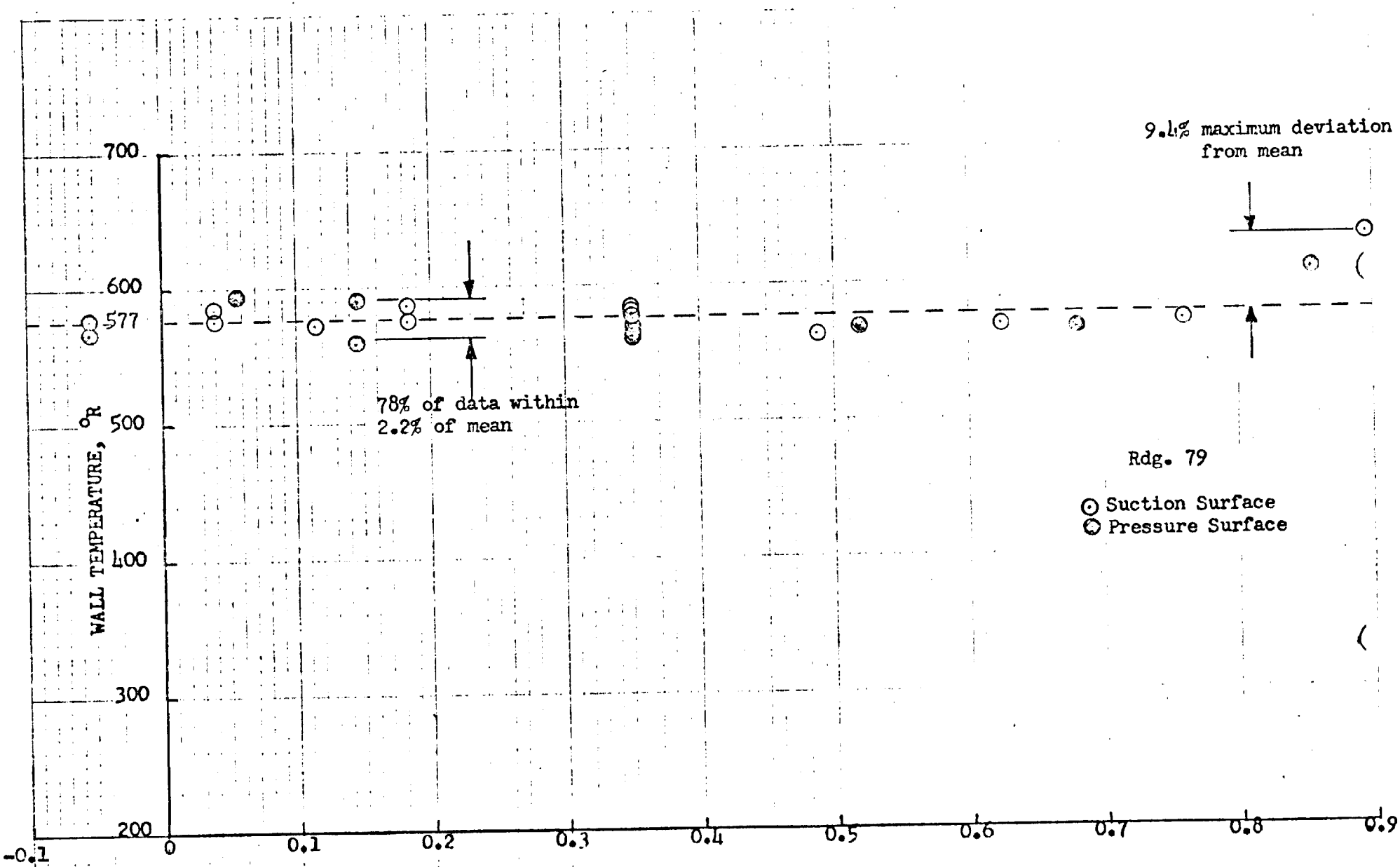
9.4% maximum deviation from mean
78% of data within 2.2% of mean
Rdg. 79
Suction Surface
Pressure Surface
WALL TEMPERATURE, °R
700
600
577
500
400
300
200
-0.1
0
0.1
0.2
0.3
0.4
0.5
0.6
0.7
0.8
0.9
NON-DIMENSIONAL DISTANCE FROM STAGNATION, X/Ls,p

FIGURE 53.

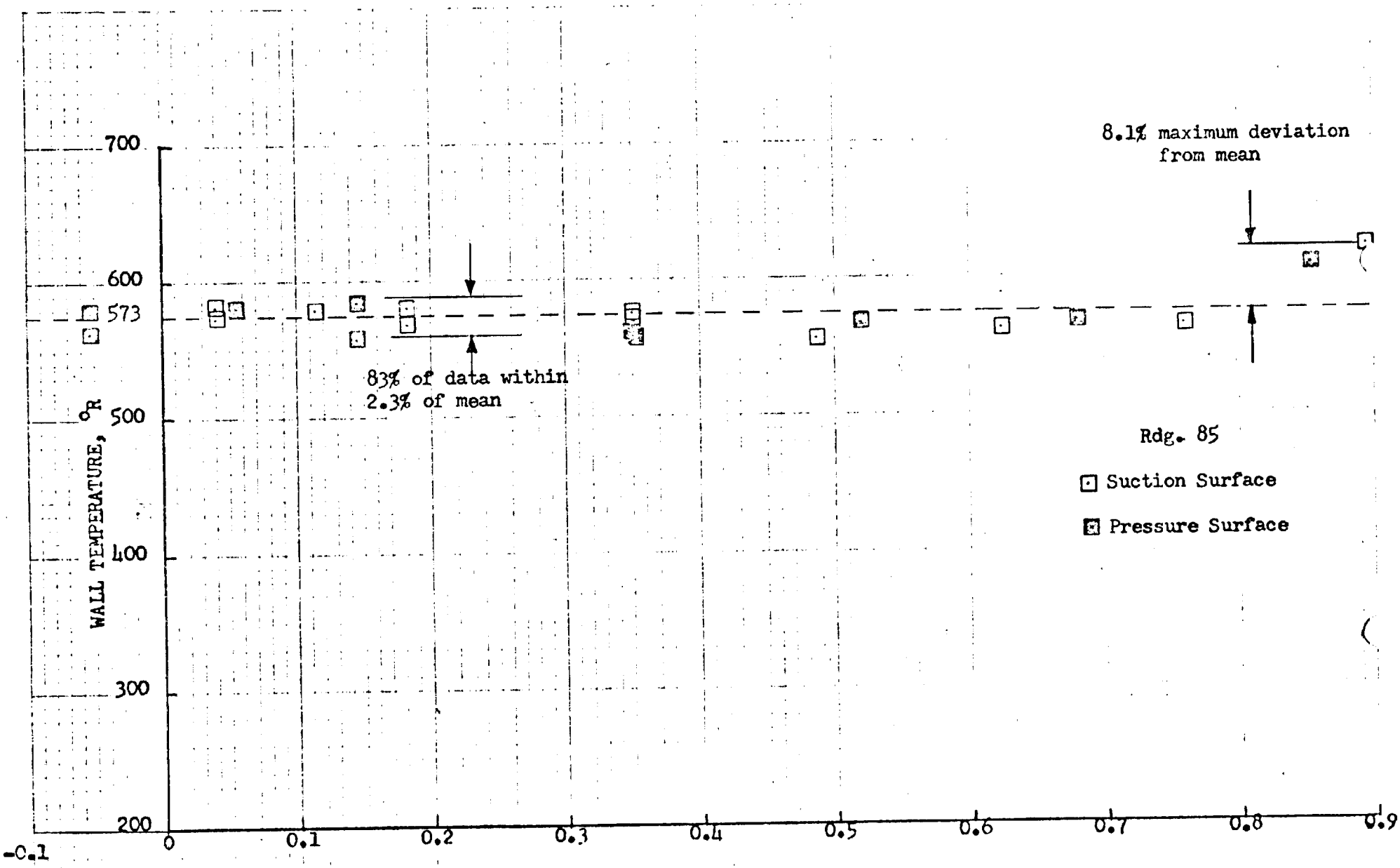
8.1% maximum deviation from mean
83% of data within 2.3% of mean
Rdg. 85
Suction Surface
Pressure Surface
WALL TEMPERATURE, °R
700
600
573
500
400
300
200
-0.1
0
0.1
0.2
0.3
0.4
0.5
0.6
0.7
0.8
0.9
NON-DIMENSIONAL DISTANCE FROM STAGNATION, X/Ls,p

FIGURE 54.

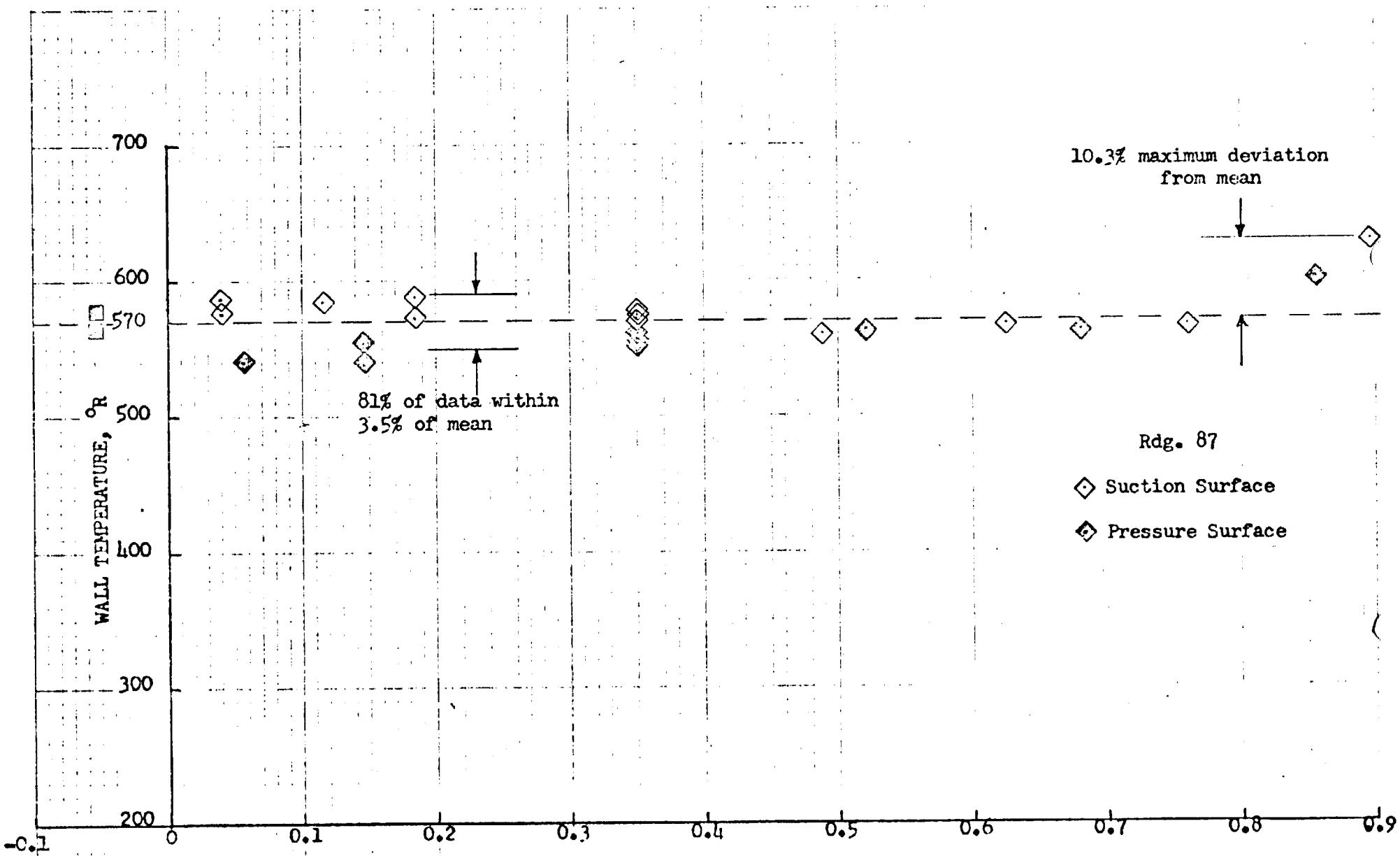
700
600
570
500
400
300
200
WALL TEMPERATURE, °R
-0.1
0
0.1
0.2
0.3
0.4
0.5
0.6
0.7
0.8
0.9
NON-DIMENSIONAL DISTANCE FROM STAGNATION, X/L_s,p
81% of data within 3.5% of mean
10.3% maximum deviation from mean
Rdg. 87
Suction Surface
Pressure Surface

FIGURE 55.

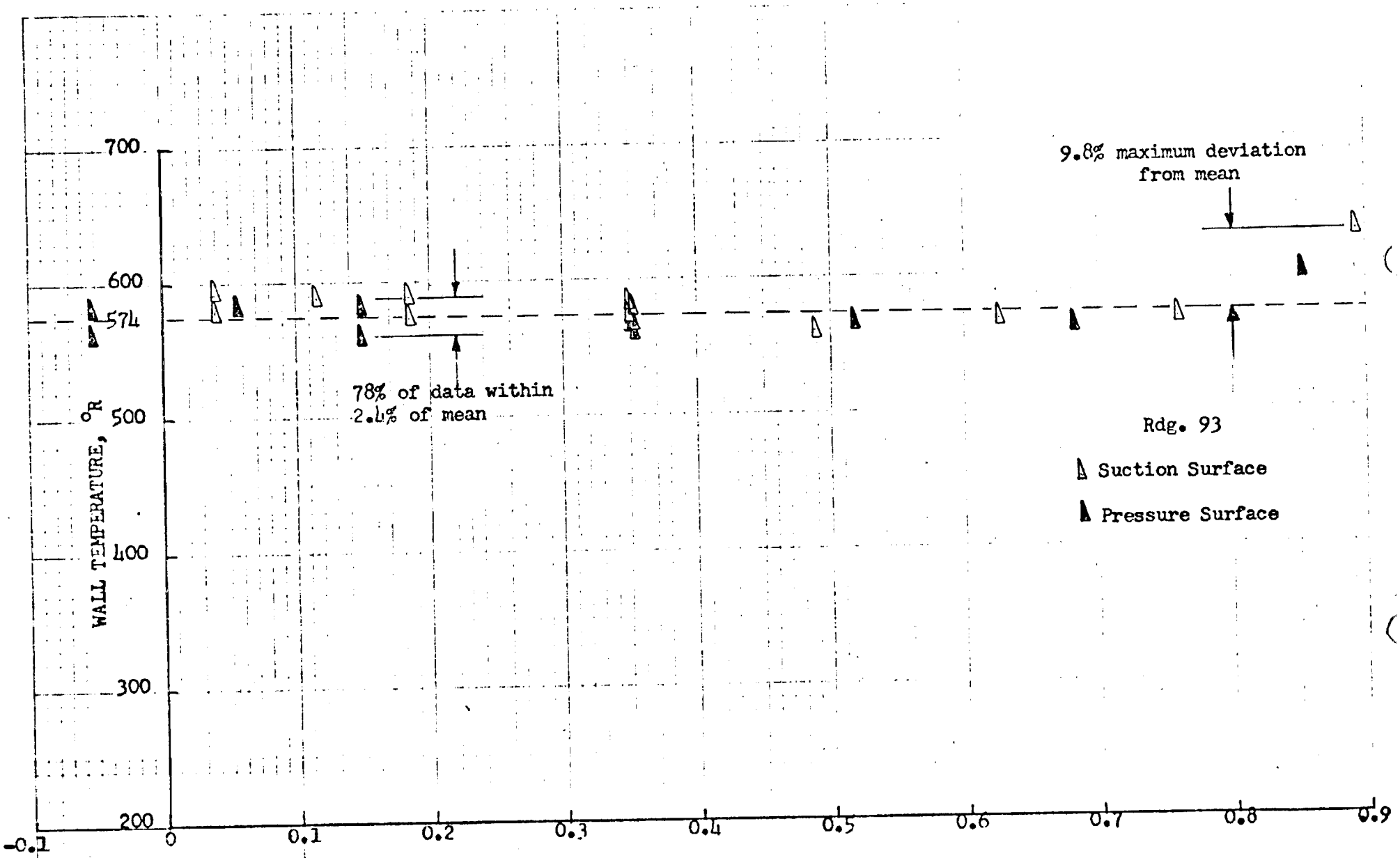
700
600
574
500
400
300
200
WALL TEMPERATURE, °R
-0.1
0
0.1
0.2
0.3
0.4
0.5
0.6
0.7
0.8
0.9
NON-DIMENSIONAL DISTANCE FROM STAGNATION, X/L_s,p
9.8% maximum deviation from mean
78% of data within 2.4% of mean
Rdg. 93
Suction Surface
Pressure Surface

FIGURE 56.

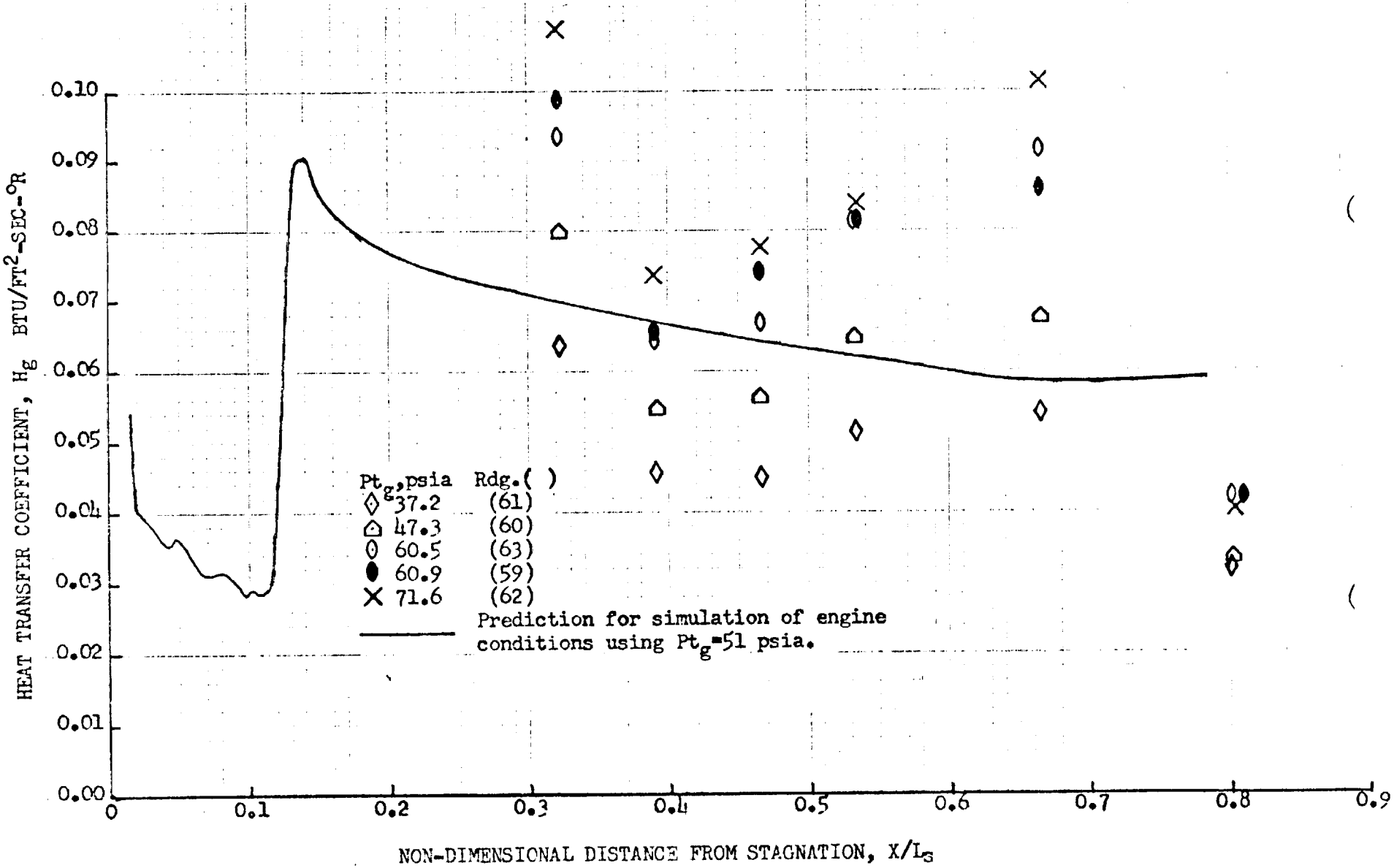
HEAT TRANSFER COEFFICIENT, H_g BTU/FT^2-SEC-^{o}R
0.10
0.09
0.08
0.07
0.06
0.05
0.04
0.03
0.02
0.01
0.00
0
0.1
0.2
0.3
0.4
0.5
0.6
0.7
0.8
0.9
NON-DIMENSIONAL DISTANCE FROM STAGNATION, X/L_s
Pt_g,psia Rdg.( )
37.2 (61)
47.3 (60)
60.5 (63)
60.9 (59)
71.6 (62)
Prediction for simulation of engine conditions using Pt_g=51 psia.

FIGURE 57

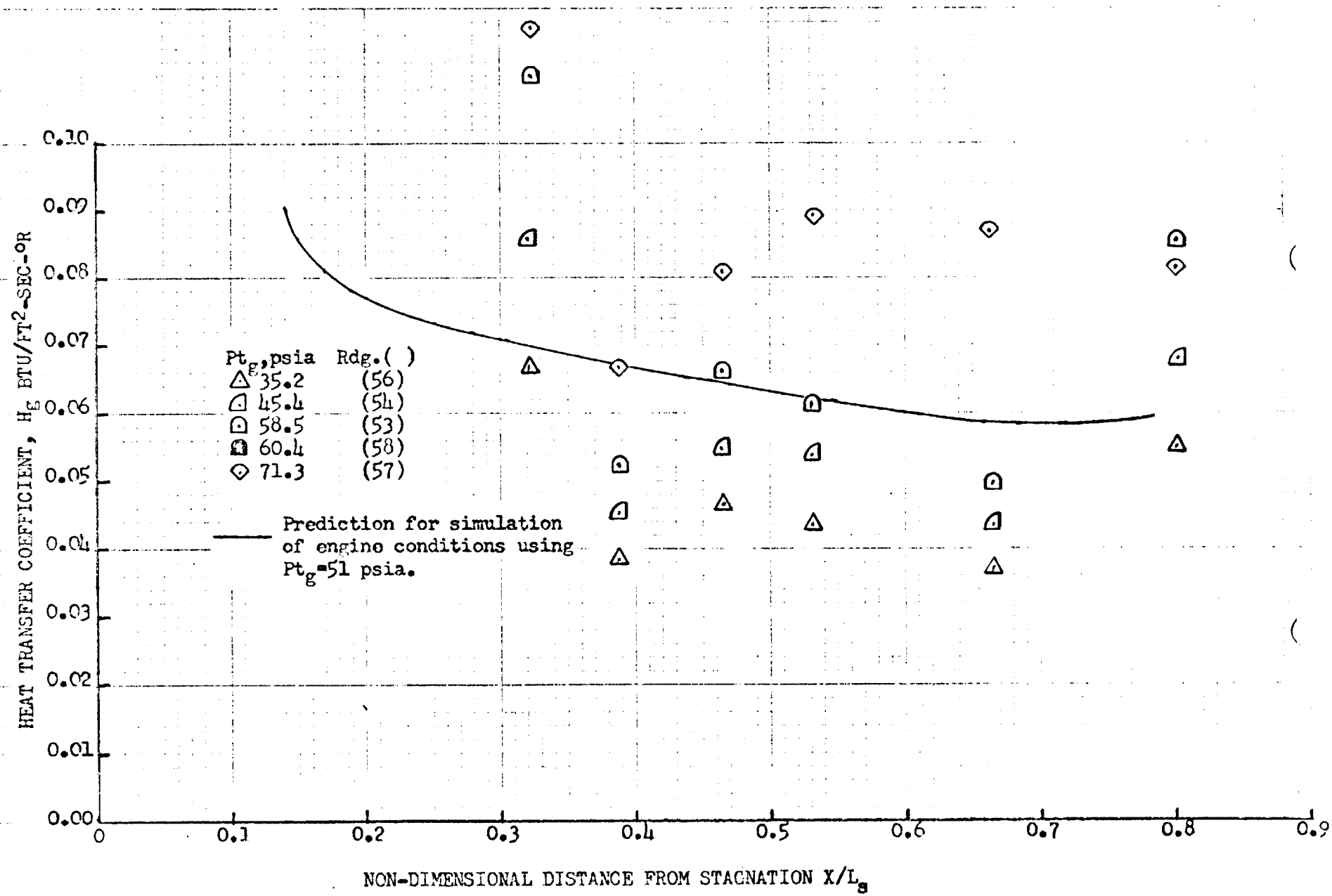
HEAT TRANSFER COEFFICIENT, H_g BTU/FT^2-SEC-°R
0.10
0.09
0.08
0.07
0.06
0.05
0.04
0.03
0.02
0.01
0.00
0
0.1
0.2
0.3
0.4
0.5
0.6
0.7
0.8
0.9
NON-DIMENSIONAL DISTANCE FROM STAGNATION X/L_s
Pt_g,psia Rdg.( )
35.2 (56)
45.4 (54)
58.5 (53)
60.4 (58)
71.3 (57)
Prediction for simulation of engine conditions using Pt_g=51 psia.

FIGURE 58.

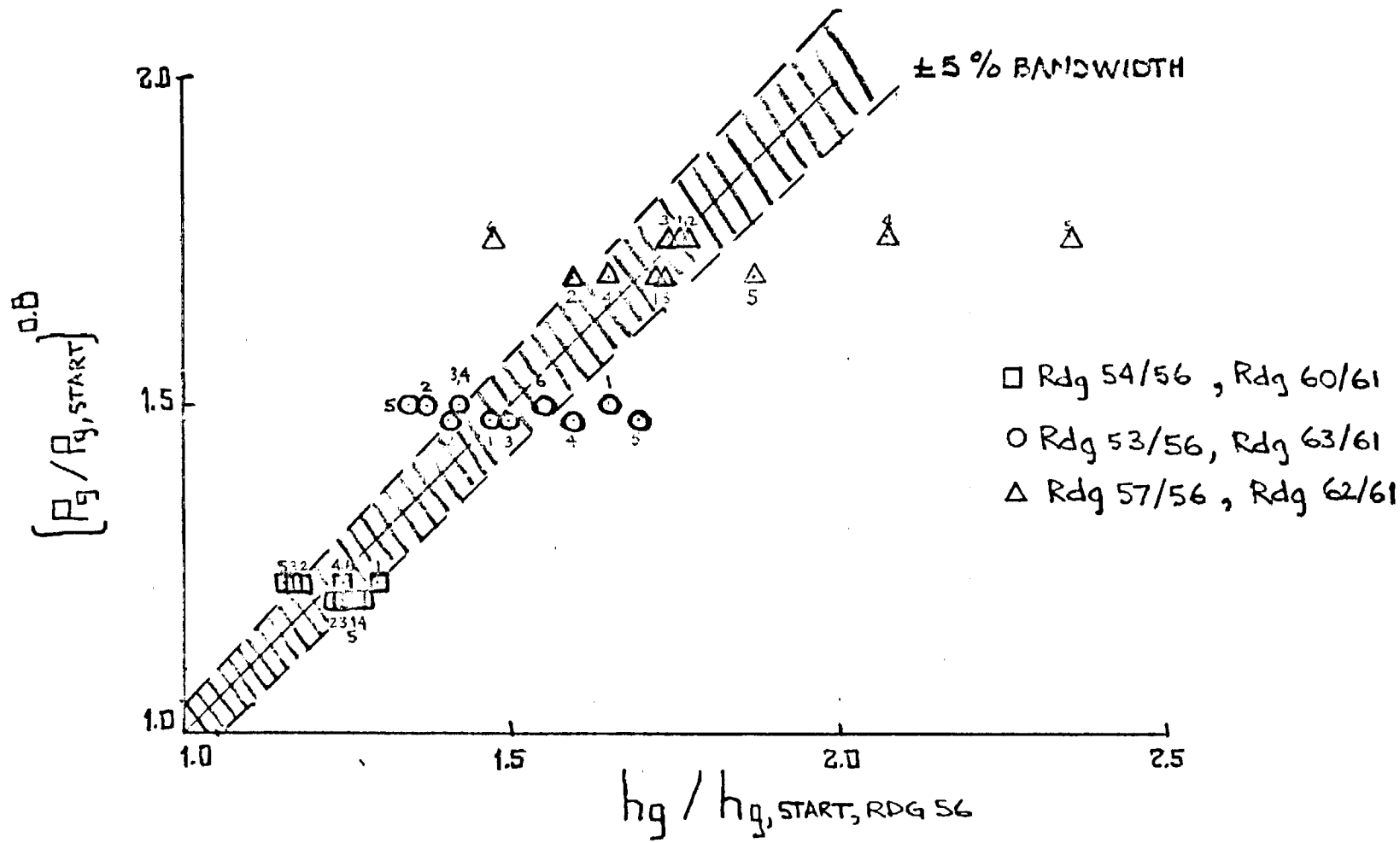

SUCTION SURFACE

FIGURE 59.

9/26/74 GJH

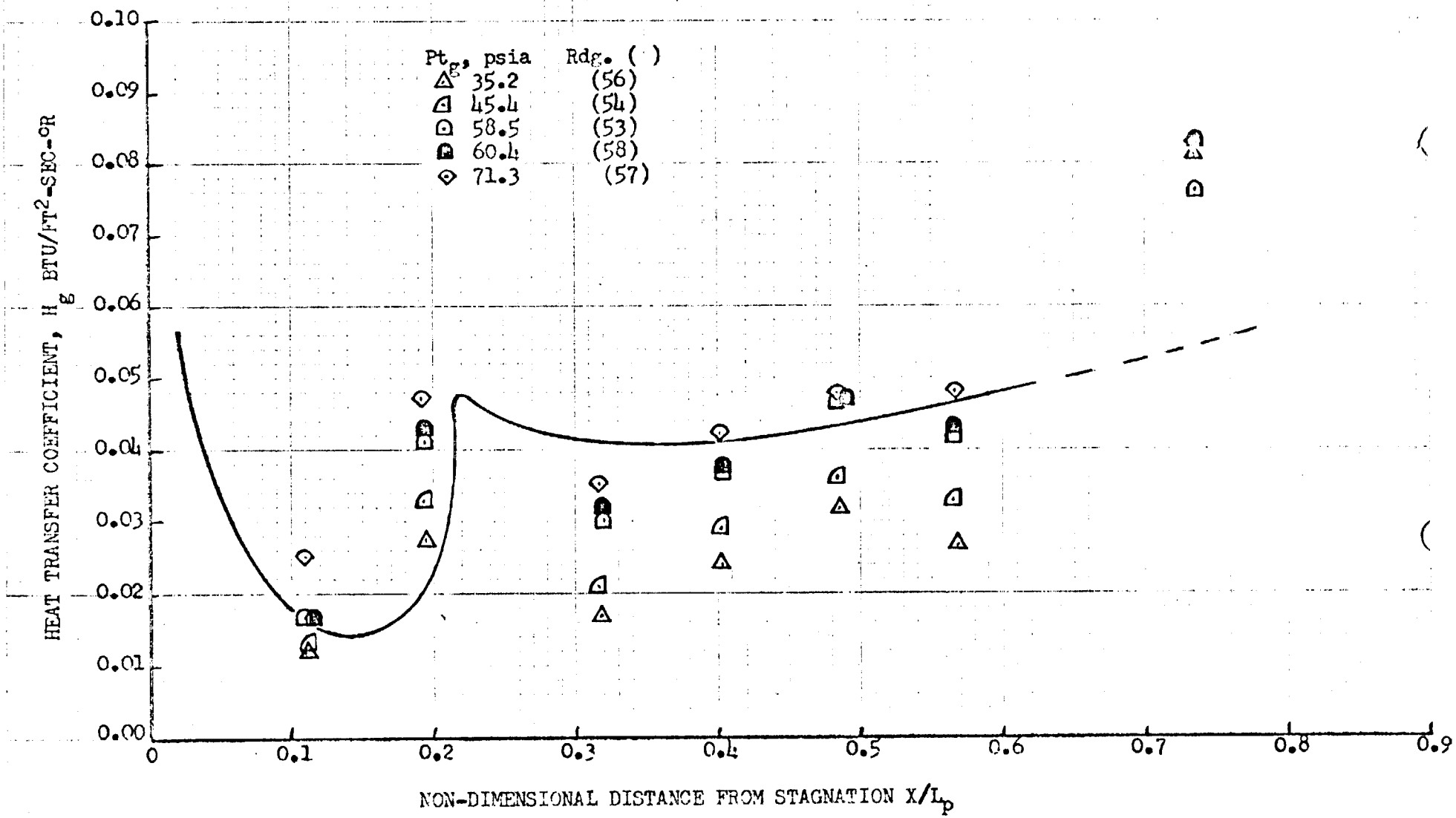
Pt$_g$, psia Rdg. ( )
35.2 (56)
45.4 (54)
58.5 (53)
60.4 (58)
71.3 (57)
HEAT TRANSFER COEFFICIENT, H_g BTU/FT^2-SEC-°R
0.10
0.09
0.08
0.07
0.06
0.05
0.04
0.03
0.02
0.01
0.00
0
0.1
0.2
0.3
0.4
0.5
0.6
0.7
0.8
0.9
NON-DIMENSIONAL DISTANCE FROM STAGNATION X/L$_p$

FIGURE 60.

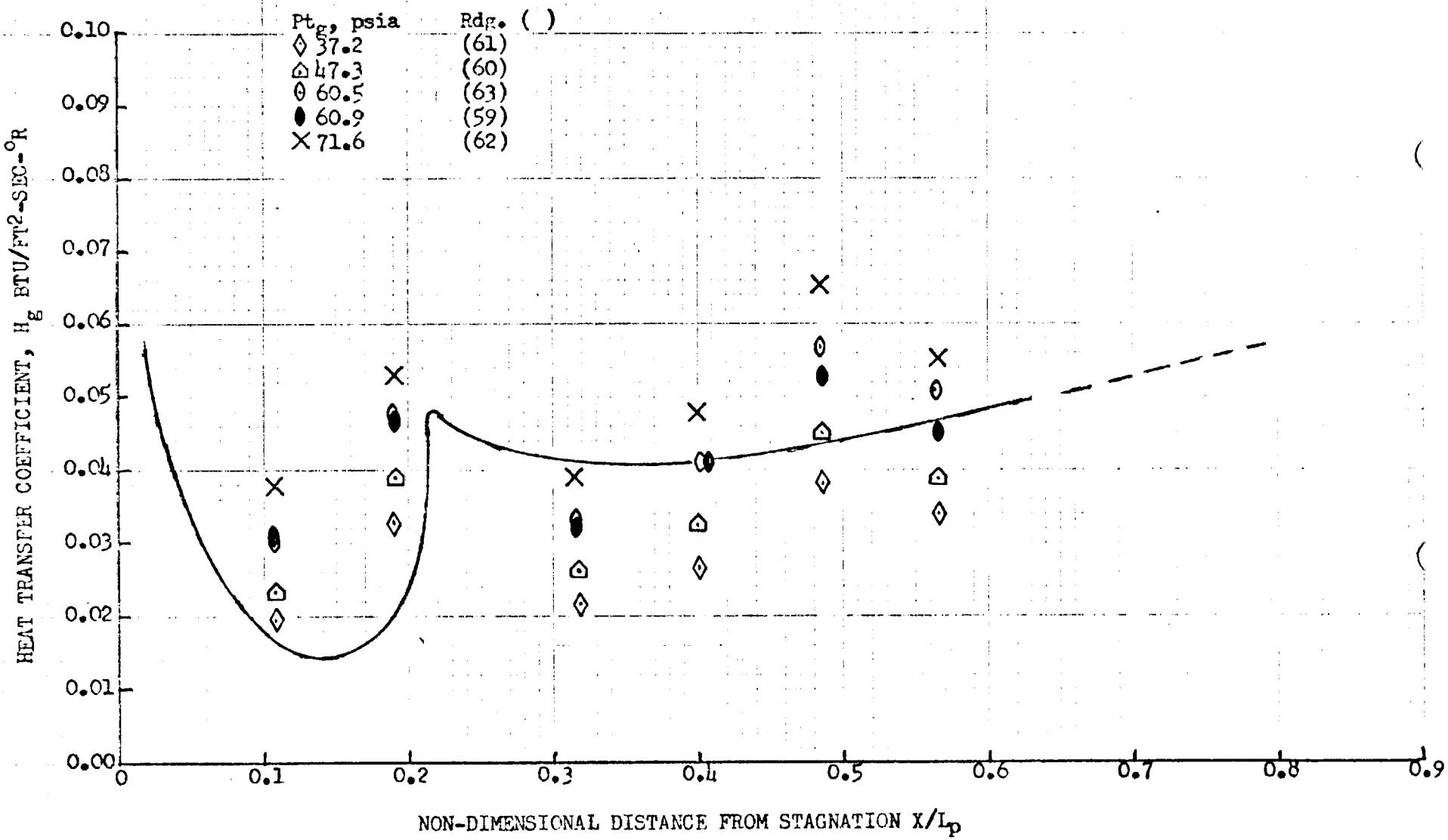
Ptg, psia
Rdg. ( )
37.2 (61)
47.3 (60)
60.5 (63)
60.9 (59)
71.6 (62)
HEAT TRANSFER COEFFICIENT, Hg BTU/FT2-SEC-°R
0.10
0.09
0.08
0.07
0.06
0.05
0.04
0.03
0.02
0.01
0.00
0
0.1
0.2
0.3
0.4
0.5
0.6
0.7
0.8
0.9
NON-DIMENSIONAL DISTANCE FROM STAGNATION X/Lp

FIGURE 61.

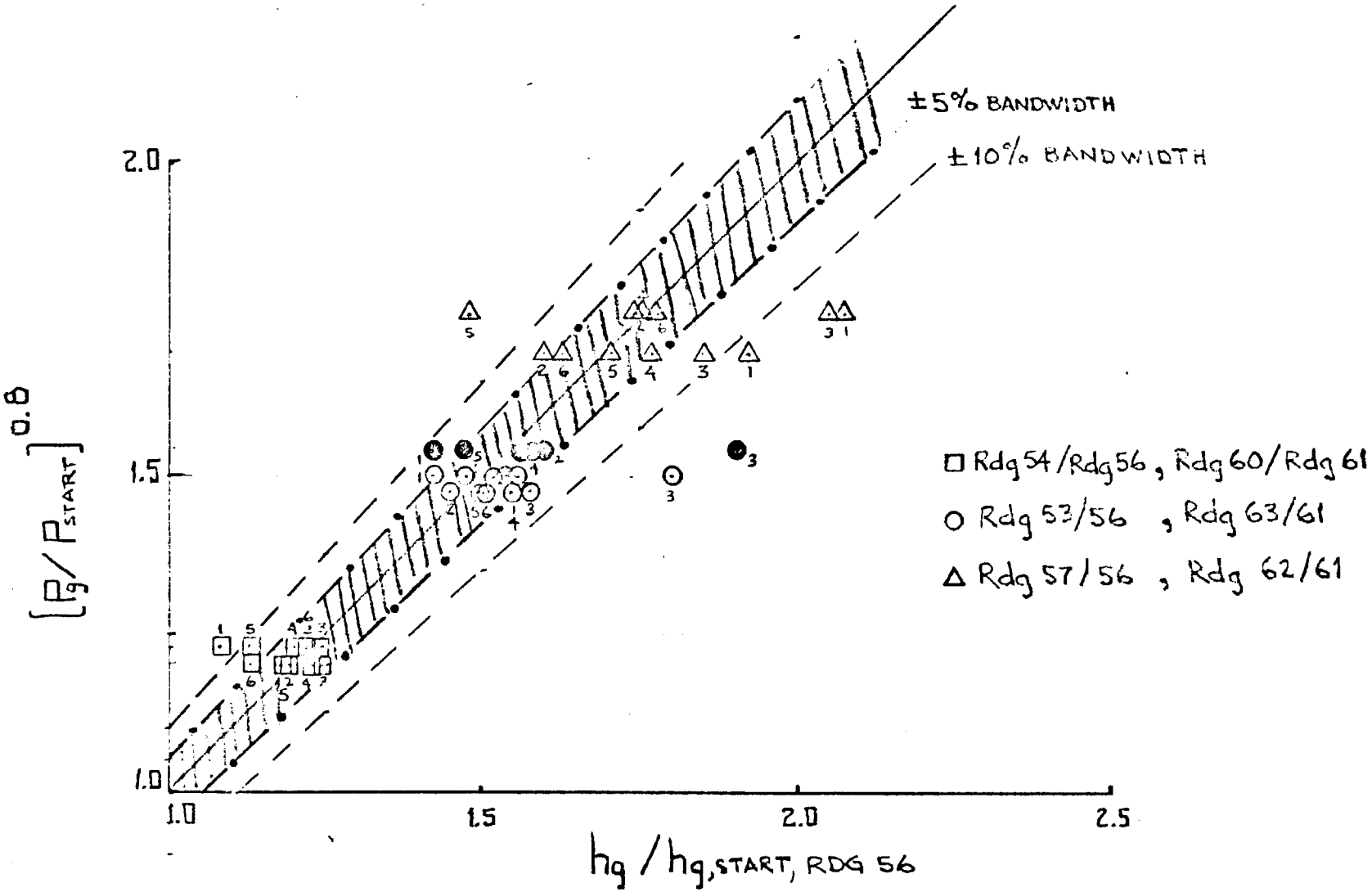

PRESSURE SURFACE

FIGURE 62

9/26/74 GJF

APPENDIX A.

... ANALYSIS ...

Local Mach number variation with pressure is

$$\frac{P_T}{P} = \left(1 + \frac{\gamma-1}{2} M^2\right)^{\gamma/\gamma-1} \qquad (1)$$

with assumption of negligible losses in total pressure (i.e. inviscid analysis" in 2-d channel) and small heat losses

$$\text{where } \frac{T_T}{T} = \left(1 + \frac{\gamma-1}{2} M^2\right) \qquad (2)$$

I. Check on P_T losses:

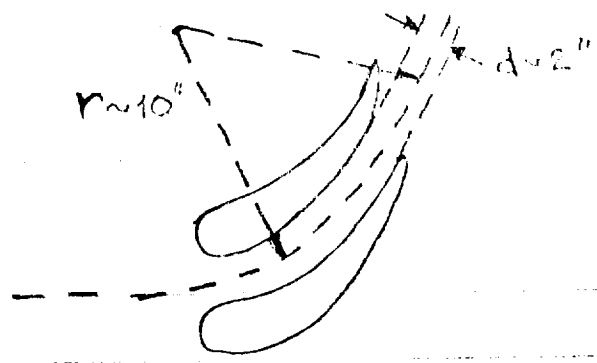

$$\frac{r}{d} = 5.0 \Rightarrow \left(\frac{L}{D}\right)_{bend} = 8.0 \qquad \left(\frac{L}{D}\right)_{friction} = \frac{8}{2} = 4.0$$

$$Re_{\substack{\text{LEADING EDGE}\\ \text{DIAMETER}}} \doteq 3\times10^5 \Rightarrow f = 0.015 = f_{turb}$$

$$\Delta P_{\substack{loss\\ bend}} = f\left(\frac{L}{D}\right)\left(\frac{\rho V^2}{2g_c}\right)$$

$$\Delta P_{\substack{loss\\ total}} = \Delta P_{loss,\,bend} + \Delta P_{loss,\,friction}$$

$$\Delta P_{loss\,total} = \left[f\left(\frac{L_b}{D}\right) + f_{turb}\left(\frac{L}{D}\right)_e\right]\frac{1}{2}\rho\frac{V^2}{g_c} \qquad (3)$$

$$\frac{\rho V^2}{2g_c} = \frac{P_{IN} M_{IN}^2 \gamma g R T_{IN}}{R T_{IN} 2 g_c} = \frac{P M^2 \gamma g}{2 g_c} = 1.64 \text{ psia}$$

$$\Delta P_{loss,\,total} = (1.64)\left[0.015(8+4)\right] \doteq 0.30 \text{ psia}$$

$$\therefore 1 - \left[\frac{P_{T\infty} - \Delta P_{loss}}{P_{T\infty}}\right] = 0.006 \quad \sim 0.6\% \text{ loss in } P_{T\infty}$$

II. Check on T_T change due to heat losses:

$$q''_{\text{removed, average over 8" of test surface}} \doteq 40 \text{ BTU/ft}^2\text{-sec}$$

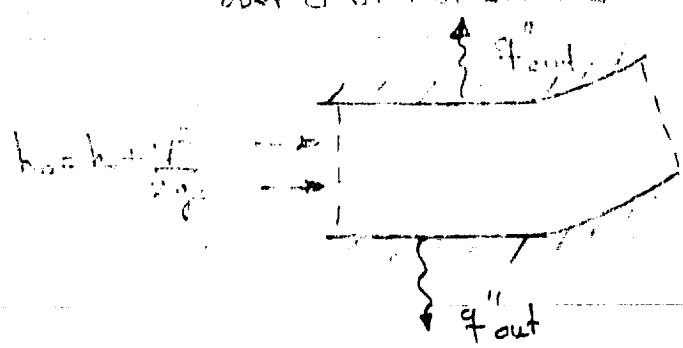

$$h_o = c_p T + \frac{V^2}{2 g_c J}$$

$$\text{or } T_o = T_T = T + \frac{V^2}{2 c_p g_c J}$$

T_T accounted for in Mach No. variation over surface.
but T_T also reduced due to heat losses.

$$c_p \dot{m} (\Delta T_T) = q''_{removed} A_{total}$$

$$A_{total} = 8.0'' \times 4.5'' \times 2 = 72 \text{ in}^2 \approx 0.5 \text{ ft}^2$$

$$\dot{m}_{design} \sim 4 \text{ lbm/sec}, \quad c_p = 0.264 \text{ BTU/lbm}^\circ\text{R}$$

$$\Delta T_T = \frac{q''_{w,avg} A_{total}}{c_{p\infty} \dot{m}}$$

$$\Delta T_T = \left(\frac{40\ Btu}{ft^2\text{-}sec}\right)\left(0.5\ ft^2\right)\left(\frac{Btu}{0.26\ lbm\ °R}\right)\left(\frac{sec}{4\ lbm}\right)$$

$$\Delta T_T = 15.9°$$

$$\frac{\Delta T}{T_{T_w}} = \frac{15.9°}{1248°R} = 1.5\%$$ change in total temperature due to heat losses

It will therefore be assumed that P_T and T_T remain essentially constant through test channel.

To simulate heat transfer phenomena at reduced conditions it is necessary that the Reynolds No. and Mach No. distribution over the test surface be matched for test and actual cases.

$$Re_{x_M} = Re_{x_E} \qquad M_{x_M} = M_{x_E}$$ where M = model, E = engine

The Mach number distribution can be simulated by proper geometric modeling and throttling capability of main flow channel in conjunction with by-pass ducts.

$$Re_x = \frac{\rho V x}{\mu} \qquad (4)$$

$$V = Ma = M(\gamma g R T)^{1/2} \qquad (5)$$

$$T = \frac{T_-}{\left(1 + \frac{\gamma - 1}{2} M^2\right)} \qquad (6)$$

$$\rho = \frac{p}{RT} = \frac{P\left(1+\gamma-\frac{1}{2}M^2\right)^{\gamma/\gamma-1}}{R\,T_T\left(1+\frac{\gamma-1}{2}M^2\right)} \qquad (7)$$

$$\therefore Re_x = \frac{M_x(\gamma g R)^{1/2}\,P_T\left(1-\gamma-\frac{1}{2}M_x^2\right)}{\left(1+\gamma-\frac{1}{2}M_x^2\right)^{1/2}\,R\,T_T\left(1-\gamma-\frac{1}{2}M_x^2\right)^{\gamma/\gamma-1}}$$

$$Re_x = \frac{M_x(\gamma g)^{1/2}\,P_T\left(1+\frac{\gamma-1}{2}M_x^2\right)^{-(\gamma+1)/2(\gamma-1)}}{(RT_T)^{1/2}}$$

$$\frac{Re_x^M}{Re_x^E} = \left(\frac{M_x^M}{M_x^E}\right)\left(\frac{\gamma^M g^M}{\gamma^E g^E}\right)^{1/2}\left(\frac{P_T^M}{P_T^E}\right)\left(\frac{R^E T_T^E}{R^M T_T^M}\right)^{1/2}\frac{\left[1+\frac{\gamma^E-1}{2}M_x^{E^2}\right]^{(\gamma^E+1)/2(\gamma^E-1)}}{\left[1+\frac{\gamma^M-1}{2}M_x^{M^2}\right]^{(\gamma^M+1)/2(\gamma^M-1)}}\left(\frac{X^M}{X^E}\right) \qquad (8)$$

if model is geometrically similar to engine component
$M^M = M^E$ at $X^M/L^M_{char} = X^E/L^E_{char}$

$$\therefore \frac{Re_x^M}{Re_x^E} = \underbrace{\left(\frac{M_{x_L}^M}{M_{x_L}^E}\right)}_{\approx 1.0}\left(\frac{\gamma^M}{\gamma^E}\right)^{1/2}\left(\frac{P_T^M}{P_T^E}\right)\left(\frac{R^E T_T^E}{R^M T_T^M}\right)^{1/2}\frac{\left[1+\frac{\gamma^E-1}{2}M_{x_L}^{E^2}\right]^{(\gamma^E+1)/2(\gamma^E-1)}}{\left[1+\frac{\gamma^M-1}{2}M_{x_L}^{M^2}\right]^{(\gamma^M+1)/2(\gamma^M-1)}}\underbrace{\left(\frac{X^M/L^M}{X^E/L^E}\right)}_{\approx 1.0}\frac{L^M}{L^E} \qquad (9)$$

at same relative position on surface

$$\frac{Re_x^M}{Re_x^E} = \left(\frac{P_T^M}{P_T^E}\sqrt{\frac{\gamma^M R^E T_T^E}{\gamma^E R^M T_T^M}}\right)\left(\frac{L^M}{L^E}\right) f\left(\gamma^E, \gamma^M, M_{x_L}^E, M_{x_L}^M\right)$$

if $M \ll 1$, $f(\gamma^E, \gamma^M, etc\ldots) = 1$

$$\left(\frac{Re_x^M}{Re_x^E}\right)_{\substack{\text{at same}\\ x/L}} = \left(\frac{P_T^M}{P_T^E}\right)\left(\frac{\gamma^M R^E T_T^E}{\gamma^E R^M T_T^M}\right)^{1/2}\left(\frac{L^M}{L^E}\right) = 1 \qquad (10)$$

where L^M, L^E are characteristic lengths

Knowing the conditions of the engine to be modeled (P_T^E, T_T^E, γ^E, R^E, L^E) choosing an operating temperature for the simulation dictates the proper total pressure necessary.

If the model is to perform as in actual conditions some normalized wall temperature must be similar between simulation and reality.

Using $\phi = \dfrac{T_{T\infty} - T_w}{T_{T\infty} - T_c}$ (11)

where T_c is fluid temperature cooling underside of wall exposed to $T_{T\infty}$

it is necessary that

$$\phi^E = \phi^M$$

$$\text{or } \frac{\phi^E}{\phi^M} = \frac{\left(T_{T\infty} - T_w / T_{T\infty} - T_c\right)^E}{\left(T_{T\infty} - T_w / T_{T\infty} - T_c\right)^M} = 1 \qquad (12)$$

$$\left(1 - T_w/T_{T\infty}\right)^E / \left(1 - T_c/T_{T\infty}\right)^E = \left(1 - T_w/T_{T\infty}\right)^M / \left(1 - T_c/T_{T\infty}\right)^M$$

$$\left(T_w/T_{T\infty}\right)^E \approx 0.50, \quad \left(T_c/T_{T\infty}\right)^E \approx 0.422$$

$$\therefore \left(1 - T_w/T_{T\infty}\right)^M / \left(1 - T_c/T_{T\infty}\right)^M = 0.865$$

Since it is necessary to use Water as the wall coolant

$T_c \approx 495°R$

$\therefore\ 0.365(1 - 495/T_{T\infty})^{M} = (1 - T_w/T_{T\infty})^{M}$ (13)

but since there is independent control of the water flow allowing wide variation in heat removal, choosing $T_{T\infty}$ in relation to the future use of ambient film cooling air would be more advantageous. Certain film cooling parameters that must be matched for engine and model require a definite relation between gas temperature and film coolant temperature. Such an analysis dictates $T_{T\infty}^{M} = 1240°R$ for available ambient film cooling air. for (13) to hold $T_w \approx 130°F$, which is no problem to achieve given the variable water flow rates available.

From a dimensional analysis of the governing equations it follows that the heat transfer is dependent on the following

$$St_x = St_x(x/L, Re_x, Pr, Gr_x, E)$$

where St_x = local Stanton No

Pr = Prandtl No

Gr_x = local Grashof No

E = Eckert No

Since forced convection >> natural convection for this problem $Gr_x \approx 0$

$$E^{E} = \frac{U_\infty^2}{g c_p \Delta T_{w-e}} = \frac{M_\infty^{E_2} \gamma^{E} R^{E} T_\infty^{E}}{\left(1 + \frac{\gamma - 1}{2} M_\infty^{E_2}\right) g c_p \Delta T_{w-e}^{E}}$$

$$\frac{E^E}{E^M} = \left(\frac{M^{2E}}{M^{2M}}\right)\left(\frac{\gamma^E}{\gamma^M}\right)\left(\frac{T_T^E}{T_T^M}\right)\left(\frac{C_p^M}{C_p^E}\right)\left(\frac{\Delta T^M}{\Delta T^E}\right)\frac{\left(1+\frac{\gamma^M-1}{2}M^{2M}\right)}{\left(1+\frac{\gamma^E-1}{2}M^{2E}\right)}$$

$\frac{M^{2E}}{M^{2M}} \to 1.0$, $\frac{\left(1+\frac{\gamma^M-1}{2}M^{2M}\right)}{\left(1+\frac{\gamma^E-1}{2}M^{2E}\right)} \sim 1.0$

$$\frac{\gamma^E}{\gamma^M} = 0.93 \qquad \frac{T_T^E}{T_T^M} = 2.79 \qquad \frac{C_p^M}{C_p^E} = 0.789$$

$$\frac{\Delta T^E}{\Delta T^M} = \frac{1740}{650} = 2.68$$

$$\frac{E^E}{E^M} \approx 0.764 \qquad \frac{Pr^E}{Pr^M} = \frac{0.697}{0.708} = 0.984$$

∴ Geometrical modeling yields x/L similar; selection of the proper gas temperature dictates the total pressure in the channel of proper Mach number distribution, yielding the proper mass flux to match the Reynolds No. distribution correctly. Such selection of conditions cannot match Pr properly nor the Eckert No., but come well within acceptable limits on the Pr and reasonable limits on the Eckert No.

Appendix B.
Axial Conduction Estimates

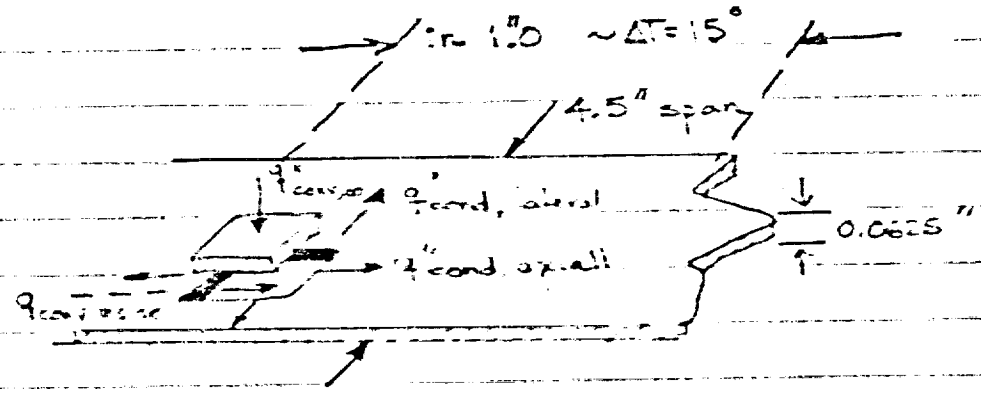

$$Q_{conv,\infty} = Q_{conv,inside} + Q_{cond,lateral} + Q_{cond,axial}$$

$$Q_{cond,lateral} \ll Q_{cond,axial}$$

$$q''_{cond,axial} = -k \frac{dT}{dx}$$

$$\left(\frac{dT}{dx}\right)_{max.\,measured} \doteq 15°/\text{in}$$

$$k_{copper} = 220 \text{ Btu/hr-ft-°F}$$

$$Q_{cond,axial} = (220)(15)\left(12 \frac{in}{ft}\right) A_{rea}$$

$$A_{rea,cond} = 4.5''(0.0625')(144)$$

$$Q_{cond,axial} \doteq 0.0215 \text{ Btu/sec}$$

$$q''_{conv,\infty,measured,mean} \doteq h_{rm} A_{conv} (\Delta T)$$

$$\doteq 0.03 \frac{Btu}{sec\,ft^2\,°R}(670°R)\left(\frac{4.5'' \times 1.0''}{144}\right)$$

$$= 0.623 \text{ Btu/sec}$$

$$\frac{Q_{cond,axial}}{Q_{conv,normal}} \approx \frac{0.0215}{.623} = 3.4\%$$